# Pump-probe Experiments with Ultrashort Mid-Infrared Light Pulses

Esperimenti di pump-probe con impulsi di luce ultracorti nel medio infrarosso

***Gabriele Berruto***

Advisor: DANIELE FAUSTI

Co-advisors: FULVIO PARMIGIANI and FRANCESCO RANDI

A thesis presented for the degree of
Master of Science in Physics


Department of Physics
University of Trieste
Italy
20 September 2014

# Contents

# Short abstract

We designed, built and characterized a setup for pump-probe spectroscopy with mid-infrared carrier-envelope phase-stable pump and ultrashort optical probe, and tested it on a $CuGeO_3$ sample.
The setup for the generation of mid-infrared light pulses is based on a pair of twin BBO-based optical parametric amplifiers pumped with photons at 1.5 eV and seeded by the same white-light continuum, generated in a YAG plate. The two so generated near-infrared signals are sent into a GaSe crystal, allowing for difference frequency generation in the mid-infrared range. Our setup produces carrier-envelope phase-stable laser pulses with energy per pulse at the µJ-level, in the tunable mid-infrared range 5-20 µm. A full amplitude and phase characterization of the mid-infrared electromagnetic field was done by means of electro-optic sampling measurements in a thin ZnTe crystal. Electro-optic sampling gave also the proof of short- and long-term carrier-envelope phase-stability.
In the last chapter, we present some preliminary results of pump-probe measurements on $CuGeO_3$, using the new pump-probe setup. We observed that the resonant excitation of a Cu-O vibrational mode around 13 µm gives a peculiar transient non-thermal polarization rotation of the near-infrared probe pulses.

# Some pics

T-ReX group - kHz (or THz, or NLO, or UCMµJLDFG) lab

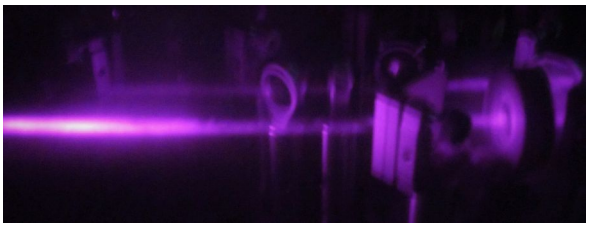

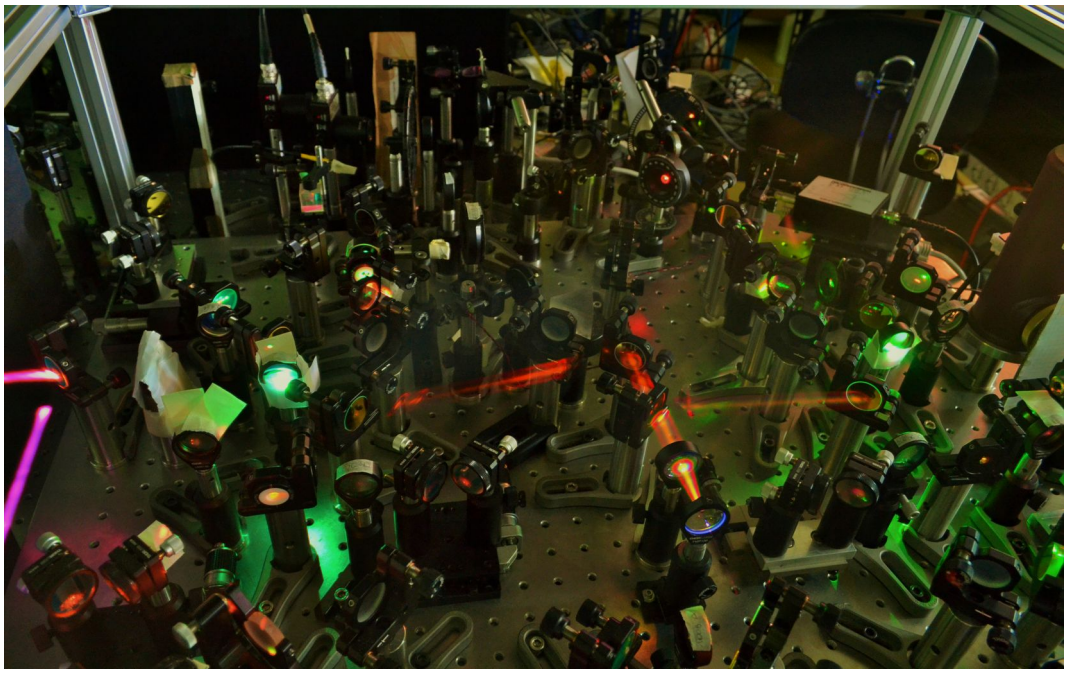

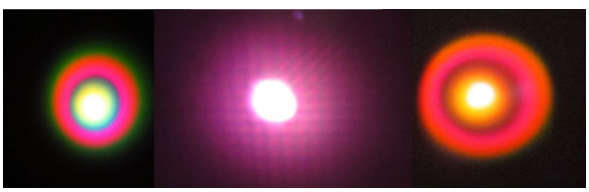

# Riassunto — Invito alla lettura

Questa tesi presentata per la discussione finale del Corso di Laurea Magistrale Interateneo in Fisica, presso il Dipartimento di Fisica dell'Università degli Studi di Trieste, è frutto del lavoro svolto presso i Laboratori T-ReX di Basovizza, nelle strutture di Elettra Sincrotrone Trieste S.C.p.A., e si colloca nell'ambito disciplinare delle spettroscopie, ottica e fisica della materia condensata.
La tesi ha come argomento cardine esperimenti di *pump-probe* con impulsi ultracorti di luce laser nel medio infrarosso. Nei primi capitoli, a seguito di un'introduzione al mondo dell'ottica non lineare, tratteremo la progettazione, costruzione e caratterizzazione del setup per la generazione di impulsi laser nel medio infrarosso. Sarà poi presentata e discussa la completa caratterizzazione del campo elettromagnetico nel medio infrarosso, e, nel finale, presenteremo i risultati preliminari di esperimenti di *pump-probe* su germanato di rame.

Interpreto questo breve riassunto in lingua italiana più come un semplice invito alla lettura che come una stringata sinossi tecnica, che può essere trovata nello Short abstract, oltre che nel corpo della tesi.

La natura tecnica degli *esperimenti di pump-probe* (si veda la figura 1) è la seguente. Il campione, ad esempio un cristallo, è portato fuori dall'equilibrio grazie all'interazione con un intenso impulso di luce molto corto (decine o centinaia di femtosecondi), che chiamiamo *pump*, e va in un nuovo stato metastabile.
A seguito della fotoeccitazione il campione si troverà in una condizione di non equilibrio, la cui natura può essere termica o non-termica. Un secondo impulso, il *probe*, incide quindi sul campione, andando a carpire informazioni su questo nuovo stato del materiale. I casi nei quali lo stato fuori equilibrio è di tipo termico sono i più facili da interpretare: il campo elettrico del *pump*, all'ordine zero, rilascerà semplice-

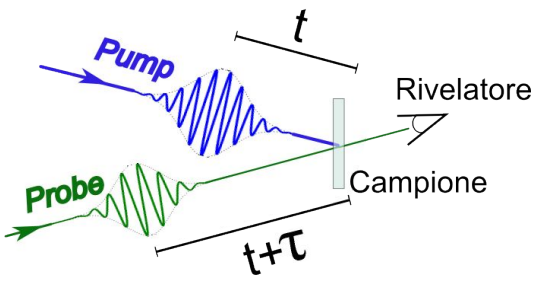


Figure 1: Schema concettuale di un esperimento di *pump-probe*. $\tau$, il ritardo temporale tra i due impulsi, è variabile.

mente una certa quantità di energia al campione, che incorrerà in un processo di riscaldamento. Lo stato metastabile (termico o non-termico) rilasserà in un tempo finito verso lo stato di equilibrio di partenza, seguendo una sua propria dinamica. Lo studio di questa dinamica viene effettuato tramite l'interazione del campione con un secondo impulso di luce (come detto, il *probe*), che arriva sul campione ad un tempo successivo rispetto al *pump* (è ritardato di un tempo $\tau$, vedi figura 1). Il *probe* è un impulso poco intenso, perché deve solo sondare lo stato del materiale, che è stato perturbato dal *pump*. Modificando il ritardo tra i due impulsi e misurando la riflettività o la trasmittività del campione agli impulsi di *probe*, si può seguire la dinamica di rilassamento del materiale che si sta studiando, e da questa svelare e comprendere quali sono le interazioni caratteristiche dei gradi di libertà del materiale.
Gli studi dei materiali fuori equilibrio non servono tanto a comprendere il loro comportamento nella fase transiente in sé, ma hanno di solito l'obiettivo di aumentare la comprensione dei meccanismi microscopici che determinano le proprietà dei materiali all'equilibrio. Infatti, un po' naïvamente, fuori dall'equilibrio si possono studiare separatamente le interazioni tra i vari gradi di libertà del sistema, mentre all'equilibrio essi competono simultaneamente, e, inevitabilmente, si sovrappongono.

Con questo lavoro, noi vogliamo aprire la strada ad una spettroscopia *pump-probe* nuova, che si basi sull'eccitazione dei gradi di libertà a bassa energia del sistema nel range spettrale del medio infrarosso, cioè alle energie tipiche dei processi microscopici che danno luogo alla termodinamica, come le oscillazioni dei reticoli cristallini. L'obiettivo è quindi quello di poter compiere degli studi di non-equilibrio basati sulla fotoeccitazione coerente con impulsi ultracorti e con basse energie dei fotoni, che possono eccitare selettivamente alcuni gradi di libertà interni del materiale.

A tale scopo, abbiamo progettato e costruito un setup ottico basato sulla disposizione "a cascata" di varie tecniche di ottica non lineare, in modo da ottenere impulsi finali nel medio infrarosso, con lunghezza d'onda tra 5 e 20 micrometri, partendo da impulsi con lunghezza d'onda di 800 nanometri. Campi elettrici molto intensi possono infatti indurre una polarizzazione nei cristalli che non scali linearmente con il campo elettrico applicato, e che —a sua volta— agisce come termine sorgente per la generazione di fotoni a nuove frequenze, come studiato dall'*ottica non lineare*.

La peculiarità dello schema adottato (si vedano le figure 2.8 e 3.4) risiede nel fatto che gli impulsi così prodotti siano stabili nella fase tra il campo elettrico e l'inviluppo dell'impulso, aspetto generalmente non verificato per impulsi generati nei comuni oscillatori laser. Questo è stato possibile costruendo due amplificatori ottici parametrici, simmetrici, e "inseminati" dagli stessi impulsi di luce bianca. L'amplificazione ottica parametrica è un processo non lineare del secondo ordine (di interazione a tre onde), nel quale fotoni ad una frequenza vengono convertiti —grazie all'interazione con un mezzo non lineare e non centrosimmetrico– in coppie di fotoni a frequenze più basse, conservando energia e momento. Gli impulsi generati dai due amplificatori ottici parametrici sono nel vicino infrarosso. Con un processo di generazione della loro frequenza differenza, si ottengono infine impulsi di luce coerente nel medio infrarosso.
Gli impulsi così creati hanno una lunghezza d'onda regolabile nell'intervallo di interesse, ed energie superiori al microjoule per impulso.

Grazie ad un interferometro di Michelson, costruito per questo lavoro, si è potuto studiare il contenuto spettrale degli impulsi, che sono stati utilizzati poi per fare campionamento elettro-ottico su un campione sottile di tellururo di zinco (si veda ad esempio la misura in figura 2). Una misura di campionamento elettro-ottico è una spettroscopia nel dominio dei tempi, essenzialmente un esperimento di *pump-probe* dove si misura la rotazione di polarizzazione del *probe* indotta dalla presenza del campo elettrico di *pump* nel cristallo, e dà accesso direttamente al campo dell'impulso di *pump*, che quindi viene caratterizzato completamente, in ampiezza e fase.

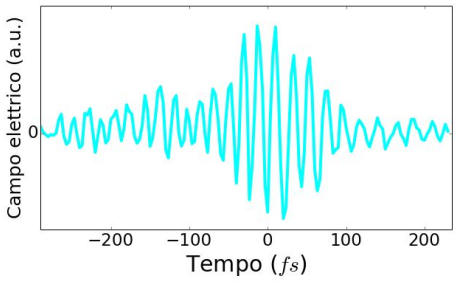


Figure 2: Esempio di campo elettrico degli impulsi nel medio infrarosso, così come misurato dal campionamento elettro-ottico.

Per effettuare questi esperimenti è fondamentale, come mostrato in figura 3, che l'inviluppo dell'impulso di *probe* sia più corto del periodo di oscillazione del campo elettrico di *pump*. Abbiamo quindi usato un *probe* ultracorto, con durata temporale di circa 15 femtosecondi, generato grazie all'allargamento spettrale in una fibra cava riempita di argon.

È stata quindi verificata la stabilità di fase degli impulsi prodotti, su tempi superiori a quelli tipici degli esperimenti di *pump-probe*, cioè si è verificata la possibilità di effettuare esperimenti di *pump-probe* che consentano di essere sensibili alla fase del campo elettrico che eccita il materiale, e quindi di vedere la risposta del campione direttamente al *campo elettrico*, non solo alla quantità di energia rilasciata (l'*inviluppo* dell'impulso), come avviene abitualmente.

Il setup di *pump* nel medio infrarosso e *probe* ottico è stato utilizzato per compiere delle misure preliminari su un campione sottile di germanato di rame, con l'obiettivo di eccitare coerentemente in maniera risonante un modo vibrazionale rame-ossigeno

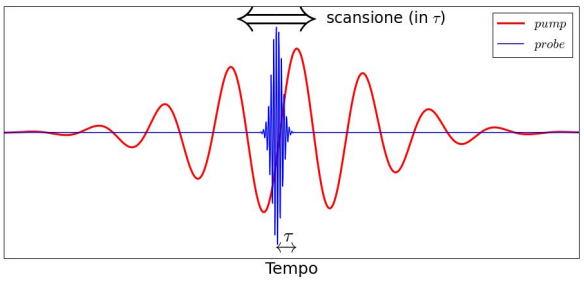


Figure 3: *Pump* in rosso, *probe* ultracorto in blu. La differenza tra i loro centri dell'inviluppo è il ritardo temporale $\tau$, e la misura di campionamento elettro-ottico avviene misurando la variazione di polarizzazione del *probe* al variare di $\tau$.

a lunghezza d'onda di circa 13 micrometri. Non si è osservata alcuna oscillazione coerente nella risposta (misurata dal *probe* a 800 nm) del germanato di rame, ma si è misurato un cambiamento qualitativamente significativo della rotazione della polarizzazione del probe quando si fotoeccita il campione alla lunghezza d'onda del modo vibrazionale.

Per concludere, in questo lavoro si è costruito un nuovo setup ottico e se ne è verificato il funzionamento. Siamo riusciti a generare in maniera controllata impulsi di luce laser nel medio infarosso, ne abbiamo verificata la stabilità in fase ed è stato inoltre possibile caratterizzare completamente questi impulsi infarossi tramite misure di campionamento elettro-ottico. Infine, da esperimenti preliminari su germanato di rame, abbiamo mostrato un effetto dell'eccitazione di un modo vibrazionale rame-ossigeno.

# Introduction

This thesis I present for the M.Sc. degree in Physics (curriculum in Condensed Matter Physics) at the University "Università degli Studi di Trieste" is the result of the work carried out at the T-ReX Laboratories in Basovizza, thanks to the collaboration between Università degli Studi di Trieste and Elettra-Sincrotrone Trieste S.C.p.A.
Throughout this thesis, we will deal with optics and time-resolved spectroscopies on materials. In particular I will discuss a new setup we built at T-ReX Laboratories, which opens the door to time-resolved spectroscopy of out-of-equilibrium materials brought out-of-equilibrium by ultrashort *mid-infrared* light pulses.

The experimental technique we used is the "pump and probe spectroscopy", which indeed is an out-of-equilibrium time-resolved spectroscopy technique. We will refer to it simply as *pump-probe*. The rationale of pump-probe experiments (exemplified in Fig. 4) is the following. The sample is kicked out of equilibrium by an ultrashort light pulse (called pump) and brought into a transient new thermal or sometimes non-thermal state. Such transient state is measured by means of a second light pulse (probe) impinging on the sample at a later time. The measure in real time of the relaxation dynamics through the reflectivity or transmittivity of the probe pulse is used to unveil the characteristic interaction determining the physical properties of the studied material.
The aim of my thesis was to build and characterize a setup allowing for non-equilibrium studies based on photoexcitation with ultrashort light pulses in the mid-infrared range. These mid-infrared pulses can be used to investigate materials at low energy scales via a selective excitation of some degrees of freedom, for example vibrational modes. The energy scales involved are those of thermodynamics, a typical incoherent phenomenon, which here could be studied coherently.

In this thesis work we designed and built an optical setup based on a cascade of non-

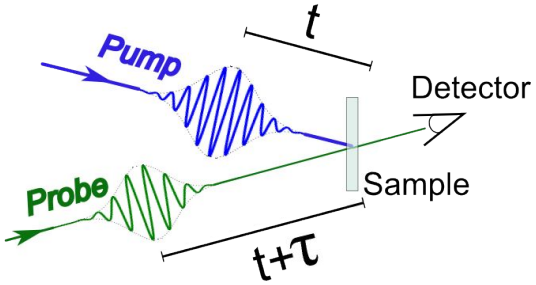


Figure 4: Conceptual scheme of a pump-probe experiment.

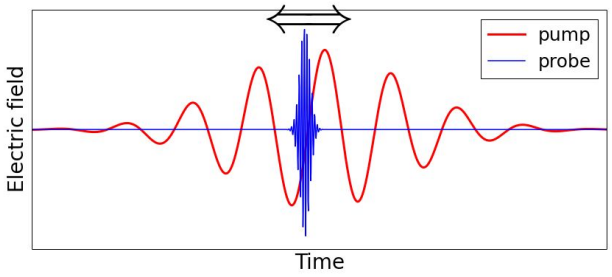


Figure 5: Pump in red, ultrashort probe in blue. The temporal difference between their envelope maxima is the delay time $\tau$, and an electro-optic sampling is performed measuring the change in the probe polarization after the sample, as a function of the delay time $\tau$. The electric field of the pump is mapped in the polarization rotation of the probe through a change in the birefringence of the crystal hosting the electro-optic sampling process.

linear optics techniques to generate mid-infrared ($\lambda$ = 5-20 µm) laser pulses, starting from a pulsed laser beam with central wavelength 800 nm and repetition rate 1 kHz. High intensity laser fields can induce a nonlinear polarization in crystals, i.e. a polarization which contains nonlinear terms in the electric field. The nonlinear polarization in turn acts as a source term, and gives rise to fields at new wavelengths, as studied by nonlinear optics.
Our scheme is designed in order to have mid-infrared light showing pulse-to-pulse stability in the phase between the oscillating electric field and the pulse envelope (Carrier-Envelope Phase, CEP). We built two symmetric Optical Parametric Amplifiers (OPAs) seeded by the same white-light continuum, generated in a YAG crystal. Each OPA has two stages, the first being non-collinear, and the second collinear, both using BBO crystals as nonlinear media. Our OPAs are tunable in the near-infrared range, and their efficiency exceeds 25%. The two signals produced in the OPAs partecipate to a photon downconversion process (Difference Frequency Generation, DFG) in a GaSe crystal. The tunable mid-infrared pulses, reaching energies of a few µJ per pulse, have been revealed by a MCT infrared detector and spectrally characterized in a Michelson interferometer built for this thesis.

I demonstrate that the mid-infrared pulses produced with the optical scheme described are carrier-envelope phase-stable. In order to measure the phase of the pumping electric field, the envelope of the probe should be significantly shorter than the period of the oscillating electric field. For this reason we use as probe ultrashort pulses (with a temporal width of approximately 15 fs) at $\lambda$ = 800 nm, which undergo spectral broadening in a hollow fiber filled by Argon and are subsequently temporally compressed in a set of chirped mirrors.

Electro-optic sampling (see Fig. 5 for a conceptual representation) in a thin sample of ZnTe allows us to have a full phase and amplitude characterization of the electromagnetic field produced by DFG and to verify its CEP-stability over a period of time of hours. Moreover, the electro-optic sampling measurements (Fig. 6) allow us to analyze the mid-infrared pulses both in time and energy domains, and give a complete information about the temporal structure of the pulse.
Furthermore, using the setup developed, we performed benchmark experiments for the new pump and probe technique on test GaAs and $CuGeO_3$ samples. In this dis-

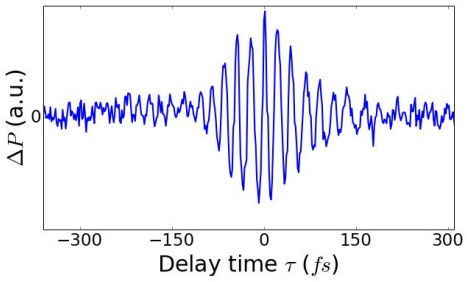


Figure 6: Polarization rotation, proportional —in an electro-optic sampling measurement— to the electric field of the pump.

sertation I will present only the preliminary results on $CuGeO_3$, and, in that case, we observed for the first time that the resonant excitation of a Cu-O vibrational mode (pump pulses around 13 µm wavelength) gives a peculiar nonthermal polarization rotation of near-infrared pulses.

The thesis is organized as follows. Chapter 1 is an introduction to concepts and techniques of nonlinear optics; Chapter 2 a brief review about the carrier-envelope phase problem and about the methods used to reach a carrier-envelope phase stability. In Chapter 3, I will describe in detail the setup built for this thesis and in Chapter 4 I will show the characterization of the mid-infrared fields generated in our setup. Finally, in Chapter 5, some preliminary results on $CuGeO_3$ are presented, and a qualitative interpretation of data is proposed.

# Chapter 1

# Nonlinear Optics

The majority of optical phenomena can be described within the *linear* approximation. It is called "linear" because the polarization effects in a medium scale linearly with the strenght of the electric field. This approximation holds as long as the strength of the external field is small with respect to the internal (atomic) field. If it is not the case, a plethora of new effects becomes accessible. The advent of the laser (1960) enabled the possibilty of producing monochromatic radiation with electric fields strong enough to observe and use nonlinear responses of matter. This gave birth to the field of *nonlinear* optics.

In our setup we used nonlinear optics techniques as a tool for the generation of light pulses at longer wavelength with rerspect to the forcing fields. Throughout this chapter I want to invite the reader to the world of nonlinear optics and to introduce him/her to a basic description of the nonlinear optical processes that we will use in the next chapters.

## 1.1 The basics

### 1.1.1 Nonlinear susceptibility

An electric field inside a medium is described by the set of Maxwell's equations:

$$\begin{cases} \nabla \cdot \vec{D} = \rho_f \\ \nabla \cdot \vec{B} = 0 \\ \nabla \times \vec{E} = -\partial_t \vec{B} \\ \nabla \times \vec{H} = \vec{J}_f + \partial_t \vec{D} \end{cases} \tag{1.1}$$

where $\vec{D} = \epsilon_0 \vec{E} + \vec{P}$ and $\vec{H} = \vec{B}/\mu_0 - \vec{M}$.
The induced polarization vector $\vec{P}$ is a function of the electric field $\vec{E}$, and for low-intensity fields

$$\vec{P}(t) = \epsilon_0 \chi^{(1)} \vec{E}(t)\,, \tag{1.2}$$

with $\epsilon_0$ the vacuum permittivity and $\chi^{(1)}$ a second-order tensor which does not depend on $\vec{E}$. Because of the linearity of the expression 1.2, the adimensional tensor $\chi^{(1)}$ is called linear (electric) susceptibility.

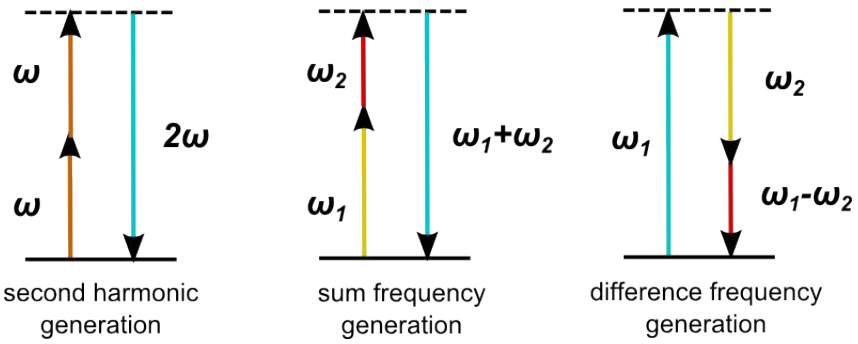


Figure 1.1: Energy diagram for some nonlinear processes.

More generally[1], the polarization can be written as

$$P = \epsilon_0 \left( \chi^{(1)} E + \chi^{(2)} E^2 + \chi^{(3)} E^3 + \dots \right) \equiv P^{(1)} + P^{(\mathrm{NL})} \,. \tag{1.3}$$

The last expression is written for scalar quantities, for the sake of simplicity; in the case of anisotropic materials the generalization is straightforward, and the coeffiecients $\chi^{(\mathrm{m})}$ become $(m+1)$-rank tensors. $P^{(\mathrm{NL})}$ is the nonlinear polarization, linked to the electric field through the nonlinear susceptibilities $\chi^{(\mathrm{m})}$, which are no more adimensional quantities. Their dimension is $[\mathrm{m/V}]^{(m-1)}$.

In order to show possible consequences of a nonlinear process, we can consider an electric field $\vec{E}(t) = \vec{E}_1(t) + \vec{E}_2(t)$ made of the superposition of two plane waves with angular frequency $\omega_1$ and $\omega_2$.

$$\vec{E}_1(t) = \vec{E}_1 e^{-i\omega_1 t} + \text{c.c.} \quad , \quad \vec{E}_2(t) = \vec{E}_1 e^{-i\omega_2 t} + \text{c.c.} \tag{1.4}$$

The second-order nonlinear polarization will therefore be

$$\begin{aligned} P^{(2)}(t) &= \epsilon_0 \chi^{(2)} \left[ \vec{E}(t) \right]^2 = \epsilon_0 \chi^{(2)} \left[ \vec{E}_1 e^{-i\omega_1 t} + \vec{E}_2 e^{-i\omega_2 t} + \text{c.c.} \right]^2 \\ &= \epsilon_0 \chi^{(2)} \Big[ |\vec{E}_1|^2 + |\vec{E}_2|^2 + E_1^2 e^{-2i\omega_1 t} + E_2^2 e^{-2i\omega_2 t} + E_1 E_2 e^{-i(\omega_1+\omega_2)t} + \\ &\qquad + E_1 E_2^* e^{-i(\omega_1-\omega_2)t} + \text{c.c.} \Big] \,. \end{aligned} \tag{1.5}$$

It contains terms oscillating at new frequencies. As we will see in the next paragraph, these terms act as sources for the electric field within the material. In Eq.1.5 we can recognize four behaviours, corrisponding to four different kind of nonlinear process (see also Fig. 1.1):

- the first two terms correspond to a DC field, and the process in known as *optical reptification*;
- the second two oscillate at $2\omega_1$ and $2\omega_2$, i.e. at the second harmonics of the incoming fields, and are thus the result of a *second harmonic generation* process;

[1] It happens that for very high electric fields near atomic resonances the series 1.3 does not converge. It is the case, exempli gratia, of Rabi oscillations in a two-levels atomic system forced by an oscillating electric field whose energy is tuned to the excitation energy of the atomic transition.

- the third oscillates at $\omega_1 + \omega_2$ and gives rise to a *sum frequency generation* process;
- the last one leads similarly to the *difference frequency generation* (DFG), since it oscillates at the difference frequency $\omega_1 - \omega_2$.

A sum frequency or second harmonic generation process is said to be of *upconversion*: the outcoming photons have higher energy with respect to the incoming photons. One could for example use an upconversion process to convert part of a visible laser beam into an ultraviolet one. A process involving the generation of a difference frequency is instead called *downconversion*.
In this thesis we will deal mainly with this latter case, which permits to create a field oscillating at a low frequency starting with fields at high frequencies, and thus allowing us to go first from the extreme red to the near-infrared and then from the near-infrared to the mid-infrared, lowering at each step the energy of the photons in the electromagnetic pulse.
The four processes mentioned above do not represent all the possible nonlinear processes, since we considered the nonlinear polarization only up to the second order.

As touched on in the introduction to the present chapter, the nonlinear polarization $P^{(\mathrm{NL})}$ starts to be significant when $E$ roughly approaches the order of magnitude of the atomic electric field $E_{\mathrm{at}}$, typically $E_{\mathrm{at}} \approx e/(4\pi\epsilon_0 a_0^2)$, where $a_0 = 4\pi\epsilon_0\hbar^2/(me^2)$ is the Bohr radius and $m$, $-e$ the mass and the charge of the electron respectively.

### 1.1.2 The wave equation

In this paragraph we want to derive from the equations 1.1, under reasonable assumptions, a wave equation that links electric field and nonlinear polarization in a nonlinear medium.
We limit ourselves to the case of a nonmagnetic material ($\vec{M} = 0$) in absence of free charge and free current ($\rho_f = 0$, $\vec{J}_f = 0$). Performing the curl of both right and left-hand side of the third equation in 1.1 and then using the fourth, we obtain:

$$-\nabla^2\vec{E} + \nabla(\nabla\cdot\vec{E}) = \nabla\times\nabla\times\vec{E} = -\partial_t\nabla\times\vec{B} = -\mu_0\partial_t\nabla\times\vec{H} = -\mu_0\partial_t^2\vec{D}\,. \quad (1.6)$$

Other than in linear optics, in our case the divergence of $\vec{E}$ does not vanish identically, because of the nonlinear term in the polarization field. Luckily, its gradient is usually negligible in most cases, notably when we can apply the so-called "slowly varying amplitude approximation" (see one of the next paragraphs). In that case

$$\nabla^2\vec{E} = \mu_0\partial_t^2\vec{D} = \mu_0\partial_t^2(\epsilon_0\vec{E} + \vec{P}) \equiv \frac{1}{c^2}\partial_t^2\vec{E} + \mu_0\partial_t^2\vec{P}\,. \quad (1.7)$$

It could be also written in the more elegant form

$$\Box\vec{E} = -\mu_0\partial_t^2\vec{P}\,, \quad (1.8)$$

where we introduced the D'Alembert operator $\Box \equiv (1/c^2)\partial_t^2 - \nabla^2$.
To see better what this equation means, it is useful to separate linear and nonlinear terms, so that $\vec{P} = \epsilon_0\chi^{(1)}\vec{E} + \vec{P}^{(\mathrm{NL})}$. Moving the first term to the left-hand side of Eq. 1.8 allows us to define the linear dielectric function $\epsilon^{(1)} = 1 + \chi^{(1)}$, and its

square root $n$, the linear refractive index ($n^2 = \epsilon^{(1)}$). The linear dielectric function links the linear electric displacement field to the electric field

$$\vec{D}^{(1)} = \epsilon_0 \epsilon^{(1)} \vec{E} \,. \tag{1.9}$$

Calling $\tilde{\Box}$ the D'Alembert operator for a wave travelling in a medium with group velocity $c/n$, the Eq. 1.8 reads

$$\tilde{\Box} \vec{E} = -\mu_0 \partial_t^2 \vec{P}^{(\mathrm{NL})} \,. \tag{1.10}$$

This is a stimulated wave equation, where the temporal variation of the nonlinear polarization represents the source term. If this term is vanishing, the solution is trivially a plane wave propagating with velocity $c/n$, whereas, if it is not negligible, it acts as a source, creating new electric fields. The equation 1.10 is an important equation for nonlinear optics and it predicts non-trivial results, such as the creation of electric fields with new wavelengths.

For the moment we assumed no dependence on the frequency, but it is well-known that media are dispersive, i.e. their refractive indexes are functions of the frequency of the propagating light. If we consider a wave-packet, $\vec{E}$ and $\vec{P}^{(\mathrm{NL})}$ can be expressed as sum of plane-waves with angular frequency $\omega_m$:

$$\vec{E}(t) = \sum_m{}' \left( \vec{E}_m e^{-i\omega_m t} + \text{c.c.} \right) \quad , \quad \vec{P}^{(\mathrm{NL})}(t) = \sum_m{}' \left( \vec{P}_m^{(\mathrm{NL})} e^{-i\omega_m t} + \text{c.c.} \right) . \tag{1.11}$$

The prime on the sum indicates that $m$ runs over positive integers only, and the complex coefficients $\vec{E}_m$ and $\vec{P}_m^{(\mathrm{NL})}$ are functions of the spatial coordinates.
Therefore the constitutive equation 1.9 becomes $\vec{D}_m^{(1)} = \epsilon_0 \epsilon^{(1)}(\omega_m) \vec{E}_m$. Here $\epsilon^{(1)}$ is a real tensor (which reduces to a scalar in the isotropic case) for a lossless medium, while it is complex for a dissipative medium.
Once we insert Eq. 1.11 in the wave equation 1.10, we find the latter valid frequency-by-frequency, i.e.

$$\tilde{\Box} \vec{E}_m = -\mu_0 \partial_t^2 \vec{P}_m^{(\mathrm{NL})} \,, \quad \forall m \,, \tag{1.12}$$

where $\tilde{\Box} = \tilde{\Box}(m)$, since the group velocity is frequency-dependent.

### 1.1.3 Phase matching

Consider now an interaction between two monochromatic collimated co-propagating continuous beams in a lossless medium with nonzero second-order nonlinear susceptibility. This is a fairly specific case of interaction, but the result presented at the end of the paragraph is quite general and of primary importance, and can be extended to pulsed beams too.
The two beams are both with wavevector $k_{1,2} = (n(\omega_{1,2})\omega_{1,2})/c$ along the $z$-axis, so that

$$E_{1,2}(t) = E_{1,2} e^{-i\omega_{1,2} t} + \text{c.c.} \equiv A_{1,2} e^{i(k_{1,2} z - \omega_{1,2} t)} + \text{c.c.} \,, \tag{1.13}$$

where $A_{1,2}$ are the ($z$-dependent) amplitudes of the field. Let us concentrate on the DFG polarization term in Eq. 1.5

$$P_3(t) \equiv P_{\mathrm{DFG}}^{(\mathrm{NL})}(t) = \epsilon_0 \chi^{(2)} A_1 A_2^* e^{i(k_1 - k_2)z} e^{-i\omega_3 t} + \text{c.c.} \equiv p_3 e^{i(k_1 - k_2)z} e^{-i\omega_3 t} + \text{c.c.} \,, \tag{1.14}$$

in which $\omega_3 \equiv \omega_{\mathrm{DFG}} = \omega_1 - \omega_2$. Since the nonlinear term in 1.12 is small, the solution for the field with frequency $\omega_3$ will be similar to a plane wave. We can thus make an ansatz supposing $E_3$ having a plane wave form, but with a $z$-varying amplitude

$$E_3(t) = A_3(z)e^{i(k_3 z - \omega_3 t)} + \text{c.c.}\,. \tag{1.15}$$

If the interaction between the two incoming waves in the material begins at $z = 0$ in absence of a pre-existing nonzero field at $\omega_3$, the boundary condition will be $E_3(z = 0) = 0.$, which is indeed the case we are most interested in. Substituting the ansatz form of $E_3(t)$ in the wave equation 1.12, leads us to

$$A_3''(z) + 2iA_3'(z)k_3 + \text{c.c.} = -\frac{\omega_3^2 p_3}{\epsilon_0 c^2} e^{i(k_1 - k_2 - k_3)z} e^{i\omega_3 t} + \text{c.c.}\,, \tag{1.16}$$

where the prime indicates the derivative with respect to $z$. The first term on the left hand side is in general much smaller than the second term, and therefore can be neglected.
The condition

$$|A''(z)| << |2k_3 A'(z)| \tag{1.17}$$

is known as *slowly varying amplitude approximation* and states that the rate of variation of the envelope function $A_3$ over distances comparable to the field wavelength is much smaller than unity. Under this approximation we get

$$A_3' = \frac{i\lambda_3 \omega_3^2 p_3}{4\pi\epsilon_0 c^2} e^{i\Delta k z}\,, \tag{1.18}$$

where we introduced the wavevector mismatch $\Delta k = k_1 - k_2 - k_3$, which is a crucial quantity in a nonlinear interaction.
In order to obtain a simple solution of the latter equation we make a further approximation, considering as constant the amplitudes $A_1$ and $A_2$ appearing in $p_3$. This means that we consider the case in which only a small part of the intensity of the two incoming beams in used to create the DFG beam, thus leaving them almost undepleted.
It is clear under these hypotheses that a vanishing wavevector mismatch maximizes the gain and the final amplitude of the DFG beam. If $\Delta k = 0$, $A_3$ grows linearly with $z$ (hence the intensity grows quadratically). The linear dependence with $z$, valid for small interaction length, is limited for long interaction length by the depletion of the pump field[2].
In nonlinear optics jargon the condition

$$\Delta k = 0 \tag{1.19}$$

is called *phase matching*. It is nothing but photon momenta conservation in the crystal, if we interpret the process as the annihilation of a photon at energy $\hbar\omega_1$ and the creation of two photons at energies $\hbar\omega_3$ and $\hbar\omega_2$, mediated by the crystal.

[2]Referring to the case dealt with so-far, of continuous laser light. If laser pulses are employed, additional parameters (notably, the temporal walk-off between the pulses, which is a consequence of the chromatic dispersion, and the spatial walk-off of different polarized pulses, which is a joint consequence of chromatic dispertion and birefringence of nonlinear crystal) limit the interaction length for which the $E_3(z)$ growth is linear with $z$.

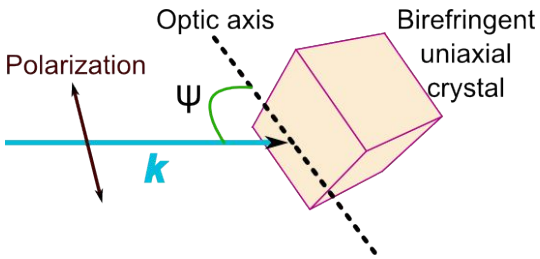


Figure 1.2: Here the polarization lies in the plane spanned by the wavevector and the optic axis. Therefore, the wave experiences the extraordinary refractive index $n_e(\psi)$.

### 1.1.4 Phase matching conditions in birefringent crystals

We derived the phase matching condition in the case of a DFG process, but its fullfillment is necessary for a large variety of nonlinear processes, such as second harmonic generation, sum frequency generation and four-wave mixing, in order for these processes to be efficient. When this condition is achieved, along all the length of the nonlinear crystal the contribution of the interaction with each dipole adds up in phase, and the final amplitude will be large. If $\Delta k \neq 0$ there is "coherent" interaction only over a lenght of about $2/\Delta k$.
In vacuum, a condition like 1.19 is trivially fulfilled once $\omega_3 = \omega_1 - \omega_2$ and the beams are parallel and spatially overlapped, but media are dispersive, as we said before, i.e. their refractive index is frequency dependent. Far from atomic resonances, the refractive index is a monotonically growing function[3] of $\omega$, and is said to be in its "normal region", where $n_1 > n_2$ when $\omega_1 > \omega_2$. Considering that $k = \omega n/c$ and $\omega_3 = \omega_1 - \omega_2$, we can rewrite Eq. 1.19 as

$$\omega_1 = \frac{n_2 - n_3}{n_1 - n_3}\omega_2 \,, \tag{1.20}$$

which is impossible to fulfill in the bulk normal region, since the fraction is smaller than unity.
The most common approach to overcome the problem resides in the employment of crystals showing birefringence. The most used birefringent crystal typically has an optic axis for which light propagating parallel or perpendicular to the plane spanned by the wavevector and the optic axis[4] experiences a different refractive index, $n_e$ and $n_o$ respectively. They are called "uniaxial". The origin of the subscripts is due to the fact that a beam with polarization along the optic axis is said to be *extraordinary polarized*, while in case of perpendicular polarization we talk about *ordinary polarization*. Uniaxial crystals can be either *negative* or *positive*, depending on whether $n_e$ is smaller or larger that $n_o$, respectively. Most common nonlinear birefringent crystals are negative uniaxial.

Therefore, in the DFG case, we can align the polarization of the beam oscillating at $\omega_1$ along the slowest axis, making $n_1 < n_2$ and —at least in principle— allowing for the fulfillment of the phase matching condition.
The aspects which allow to reach the phase matching over a broad range of wavelengths is the angular dependence of the extraordinary refractive index. With reference to Fig. 1.2, if we define $\psi$ as the angle between the wavevector and the optic

[3] Usually well described by the empirical Sellmeier formula.
[4] I.e. their polarization is parallel or perpendicular to the optic axis.

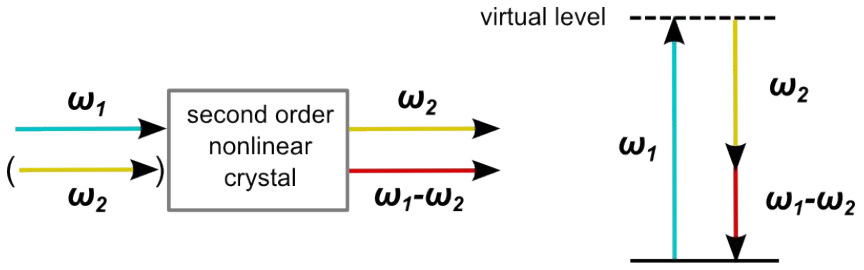


Figure 1.3: Scheme for downconversion and relative energy diagram. In an OPA $\omega_1$, $\omega_2$ and $\omega_1 - \omega_2$ are called pump, signal and idler respectively.

axis and $\tilde{n}_\mathrm{e} = n_\mathrm{e}(\psi{=}\pi/2)$, then

$$n_\mathrm{e}(\psi) = \frac{\tilde{n}_\mathrm{e}}{\sqrt{1 + \frac{\tilde{n}_\mathrm{e}^2 - n_\mathrm{o}^2}{n_\mathrm{o}^2}\cos^2\psi}}\,, \tag{1.21}$$

when the polarization lies in the wavevector-optic axis plane.
The coupled equations 1.20 and 1.21 can thus be solved for a wide set of frequencies just orienting the crystal in the right way with respect to the direction of the beams.

Furthermore, for a three-wave interaction there are two possible types of phase matching in an uniaxial crystal:

- Type I, if the two lowest energy fields share the same polarization;
- Type II, if their polarizations are orthogonal.

In paragraphs 1.2.3 and 1.2.4 we will discuss in details how to achieve phase matching in the cases of interest for this thesis.

## 1.2 Photon downconversion: OPA and DFG

### 1.2.1 Three-wave mixing downconversion

Difference frequency generation is an example of a photon downconversion process, a process in which photons at a higher energy are down-converted into photons at smaller energies, and it is also an example of three-wave mixing, since it is a second order process and involves three fields. Considering the second order processes, SFG and SHG are instead upconversion processes.
The typical downconversion process in represented in Fig. 1.3. From the practical point of view is important to distinguish two cases, in accordance to what outcoming field we are interested in: the optical parametric amplification (OPA) and the DFG.

In an OPA we have a high-intensity high-energy field, called *pump*, which is partially converted to a lower-energy *signal* beam; in the interaction a third beam is created, the *idler*, whose energy is the difference between the other two. In most cases the beam we are interested in is the signal. It is called optical parametric "amplification" because usually there is a low-intensity pre-existing field (the *seed*) at the frequency of the signal $\omega_\mathrm{s}$, which in the crystal "stimulates" the downconversion from the pump beam. The result of the parametric interaction is therefore a net amplification of

the seed beam. If there is no seed field before the crystal, the process can still occur —although typically with much smaller intensities— and can be described as an amplification of the vacuum fluctuations at frequency $\omega_s$ and $\omega_i$. Such process takes the name of spontaneous parametric downconversion (or *optical parametric superfluorescence*).
The difference between a spontaneous and a seeded optical parametric process[5] can be understood whithin the following corpuscolar description: a photon at frequency $\omega_p$ is "absorbed" by an atom, which first goes to an excited *virtual* level, and then decays to its ground level emitting two photonsat frequencies $\omega_s$ and $\omega_i$, as depicted in the right part of Fig. 1.3. The electronic state of the material does not undergo any real transition.

Unlike OPA, in a DFG the strengths of the two incoming beams are comparable, and the interest resides only in the outcoming difference-frequency beam, for which no seed is usually employed.

We want now to find a solution of the downconversion process in a more general case with respect to paragraph 1.1.2, and adopt the typical lexicon of the OPA. With reference to that paragraph, pump, signal and idler correspond to the fields '1', '2' and '3' (the DFG) respectively.
In the same way we derived Eq. 1.18 for the idler amplitude, it is possible to derive symmetric equations for the other two fields. We continue to work in the undepleted pump approximation, so that our set of coupled equations[6] will be

$$\begin{cases} A_p^{'} = \dfrac{2i\omega_p^2 d_{\text{eff}}}{k_p c^2} A_s A_i e^{-i\Delta k z} \approx 0 \\ A_s^{'} = \dfrac{2i\omega_s^2 d_{\text{eff}}}{k_s c^2} A_p A_i^* e^{i\Delta k z} \\ A_i^{'} = \dfrac{2i\omega_i^2 d_{\text{eff}}}{k_i c^2} A_p A_s^* e^{i\Delta k z} \,. \end{cases} \tag{1.22}$$

Here the quantity $d_{\text{eff}}$ appears, which is a sort of generalization of the second-order nonlinear coefficient, and takes into account the angles of incidence with respect to the optic axis of the crystal, and the type of phase matching[7].
Using the phase matching condition 1.19 and differentiating $A_i^{'}$ with respect to $z$, we obtain

$$A_i^{''} = \frac{2i\omega_i^2 d_{\text{eff}}}{k_i c^2} A_p A_s^{'*} = \frac{4\omega_i^2 \omega_s^2 d_{\text{eff}}}{k_i k_s c^4} |A_p|^2 A_i = \frac{4\omega_i \omega_s d_{\text{eff}}^2}{n_i n_s c^2} |A_p|^2 A_i \simeq \kappa A_i \,, \tag{1.23}$$

which has the simple general solution

$$A_i = \alpha \cosh(\kappa z) + \beta \sinh(\kappa z) \,. \tag{1.24}$$

[5] It should be noted that such a difference is basically the same occurring between stimulated and spontaneous emission in atomic physics.

[6] Defining the intensity of the beam as $I = 2n\epsilon_0 c|A|^2$, with a simple algebra we can also derive the equations $I_s^{'}/\omega_s = I_i^{'}/\omega_i = -I_p^{'}/\omega_p$, known as Manley-Rowe relationships. They can be interpreted as photon conservation laws.

[7] See [2] for a further discussion. In paragraph 1.1.2 we dealt with an isotropic crystal, for which $d_{\text{eff}}$ has no specific reason to be introduced. In that case the correspondence is simply $\chi^{(2)} = 2d_{\text{eff}}$. The correct formula is 1.22

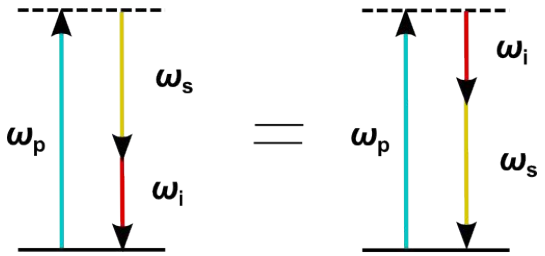


Figure 1.4: Reciprocity of the energy diagram under signal-idler exchange.

The specific solution that meets the boundary conditions $A_{\rm i}(z=0)=0$, $A_{\rm s}(z=0)=A_{\rm s}(0)$ is

$$\begin{cases} A_{\rm i} = i\sqrt{\dfrac{\omega_{\rm i} n_{\rm i}}{\omega_{\rm s} n_{\rm s}}}\dfrac{A_{\rm p}}{|A_{\rm p}|}A_{\rm s}^{*}(0)\sinh(\kappa z) \\ A_{\rm s} = A_{\rm s}(0)\cosh(\kappa z)\,. \end{cases} \tag{1.25}$$

We note that, for $\kappa z$ sufficiently large, both signal and idler grow exponentially $\propto \exp(\kappa z) = \exp(\text{const.}\times I_{\rm p} z)$, where $I_{\rm p}$ is the pump intensity[8]. An exponential regime is typical of those systems for which the products of the interaction are in turn sources of the interaction itself. In the downconversion the field at $\omega_{\rm s}$ stimulates the emission at $\omega_{\rm i}$, which in turn stimulates the emission at $\omega_{\rm s}$, as can be seen in Fig. 1.4. However, the exponential growth cannot stand indefinitely, considering that our solutions remain valid only under the undepleted pump approximation. For long crystals the intensities of signal and idler reach a saturation [5].
Moreover, from equations 1.25 it is important to point out that the signal field keeps its own phase, i.e. the phase of the seed, while the idler takes the difference of the phases between pump and signal, rotated by $\pi/2$. This aspect will be treated more in depth in the chapter 2, because it is crucial for the design of our setup.

### 1.2.2 Downconversion for ultrashort pulses

So far we treated only continuous waves, although our interest resides only in applications with pulsed lasers, with temporal widths from hundreds down to tenths of femtoseconds. Moreover, light pulses cannot be monochromatic, because of the uncertainty relation $\Delta t \Delta\text{Energy} \gtrsim \hbar$.

The electric field of a laser pulse (Fig. 1.5) can be described by slightly modifying equation 1.15, allowing the amplitude to vary with time. The temporal shape of the amplitude is the pulse *envelope*.

$$E = A(z,t)e^{i(kz-\omega t)} + \text{c.c.} \tag{1.26}$$

[8] Conversely, for small $z$, the signal is undepleted and the idler a linear function of $z$, in accordance with what we have seen in paragraph 1.1.3.

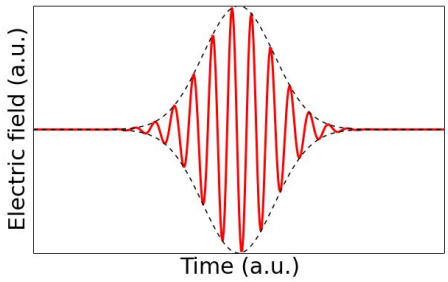


Figure 1.5: Electric field of a laser pulse (red solid line). The dashed line represents the envelope of the pulse. The full width at half maximum (FWHM) of the envelope is the *temporal width* of the pulse.

In the set of first-order equations 1.22 we insert the new term accounting for the time-derivative of the amplitude and obtain

$$\begin{cases} \partial_z A_\mathrm{p} + \dfrac{\partial_t A_\mathrm{p}}{v_\mathrm{gp}} = \dfrac{2i\omega_\mathrm{p}^2 d_\mathrm{eff}}{k_\mathrm{p} c^2} A_\mathrm{s} A_\mathrm{i} e^{-i\Delta k z} \\ \partial_z A_\mathrm{s} + \dfrac{\partial_t A_\mathrm{s}}{v_\mathrm{gs}} = \dfrac{2i\omega_\mathrm{s}^2 d_\mathrm{eff}}{k_\mathrm{s} c^2} A_\mathrm{p} A_\mathrm{i}^* e^{i\Delta k z} \\ \partial_z A_\mathrm{i} + \dfrac{\partial_t A_\mathrm{i}}{v_\mathrm{gi}} = \dfrac{2i\omega_\mathrm{i}^2 d_\mathrm{eff}}{k_\mathrm{i} c^2} A_\mathrm{p} A_\mathrm{s}^* e^{i\Delta k z} \,, \end{cases} \tag{1.27}$$

where $v_\mathrm{gj} = d\omega_\mathrm{j}/dk$ is the group velocity for the pulse centered at $\omega_\mathrm{j}$. This set of equations appears more clear when we transform to a frame of reference co-propagating with the pump pulse. If $\tau = t - z/v_\mathrm{gp}$ and we indicate with $\delta_\mathrm{jp} = |1/v_\mathrm{gj} - 1/v_\mathrm{gp}|$ the *group velocity mismatch* between the pump and the pulse with frequency $\omega_\mathrm{j}$, then

$$\begin{cases} \partial_z A_\mathrm{p} = \dfrac{2i\omega_\mathrm{p}^2 d_\mathrm{eff}}{k_\mathrm{p} c^2} A_\mathrm{s} A_\mathrm{i} e^{-i\Delta k z} \\ \partial_z A_\mathrm{s} + \left(\frac{1}{v_\mathrm{gs}} - \frac{1}{v_\mathrm{gp}}\right) \partial_\tau A_\mathrm{s} = \dfrac{2i\omega_\mathrm{s}^2 d_\mathrm{eff}}{k_\mathrm{s} c^2} A_\mathrm{p} A_\mathrm{i}^* e^{i\Delta k z} \\ \partial_z A_\mathrm{i} + \left(\frac{1}{v_\mathrm{gi}} - \frac{1}{v_\mathrm{gp}}\right) \partial_\tau A_\mathrm{i} = \dfrac{2i\omega_\mathrm{i}^2 d_\mathrm{eff}}{k_\mathrm{i} c^2} A_\mathrm{p} A_\mathrm{s}^* e^{i\Delta k z} \,. \end{cases} \tag{1.28}$$

In the hypothetic case of no group velocity mismatch, the amplification follows the same equations as in the case of continuous waves, but in real materials chromatic dispersion (and hence group velocity mismatch) cannot be neglected, and equations 1.28 tell us that the parametric interaction lasts until the three pulses are superposed, so only for finite calculable lengths. The "critical" length, called *pulse splitting length* is

$$\ell_\mathrm{jp} = \frac{\Delta t}{\delta_\mathrm{jp}} \,, \tag{1.29}$$

with $\Delta t$ duration of the pulses[9] and j labelling either the signal or the idler. The splitting length depends on pump wavelength, phase matching, dispersion of the material and pulse duration.

[9] If the two pulses have different temporal widths, the $\Delta t$ in Eq. 1.29 represents the average of the two temporal widths.

| | | |
|---|---|---|
| $\chi^{(2)}$@850 nm | 4.6 | pm/V |
| $\chi^{(2)}$@1064 nm | 4.4 | pm/V |
| $n_o$@800 nm | 1.661 | |
| $\tilde{n}_e$@800 nm | 1.546 | |
| Damage threshold | | |
| @800 nm&$\Delta t = 10$ fs | 25 | GW/cm$^2$ |
| Transparency range | 190−3500 | nm |
| Transition point | 925 | °C |
| Point group | $C_{3v}$ | |

Table 1.1: Properties of BBO. $\Delta t$ indicates the temporal width of the pulses; the smaller the width, the higher the damage threshold, in general. The crystallographic phase $\beta$ of the barium borate exists only below the transition temperature. For temperatures between the transition and the melting point (1095 °C) the crystal stays in its $\alpha$ phase. The symmetries of the $C_{3v}$ point group are (i) the identity, (ii) a 3-fold axis, (iii) 3 vertical mirror planes.

Whether $\delta_{sp}$ and $\delta_i$ have equal or opposite sign, the amplification shows different behaviour. Indeed, if they have the same sign, the gain rapidly saturates for lengths larger than the smaller splitting length, while, if they have opposite signs, the amplification continues even for very large lengths compared to the splitting length. This can be understood in the following way: if, e.g., the idler goes faster, then it stimulates the emission of signal-idler photon pairs from the front part of the pump pulse; the signal photons —which are slower— go through the peak of the pump pulse and in turn stimulate the downconversion. Viceversa, the idler photons produced in the back part of the pump pulse (via the stimulation of the signal pulse) are faster, and go throught the peak of the pump pulse, again stimulating the downconversion.

### 1.2.3 Optical parametric amplification (OPA) in a BBO crystal

A suitable nonlinear crystal for OPA should have the following characteristics:

- Transparency over the spectral range of pump, signal and idler;
- Large second-order nonlinear susceptibility;
- A birefrengence that allows to reach the phase matching condition;
- Not-too-high group velocity mismatch;
- High electromagnetic damage threshold, as well as good mechanical and chemical properties.

One of the most used crystal for OPA application in the near-infrared range[10] is $\beta$-$BaB_2O_4$ (beta-barium borate, BBO), which fits well the characteristics listed above. Its principal properties are listed in table 1.1. In order to be as clear as possible, we re-write the conservation equations that describe the OPA.

$$\begin{cases} \hbar\omega_p = \hbar\omega_s + \hbar\omega_i & \text{(energy conservation)} \\ \hbar\vec{k}_p = \hbar\vec{k}_s + \hbar\vec{k}_i & \text{(momentum conservation)} \end{cases} \tag{1.30}$$

[10] Typically pumping at 800 nm or 1064 nm, with Ti:sapphire and Nd:YAG lasers respectively.

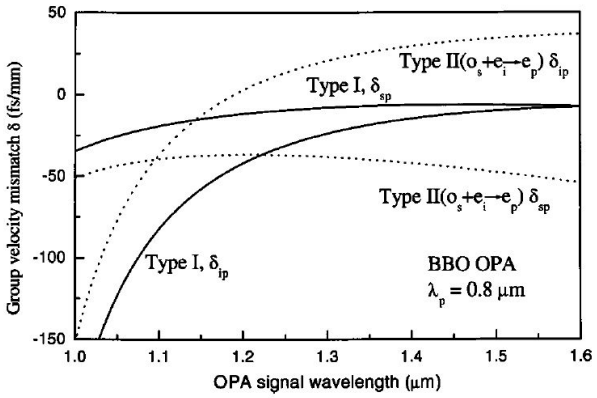


Figure 1.6: Group velocity mismatch curves ($\delta_{\mathrm{sp}}$ for signal-pump and $\delta_{\mathrm{ip}}$ for idler-pump) as functions of the signal wavelength, at fixed pump wavelength $\lambda_{\mathrm{p}} = 800\,\mathrm{nm}$. Solid and dashed lines are for type-I and type-II phase matching respectively. Figure reproduced by [5].

In addition to the the conservation laws, the three pulses have to coincide in space and in time in a suitable crystal. The group velocity mismatch is usually low in the near-infrared range, and for type-II phase matching $\delta_{\mathrm{sp}}$ and $\delta_{\mathrm{ip}}$ have opposite sign (see Fig. 1.6), allowing exponential amplification over a length well exceeding the pulse splitting length, as discussed in paragraph 1.2.2. Crystals as long as 8 mm can hence be used for collinear OPAs.
Although for type-I phase matching the pulse splitting length is larger, the effective interaction length does not exceed 5 mm. We should mention also that, using a phase matching of type-II, signal and idler are easily separable because of their orthogonal polarizations.

Furthermore, near-infrared OPAs can be pumped at 800 nm, the emission line of Ti:sapphire lasers, which usually have very high energy. This allows to build near-infrared OPAs with pulse energies up to the multi-mJ level [23].
Since BBOs absorb wavelengths larger than about 3 µm, the smallest signal wavelength achievable is around 1.1 µm, and hence the tunability is limited to the $[1.1, 3]\mu\mathrm{m}$ range.

### Noncollinear OPA for ultrashort pulse generation

A seeded OPA allows also a noncollinear interaction geometry, at least for angles small enough, and in that case its name is shortened in NOPA (noncollinear optical parametric amplifier). With reference to Fig. 1.7, let $\alpha$ be the angle formed by the seed (and hence the signal) and the pump, and $\Omega$ the angle between signal and

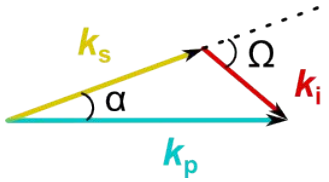


Figure 1.7: Phase matching for a noncollinear OPA (NOPA).

idler, in the phase matched case. At fixed $\alpha$, $\Omega$ depends on the signal wavelength. When the interaction is collinear, both angles are zero, and the phase matching condition is achievable only over a narrow bandwidth, because different signal wavelengths correspond to different internal angles of the crystal. This fact limits the bandwidth generated by a collinear OPA and, therefore, no pulses below 50 fs are commonly produced with such scheme. The introduction of the noncollinear interaction overcomes such limitation, and broadband signals can be generated, allowing the production of sub-10 fs, after a suitable chirp correction.
It is useful to write the projections of the vectorial phase matching conditions on the parallel and orthogonal directions, with respect to the propagation direction of the signal.

$$\begin{cases} \Delta k_{\parallel} = k_{\mathrm{p}} \cos\alpha - k_{\mathrm{s}} - k_{\mathrm{i}} \cos\Omega = 0 \\ \Delta k_{\perp} = k_{\mathrm{p}} \sin\alpha - k_{\mathrm{i}} \sin\Omega = 0 \end{cases} \tag{1.31}$$

If 1.31 is verified for a given signal frequency $\omega_{\mathrm{s}}$, then for $\omega_{\mathrm{s}}^{'} = \omega_{\mathrm{s}} + \delta\omega_{\mathrm{s}}$ we can expand to first order the phase matching equations, remembering that $\delta\omega_{\mathrm{i}} = -\delta\omega_{\mathrm{s}}$ and $v_{\mathrm{g}} = \partial_k \omega$, finding

$$\begin{cases} \Delta k_{\parallel} \simeq -v_{\mathrm{gs}}^{-1} + v_{\mathrm{gi}}^{-1} - k_{\mathrm{i}} \sin\Omega \partial_{\omega_{\mathrm{i}}} \Omega = 0 \\ \Delta k_{\perp} \simeq v_{\mathrm{gi}}^{-1} \sin\Omega + k_{\mathrm{i}} \cos\Omega \partial_{\omega_{\mathrm{i}}} \Omega = 0\,, \end{cases} \tag{1.32}$$

which has a solution for

$$v_{\mathrm{gs}} = v_{\mathrm{gi}} \cos\Omega\,. \tag{1.33}$$

It states that the projection of the idler group velocity along the signal direction must be equal to the signal group velocity. We can thus obtain a broadband OPA choosing an $\alpha$ which verifies Eq. 1.33 for the central signal wavelength. Only type-I phase matching can be adopted if we use BBO crystals, since Eq. 1.33 has a solution if and only if $v_{\mathrm{gi}} > v_{\mathrm{gs}}$ (see Fig. 1.6 for the group velocity mismatches). For the suitable $\alpha$, both signal and idler are broadband, but the spectral components of the idler are angular dispersed, and thus it is more difficul to handle with the idler and compress it to its Fourier limit.

### 1.2.4 Difference frequency generation (DFG) in a GaSe crystal

The equations describing a difference frequency generation (DFG) process are formally equivalent to the ones for an OPA. Nonetheless, we rewrite Eq. 1.30 to stress that here we are now interested mainly in the outcoming DFG beam.

$$\begin{cases} \hbar\omega_{\mathrm{DFG}} = \hbar\omega_1 - \hbar\omega_2 & \text{(energy conservation)} \\ \hbar\vec{k}_{\mathrm{DFG}} = \hbar\vec{k}_1 - \hbar\vec{k}_2 & \text{(momentum conservation)} \end{cases} \tag{1.34}$$

We want to focus our attention in a DFG in the mid-infrared (MIR), starting form two beams in the near-infrared range. The limited range of transparency makes BBOs unsuitable for the scope. Most common MIR nonlinear crystals are GaSe, $AgGaS_2$, $AgGaSe_2$, CdSe and $ZnGeP_2$. Among them, GaSe, which is transparent up to 18 µm, allows to produce DFG pulses at the largest wavelengths. It is a negative uniaxial second-order nonlinear crystal with a high damage threshold and a hexagonal layer structure, used both to generate and detect MIR pulses. Some of its properties are listed in table 1.2. GaSe was used with success in many MIR

| | | |
|---|---|---|
| $\chi^{(2)}$ | 54 | pm/V |
| $n_o$@10.6 µm | 2.697 | |
| $\tilde{n}_e$@10.6 µm | 2.374 | |
| Transparency range | $0.65 \sim 18$ | µm |
| Point group | $D_{3h}$ | |

Table 1.2: Properties of GaSe. The symmetries of $D_{3h}$ point group are (i) the identity, (ii) a 3-fold axis, (iii) 3 $C_2$ axis, and (iv) a $\sigma_h$ mirror plane.

downconversion schemes [14], and —using very thin crystals— to produce also low-intense pulses in the far-infrared range (known as terahertz (THz) range) [10].

## 1.3 Four-wave mixing and white-light generation

There are two commonly used approaches to seed optical parametric amplifiers. One exploits the *parametric superfluorescence*. In those systems, a first OPA amplifies the vacuum fluctuations, and the resulted signal serves as seed for a second equally phase-matched OPA, where the amplification really takes place. The second (most used) approach uses the generation of a *continuum of white light* (white-light generation, WLG). The seeding of the OPA is made with a selected portion of the white light spectrum.
OPAs seeded by the white light produced in a first stage by parametric superfluorescence are commonly more unstable, since parametric superfluorescence originates from quantum noise. More importantly, as discussed in chapter 3, our approach requires a high phase stability for the seed light and in parametric superfluorescence the phase of different pulses is random, not depending on the phase of the pump pulses. On the other hand, white-light generation allows to form beams with high spatial quality and mapping pulse-by-pulse the phase of the pump.
In our setup we used white light seeding, as it is done also in most of the recently produced commercial OPAs.

Every centrosymmetric crystal has a vanishing $\chi^{(2)}$, but no crystal has a vanishing third-order nonlinear susceptibility $\chi^{(3)}$. This follows from the general equation 1.3. In a centrosymmetric crystal, if the sign of $\vec{E}$ is inverted, the polarization should also change sign. Then all the even term in the Taylor expansion 1.3 must vanish. In centrosymmetric crystals the lowest order nonlinear term is thus the third, which for example gives rise to third harmonic generation. Third-order nonlinear interactions are also called *four-wave mixing*.
A third-order nonlinear polarization implies a second-order field-dependent refractive index

$$n = n(I) = n_0 + n_2 I(\vec{r}, t)\,, \tag{1.35}$$

where $I = 2n_0\epsilon_0 c|A(\vec{r}, t)|^2$ is the electric intensity and $n_2$ is usually positive. This is known as *optical* Kerr effect, because of the strict analogy with the Kerr effect, in which an applied DC electric field modifies quadratically the refractive index.
The optical Kerr effect is responsible for both of the optical nolinear effects underneath the generation of white-light continua: self-focusing and self-phase modula-

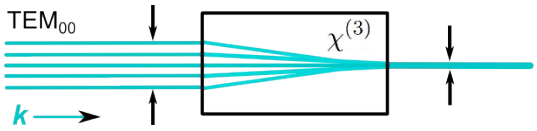


Figure 1.8: Schematic representation of self-focusing. The box represents a suitable Kerr medium, while the black arrows mark the spatial FWHM.

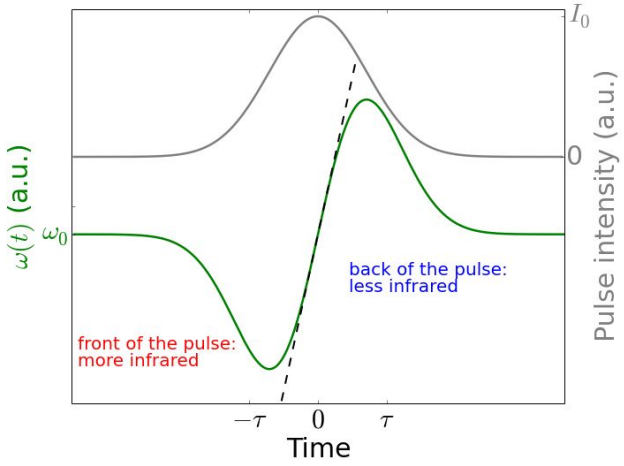


Figure 1.9: Frequency $\omega(t)$ in a self-phase modulated pulse (green, left axis). In the right axis the intensity $I_0 e^{-t^2/\tau^2}$ of the pulse envelope is plotted (grey). The dashed line indicates the linearity of the chirp. In the wings of the pulse, the linearity is lost, but the corrsponding intensity is small (HWHM$\simeq 0.7\tau$), and thu, in first approximation, we can consider the chirp as linear.

tion.

**Self focusing** (see Fig. 1.8) is due to the creation —via the optical Kerr effect— of an effective lens inside the material, which is responsible of the focalization. If we consider a collimated beam propagating along the $z$-axis and whose transverse spatial section is purely Gaussian (TEM$_{00}$),

$$I = I_0 e^{-2\rho^2/w_0^2}\,, \tag{1.36}$$

then we see that the refractive index 1.35 has also a Gaussian shape, larger in the center and smaller in the tails (being $\rho$ the distance from the center of the transverse section). The material acts therefore as a converging lens.
Self-focusing allows to reach extremely high electric fields in very localized regions, reaching filamentation regimes and eventually the damage threshold of the material.

**Self-phase modulation** (SPM) takes into account the temporal variation of $n(I)$, which in the simplest case is

$$n(t) = n_0 + n_2 I_0 e^{-t^2/\tau^2}\,. \tag{1.37}$$

As we know, $-\omega$ is the time-derivative of the phase $\phi$ of the field, and thus —for a material long $d$—

$$\omega(t) = -\frac{d}{dt}\phi = \frac{d}{dt}\left(\omega_0 t - \frac{n(t)\omega_0}{c}d - \Phi\right) = \omega_0\left(1 + \frac{2dn_2 I_0}{c\tau^2}te^{-t^2/\tau^2}\right) \equiv \omega_0 + \delta\omega(t)\,. \tag{1.38}$$

New frequencies are therefore created, and self-phase modulation results in a broadening of the spectrum. The white light pulses are intrinsically chirped: larger wavelengths stay in the front of the pulse, smaller wavelengths in the back, as shown in Fig. 1.9. The spectrum is often very large, and that is why the light generated by SPM is said to form a *white light continuum*, or sometimes even *supercontinuum*. As anticipated, the overall process is therfore known as *white-light generation* (WLG). It should be noted that SPM occurs only if the intensity is high, and for this reason the self-focusing effect is important.

Self-phase modulation is a process that preserves the phase of the electric field, and hence the phase before the crystal is mapped pulse-by-pulse in the phase after the crystal, apart from a constant.

The most commonly used crystals for SPM include sapphire ($Al_2O_3$) and YAG (Yttrium Aluminium Garnet). The infrared tail of the white light spectrum extends up to 1.5-1.6 µm, and can be used to seed an OPA working in the near-infrared. In paragraph 3.2.1, will discuss the optical Kerr media that better suit our requests.

Self-phase modulation is also responsible for the large spectral broadening in noble gas filled-hollow waveguides. We will treat this interesting aspect in section 3.3.

# Chapter 2

# The carrier-envelope phase

## 2.1 Definition

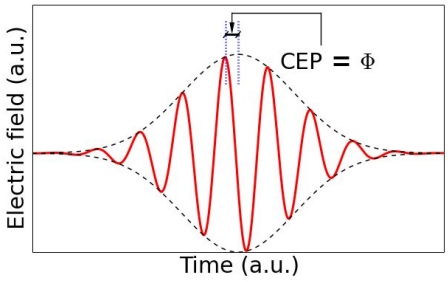


Figure 2.1: A laser pulse and the definition of the carrier-envelope phase (CEP).

For a few-cycles laser pulse it is fundamental to introduce the carrier-envelope phase (CEP), a quantity defined as the difference between the positions of envelope and electric field maxima (converted in radians), as depicted in Fig. 2.1. If $A(t)$ is the envelope and $E(t) = A(t)\cos(\omega t + \Phi)$ the electric field, then $\Phi$ represents the CEP. For short-wavelength pulses, which usually contain many carrier cycles, a CEP shift does not modify substantially the shape of the electric field, but, for large wavelength and few-cycles pulses, it does. In Fig. 2.2 we can appreciate the modification of the pulse caused by CEP shifts in the two cases.

The definition given above is not formally rigorous, since —at least in principle— different frequencies within the pulse could have different phases. We can thus define the CEP at frequency $\omega$ as the phase of the oscillatory contributions to the pulse at frequency $\omega$, measured with respect to the maximum of the envelope. We indicate it as $\Phi_\omega$. In some cases we will make use of this distinction, but in most cases the first definition will be enough.

The problem is that usually the pulses generated in the laser oscillator are not pulse-to-pulse CEP-stable. Successive pulses have the same shape and spectral content, but an almost random CEP. The origin of the instability is twofold. From one side the difference between group and phase velocity[1] in the cavity introduces a phase slippage $\Delta\Phi$ with respect to the envelope, after one roundtrip. When $\Delta\Phi$ is not an integer multiple of $2\pi$, it acts as to shift at each pulse the position of the maxima of the electric field within the envelope. On the other side, $\Delta\Phi$ is not constant, due to the unavoidable mechanical nanometric instability of the cavity parameters.

[1] defined as $\partial\omega/\partial k$ and $\omega/k$ respectively. They are different when the pulses travel through a dispersive medium.

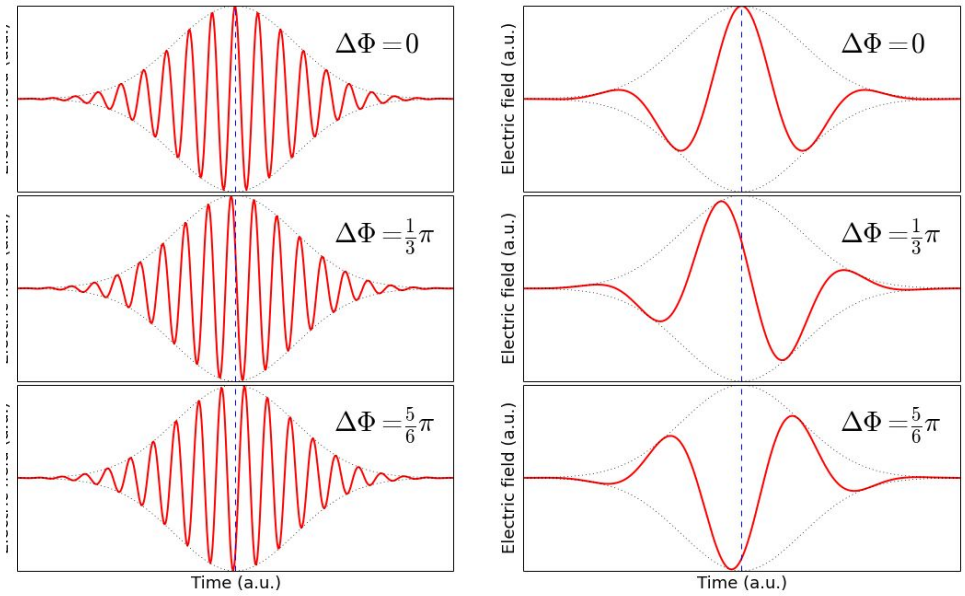


Figure 2.2: Laser pulses with many cycles (left) and roughly a single cycle (right), for different CEP values. In the latter case, a variation in the phase between carrier and envelope changes dramatically the shape of the electric field.

Not every physical phenomenon is CEP-sensitive, and so random-CEP pulses are commonly used with success in a large variety of experiments. However, in light-matter interaction the coupling depends directly on the electric field, and so the CEP should definitely play an important role, at least if few-cycles pulses are employed. The first experimental evidence of a CEP-dependent behaviour involving ultrashort pulses (the angular dependence of above-threshold ionized electrons) did not require any phase-stabilization [15], but if we want to observe a CEP-sensitive effect in a pump-probe experiment, it would be almost compulsory[2]. Indeed, as most of pump-probe spectroscopy experiments cannot be performed with single pulses, if random-CEP pulses are employed, the measurement will average the random contributions, making impossible the detection of a phase-sensitive signal.

## 2.2 CEP stabilization schemes

Many schemes were developed to achieve CEP-stability for near- and mid-infrared ultrashort laser pulses. We can classify the methods in two main branches, the active and the passive.

[2]Unless the case in which both CEP and pump-probe measurements are performed pulse by pulse, which is, for the CEP, rather complex, even though possible (see for example [16] for a single pulse CEP measurement). To our knowledge, no single-shot time-domain experiments with CEP sensitivity were ever performed.

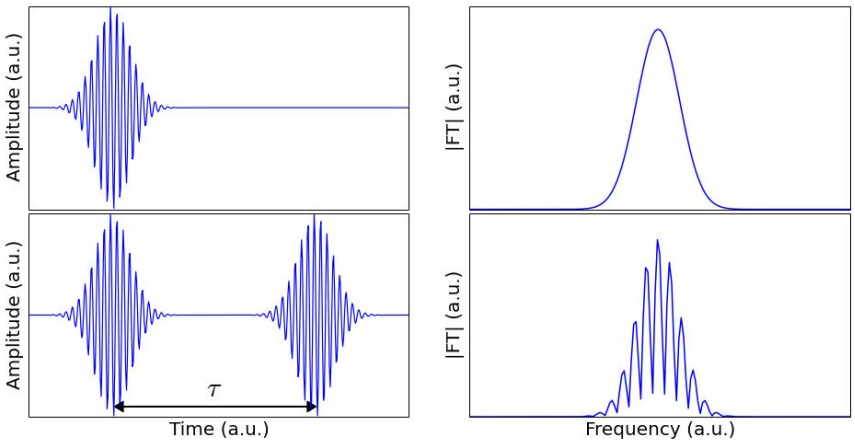


Figure 2.3: Top line: an isolated pulse and its Fourier transform (FT). Bottom line: a train of two identical pulses, separated by a time $\tau$, and the relative FT. The interference fringes are separated by the "repetition" frequency $1/\tau$.

### 2.2.1 Active methods

In active methods, a feedback on the coordinates of a cavity mirror stabilizes $\Delta\Phi$. The phase stability is commonly obtained by means of a frequency-domain stabilization approach. Indeed, even if it is easier to represent the CEP in time-domain, it has a fundamental importance in frequency-domain measurements [24].
In the top part of Fig. 2.3 we see the Fourier transform of an isolated pulse, while in the bottom part there is the transform of two pulses separated by a time $\tau = 1/f_{\text{ref}}$, where $f_{\text{ref}}$ is the laser oscillator's repetition rate. In this latter case, the pulses interfere, adding constructively only for those modes which have a phase shift of $2n\pi$, i.e. when $\omega_n\tau - \Delta\Phi = 2n\pi$. This means $f_n = nf_{\text{rep}} + (\Delta\Phi/2\pi)f_{\text{rep}} = nf_{\text{rep}} + \delta$, with $\omega_n = 2\pi f_n$. We introduced $\delta = f_{n=0}$ as the comb shift with respect to integer multiples of the repetition rate, and it is linked with the phase slippage by the relation $2\pi\delta = \Delta\Phi f_{\text{rep}}$. So, even in a repetition rate-locked laser the phase-group velocity difference drifts with time, because of the $\delta$ term. Only controlling both $f_{\text{rep}}$ and $\delta$, $\Delta\Phi$ will be under control. A precise control of the translation of a mirror inside the cavity permits to control the repetition rate, while —since the light has a spatial chromatic disperion— a tilt of the mirror introduces a linear phase change with frequency, therefore modifying also $\delta$. It is then just a matter of fine tuning to set $\Delta\Phi = 0$, modulus $2\pi$.
Summarizing, $f_{\text{rep}}$ and $\delta$ are first measured, and then a "fast" feedback loop controls tilt and position of the cavity mirror, making $\Delta\Phi$ a pulse-to-pulse stable multiple of $2\pi$ [9].
Also the cavity of the amplifier introduces a CEP drift. In this case the CEP is measured and a "slow" feedback loop corrects the fluctuations. The active feedback methods (such as the one explained above) are able to achieve a long-term CEP-stability. In addition to the feedback methods, also a feed-forward approach was experimentally proven [12] to work.

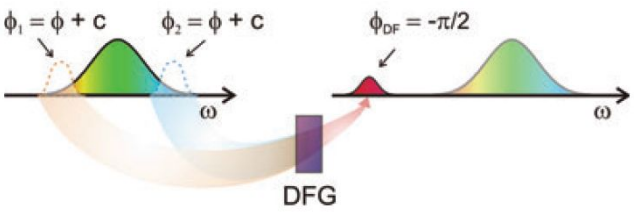


Figure 2.4: Intrapulse DFG. Adapted from [6].

### 2.2.2 Passive methods

Passive methods use nonlinear processes to stabilize the CEP. A first advantage of passive methods with respect to active ones is that they are all-optical, with no need of any electronic feedback circuit. Furthermore, they work at any repetition rate. Before talking thoroughly about passive methods, let us see how CEP changes in some nonlinear processes.
In the three-wave mixing $\omega_\mathrm{p} - \omega_\mathrm{s} - \omega_\mathrm{i} = 0$, the phases are linked by the relation

$$\Phi_\mathrm{p} - \Phi_\mathrm{s} - \Phi_\mathrm{i} = \text{const.} \tag{2.1}$$

For the downconversion treated in paragraph 1.2.1 the constant is $-\pi/2$. In effect from equations 1.25 we directly see that $\Phi_\mathrm{s} = \Phi_\mathrm{seed}$ and $\Phi_\mathrm{i} = \Phi_\mathrm{p} - \Phi_\mathrm{seed} + \pi/2$, which verifies Eq. 2.1 with const.$= -\pi/2$.
We can then conclude that, if pump and seed possesses the same carrier-envelope phase, the difference-frequency (idler) wave will be automatically phase-locked, regardless of the pulse-to-pulse instability of pump and seed. This is precisely the basis of passive methods.
As we pointed out in section 1.3, white-light generation (WLG) can be seen as a near-degenerate four-wave mixing in a Kerr medium, in which $\omega_\mathrm{WLG} = \omega_1 - \omega_2 + \omega_3$, with $\omega_{1,2,3}$ three frequency belonging to the same pulse. Following paragraph 1.1.3, the third-order nonlinear polarization is $P_\mathrm{WLG} \propto A_1 A_2^* A_3$, and within the slow varying amplitude approximation 1.17

$$A_\mathrm{WLG} \propto -iA_1 A_2^* A_3\,, \tag{2.2}$$

analogous to Eq. 1.18 after an integration.
Hence $\Phi_\mathrm{WLG} = \Phi_{\omega_1} - \Phi_{\omega_2} + \Phi_{\omega_3} - \pi/2$, which reduces to the case $\Phi_\mathrm{WLG} = \Phi - \pi/2$ in the case in which the three frequency components within the pulse share the same phase $\Phi_{\omega_1} = \Phi_{\omega_2} = \Phi_{\omega_3} \equiv \Phi$.

We can distinguish two different passive methods, based on *intrapulse* and *interpulse* difference frequency generation respectively. In the former case the mixing occurs between two frequencies of a single broadband pulse, as sketched in Fig. 2.4. The latter is instead represented in Fig. 2.5. In an optical parametric amplifier (OPA), if the seed is provided by a WLG process driven by a fraction of the pump pulse, the idler does show CEP stability. Conversely, if the seed is generated by parametric fluorescence, no phase stability can be achieved. Some cases are represented in Fig. 2.6.

A possible method working in the near-infrared range is the following (Fig. 2.7): the pump beam is split in three; the first beam goes to a WLG stage, which seeds an OPA pumped by the second pump beam. The idler is taken and used to seed

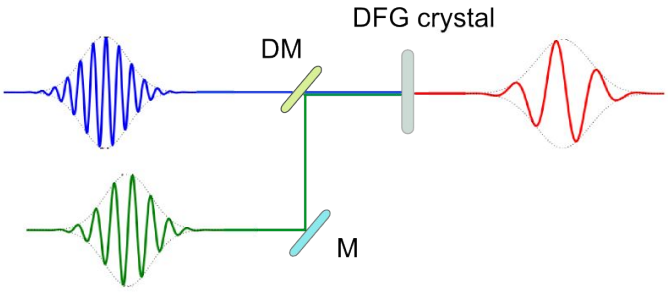


Figure 2.5: Interpulse DFG. M: mirror; DM: dichroic mirror.

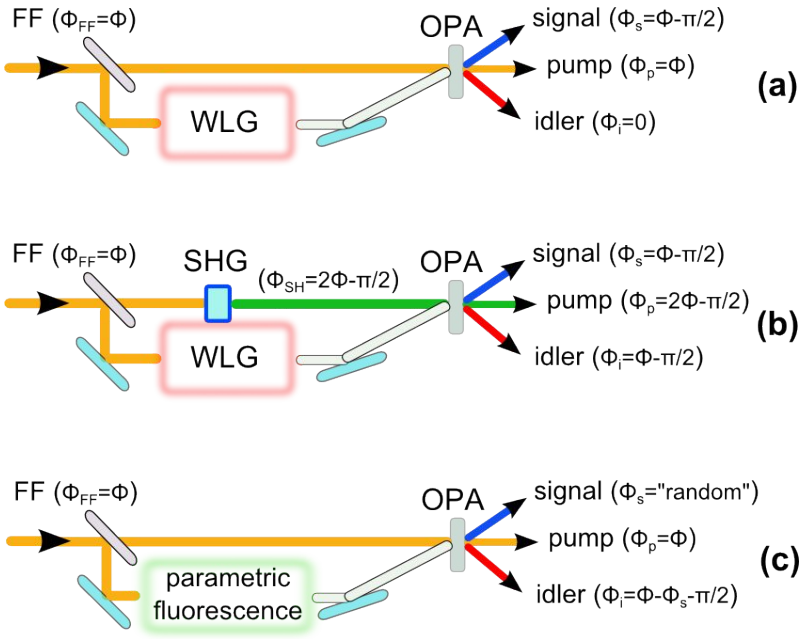


Figure 2.6: Three possible cases of OPA, with indication of the CEP of the involved pulses. The noncollinear geometry interaction is chosen for clarity purposes. **(a)**: The laser fundamental frequency (FF) drives the white-light generation process (WLG), which seeds the optical parametric amplification (OPA) process, pumped by FF. The carrier-envelope phase (CEP) of the idler is locked to zero, while the signal takes substantially the phase of FF. **(b)**: A second harmonic generation (SHG) crystal is placed on the pump path (no modification occuring to the seed generation), and the idler is no more phase stabilized. Signal and idler share the same CEP, and thus if they are used in a further difference frequency generation process, the generated difference-frequency pulses would be CEP-stable. In the case (not represented here) in which the SHG stage is placed before the beam splitter for WLG, we return to case (a), athough with different generated frequencies. **(c)**: When the seed is generated thanks to parametric fluorescence, the phase of idler and signal varies from pulse to pulse in a non predictable manner, and for this reason their CEPs are "random".

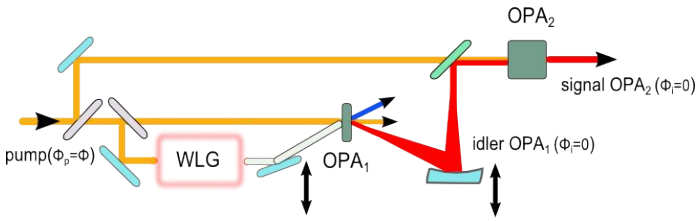


Figure 2.7: Experimental sketch for a near-infrared CEP stable optical parametric amplifier, as described in the text.

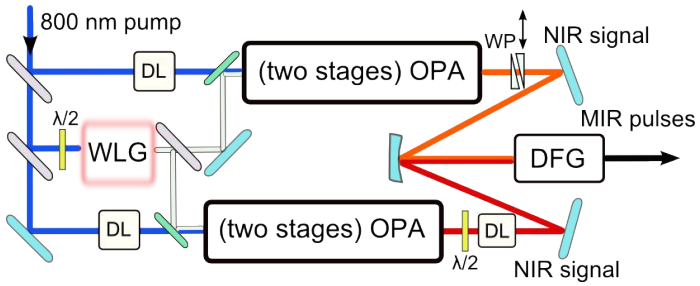


Figure 2.8: Conceptual representation of a twin-OPAs + DFG all-optical passive CEP stabilization scheme, as described in the text. The half-wave plates ($\lambda/2$) rotate the electric polarization, in order to make possible the achievement of the phase matching conditions. "DL" boxes represent delay lines, and WP indicates a pair of wedge plates (see Fig. 2.9), whose presence is not compulsory, but helps to achieve long-term CEP stability.

a second OPA, pumped by the third beam. The signal of the latter OPA is then CEP-stable.

Many other schemes are possible, in visible, near- and mid-infrared ranges, but we cannot cite all of them, which are accurately reviewed, for example, in [6].

We now focus on the scheme we implemented in our setup, the so-called **twin-OPAs+DFG** scheme, whose ouput pulses lie in the mid-infrared spectral region. Its conceptual diagram is sketched in Fig. 2.8. It consists of two symmetric OPAs seeded by the same white light, generated by a fraction of the pump beam. The OPAs have two stages, in order to maximise the output signal power. The CEP of the pump maps itself in the CEP of the seed ($-\pi/2$), and the signal of the first stage OPA inherits the CEP of the seed. The same for the signal of the second stage OPA, seeded by the signal of the first stage and pumped by a residual part of the pump. If $\Phi$ is the CEP of the pump and $\Phi_{s,1}$, $\Phi_{s,2}$ the CEPs of the near-infrared signals of OPA1 and OPA2 respectively, then

$$\Phi_{s,1} = \Phi + c_1 \quad \text{and} \quad \Phi_{s,2} = \Phi + c_2\,, \tag{2.3}$$

with $c_1$ and $c_2$ constant phases accumulated in the optical paths. The last stage consists in a DFG between the two signals. Assuming $\omega_{s,1} > \omega_{s,2}$, the CEP of the mid-infrared DFG pulses will be

$$\Phi_{\mathrm{DFG}} = \Phi_{s,1} - \Phi_{s,2} + \pi/2 = c_1 - c_2 + \pi/2 = \text{const.}\,, \tag{2.4}$$

constant for successive pulses —regardless the pump pulse-to-pulse CEP stability. The stability of the mid-infrared pulses generated with this scheme (here described theoretically) was experimentally tested in [23] and [14]. They found on one side

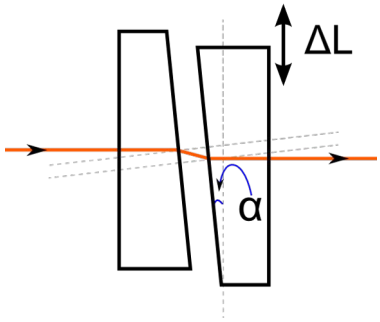


Figure 2.9: Beam propagation through a pair of wedge plates. They are made of a transparent material, usually glass, for visible and infrared light. When one of the two wedge plates is moved by $\Delta L$ in the direction orthogonal to the beam propagation, the optical path is changed by $\delta\ell = n\Delta L \tan\alpha \simeq \Delta L\alpha$, with an extraordinary precision (if $\alpha = 0.5°$, a movement $\Delta L = 20\,\mu\text{m}$ induces a change of optical path $\delta\ell \simeq 300\,\text{nm}$), without affecting the spatial position of the outcoming beam.

an excellent pulse-to-pulse stability, but, on the other side, a slow drift, significant over many minutes (about $\pi$ radians in 40 minutes). A long-term drift is something rather typical of this kind of setups. The two OPAs can be seen as the two arms of an interferometer (the interference occurring in the DFG crystal). A slightly different thermalization of the optical components in one arm with respect to the other, causes a slow change of the $c_1 - c_2$ term in Eq. 2.4, and hence the long-term drift. It is possible to eliminate the drift measuring the CEP and, with a feedback, balancing the optical path in the two arms, moving a wedge plate (Fig. 2.9) placed in one of the arms.

In this section, we introduced the carrier-envelope phase of an ultrashort laser pulse. We presented briefly some methods to stabilize the CEP.
In particular, the twin-OPAs+DFG is a all-optical passive stabilization scheme, which can use pulses at 800 nm to generate phase-stable pulses in the mid-infrared. In the next chapter we will deal with the experimental construction of that scheme. In chapter 4 we will show some data showing the stability between the carrier-phase and the pulse-envelope of our mid-infrared pulses, taken with an electro-optic sampling technique.

# Chapter 3

# The experimental setup built for mid-IR pump-ultrashort optical probe spectroscopy

Let us now focus on the construction of our experimental setup. After a short section about the laser system used in our experiments, in the first part of this chapter (section 3.2) we will deal with the setup built to generate mid-IR CEP-stable pulses, which will serve as *pump* in the pump-probe experiments. The precise characterization of the mid-IR pulses is left to chapter 4; here we will show the optical schemes and the characterization of the light generated in the WLG and OPA stages.
The generation of the ultrashort optical pulses which we will use to probe our samples is the topic of section 3.3. Since our aim is to be sensitive to the phase of the mid-IR electric field, we should use a probe whose temporal duration is significantly shorter than a period of the pump field. For $\lambda_{\text{pump}} \simeq 13.5\,\mu\text{m}$, the period of the electric field is $T_{\text{pump}} \simeq 45\,\text{fs}$, and so the temporal width of the probe envelope pulse has to be approximately 25 fs or less.

## 3.1 The laser system

The laser system of our laboratory makes use of Titanium:Sapphire technology. Its scheme is depicted in Fig. 3.1. Here we give only a brief description of its components.

It is based on a Ti:$Al_2O_3$ laser oscillator (Coherent Mira), pumped by 5 W of a continuous wave green (532 nm) solid state laser (Nd:$YVO_4$, Coherent Verdi). The ultrashort pulses are abtained by means of Kerr-lens mode-locking. Their central wavelength is around 800 nm at a repetition rate in the radiofrequency, 76 MHz, with a bandwidth between 40 and 50 nm (the spectrum is Gaussian) and a temporal width of 20 fs.
The pulses generated in the oscillator enter in a regenerative laser amplifier (Coherent Legend), which uses again Ti:$Al_2O_3$ as active medium, and it is pumped by an other continuous wave laser (Nd:YLF, Coherent Evolution, see Fig. 3.1), with a power approximately equal to 20 W. The amplification stage in Legend is done thanks to a chirped pulse amplification scheme. The outcoming pulses maintain the

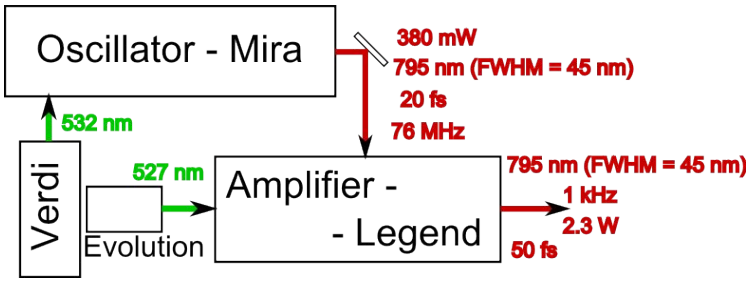


Figure 3.1: Laser system with typical values of wavelength, temporal width, power and repetition rate, as used for our experiments. Explanation in the text.

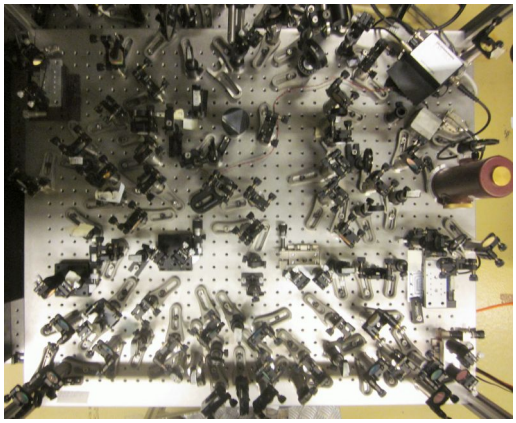

Figure 3.2: Top view of the twin-OPAs+DFG setup.

same photon energy and bandwidth they had after Mira, but increase hugely their energy per pulse, reaching approximately 2.2 mJ. On the other side, their repetition rate is lowered down to 1 kHz, and the temporal width is between 50 and 60 fs. It means that the pulses are almost transform-limited, i.e. the product of energy bandwidth and temporal width is $\hbar$.
The polarization lies in the horizontal plane, the plane parallel to the optical board.

These pulses are not carrier-envelope phase stable, as explained in chapter 2.

## 3.2 Twin OPAs + DFG scheme

In Fig. 3.2 a top view of the setup built in this thesis work is shown. As anticipated in section 2, we have a white-light generation stage which generates the seed for the twin OPAs. The two OPAs are symmetric and each one has two stages. They generates two signals, whose difference is the DFG. A detailed optomechanical scheme is depicted in Fig. 3.4.
We will constantly make reference to that scheme throughout this section, with no

Figure 3.3: Side view of the twin-OPAs+DFG setup.

need to cite every time that we are referring to it.

After the laser amplifier producing the pulses at 800 nm, the light beam is split by a 20:80 beam splitter (BS): about 0.45 mJ per pulse go to generate the probe, and about 1.73 mJ per pulse to the optical board of the twin-OPAs+DFG setup[1]. These pulses has to travel between some mirrors in back-reflection —which have the only purpose to make the optical paths of pump and probe of the same length— and are then further collimated thanks to a reflective Galilean telescope. The beam is collimated to a spot with a diameter of about 10 mm (FWHM), and its spatial transverse mode is gaussian $TEM_{00}$.

### 3.2.1 White-light generation

Only a fraction of the pump beam is taken to drive the WLG process, thanks to a glass BS1, which for p-polarized light and an angle of incidence of 45° reflects 1.4% of the incident light, namely about 24 µJ per pulse, well in excess to the amount needed for WLG. A slightly misaligned pinhole is used to regulate the photon flux, and a 10 cm-focal length lens focuses the beam in the WLG crystal (see the WLG stage in Fig. 3.4). We always worked in the single filament regime. A more complex filamentation arises when we increase the input power above a critical threshold.
The outcoming beam is strongly divergent and does not conserve the divergence of the driving beam; for this reason, the crystal is placed just in the focus of a Newtonian-like refractive telescope composed by the focusing lens L0.1 with a focal $f = 10$ cm and a second lens L0.2 with focal $f' = 5$ cm. Both sapphire and YAG can serve as Kerr media for WLG with a significant intensity in the near-IR region.

Bradler and coworkers [4] observed (Fig. 3.5) that the infrared part of the power spectrum is enhanced in YAG with respect to sapphire. According to their observation for YAG, a crystal lenght of 4 mm maximizes the IR gain, and a quite long focal length (∼10 cm) allows to work with higher fluences avoiding a complex filamentation.
It is of paramount importance to have a stable white light, because every instability in this stage will be amplified in the OPAs. We fine-tuned the aperture of the pinhole, the distance lens-crystal and the temporal compression of the laser amplifier in order to generate the more stable white light possible, monitoring the stability both to the naked eye and with a near-infrared spectrometer[2] for the infrared tail. A reddish circular ring outside a white circular spot (Fig. 3.6) guarantees the presence of a considerable amount of infrared photons [4].

A 50:50 beam splitter (BS5) divides the white light. Each beam goes to seed an OPA. In the first amplification stage, temporal superposition of the pump pulses with the seed is achieved moving a delay line in the path of the pump. Due to the large linear chirp of the white light, described in section 1.3, different fraction of the seed spectrum are amplified for different positions of the delay line. Selecting a desired fraction of the white light spectrum is just a matter of finding the corresponding position of the pump's delay line.

In Fig. 3.7 we can appreciate the chirp of a white light pulse produced in a sapphire

[1] The energy per pulse are calculated as the mean beam power divided by the repetition rate, 1kHz. The mean power is measured by means of a power meter, which is basically a pyroelectric sensor. Focalization is not required, thanks to the large sensible area of the detector. The response of the power meter is calibrated to be corrected for the tiny wavelength dependence.

[2] Hamamatsu NIR spectrometer. Its range of sensitivity is between 1.1 and 1.7 µm.

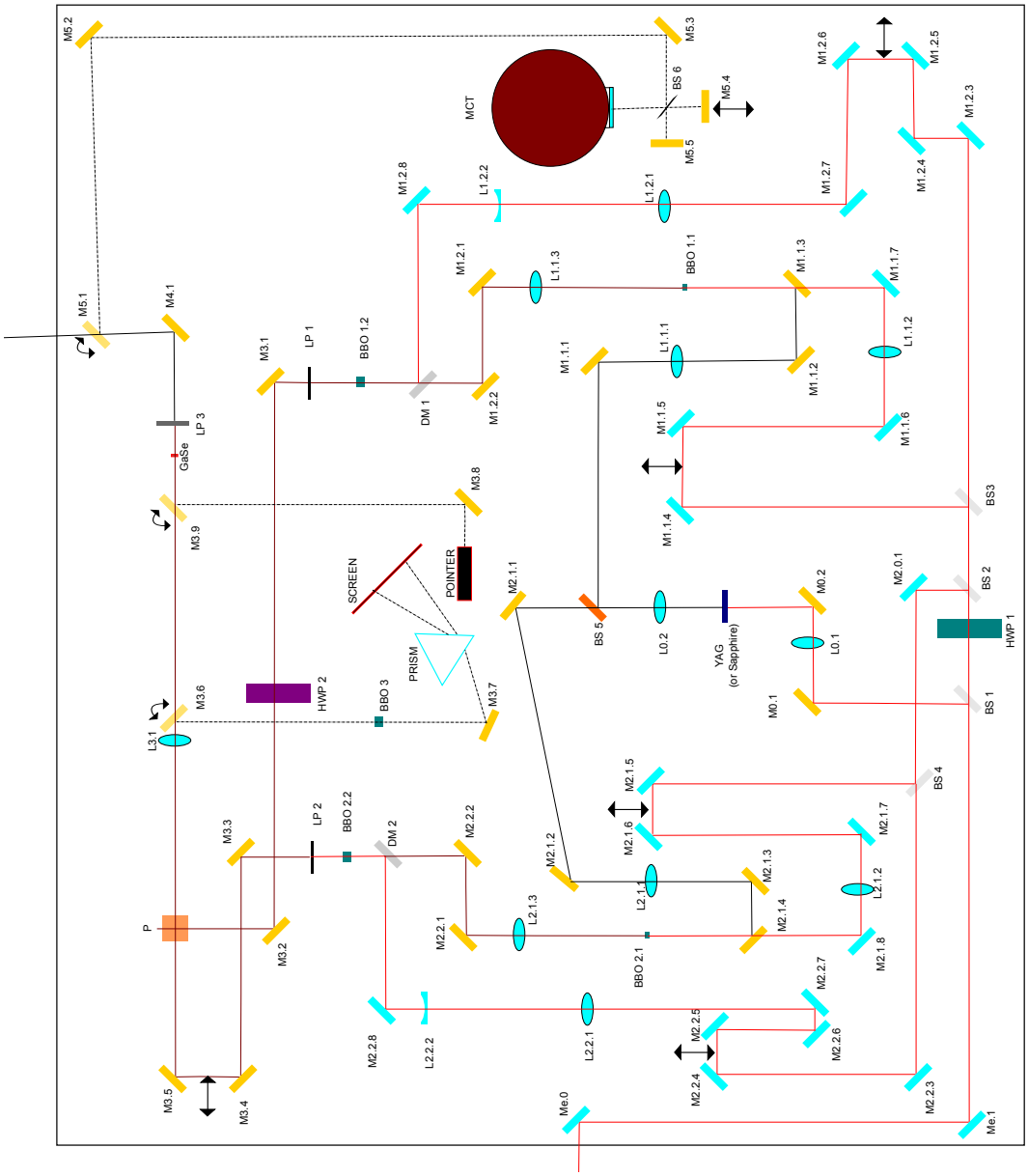


Figure 3.4: Complete optomechanical scheme of the twin-OPAs+DFG setup. Light blue mirror M: dielectric mirror, used on the pump path; BS: beam splitter; HWP: half-wave plate; yellow mirror M: Gold mirror, used on the seed, OPA and DFG paths; L: lens, cocave or convex depending on the shape; YAG (or Sapphire): Yttrium Aluminium Garnet or Sapphire crystal ; BBO: Beta Barium Borate crystal; DM: dichroic mirror; LP: low-pass filter; P: cube polarizer; GaSe: Gallium Selenide crystal; MCT: Mercury Cadmium Telluride fotoconductive infrared detector; Pointer: He:Ne laser pointer. Curved double arrows stand for flip mirrors, straight double arrows indicate a mechanical translator, controlled either manually or via an electronic controller. The numeration of the optical components is the following: e.n for external components, 0.n for the white-light generation stage, 1.1.n and 1.2.n, respectively, for the first and second stages of the optical parametric amplifier-1 (OPA1), 2.1.n and 2.2.n the same for OPA2., 3.n for the difference frequency generation stage and its diagnostics lines (BBO3+prism, alignment pointer-DFG, Michelson interferometer). BSs and HWPs follows a different, progressive, numeration. For a detailed description of the setup, see the text.

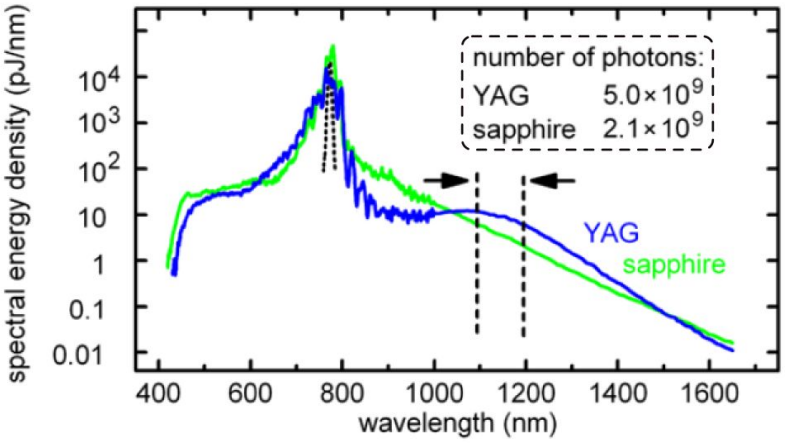


Figure 3.5: Spectral energy density (in logarithmic scale) for white-light continua generated in sapphire (green line) and YAG (blue line) crystals. The (not to scale) dotted black line peaked at 775 nm is relative to the pulses that drives the WLG. In the region from 1050 to 1450 nm, with respect to sapphire, the YAG allows for a remarkable increase in the generated photons. In the dotted box, the number of photons in the $[1.1 - 1.2]$ µm spectral range is indicated for the two Kerr media. Adapted from [4]

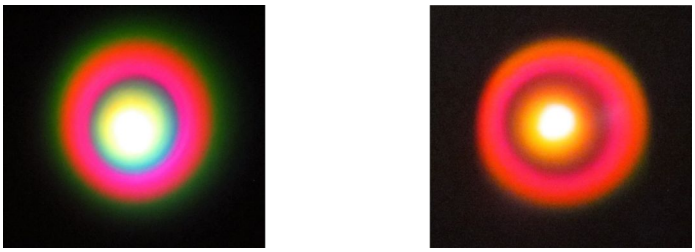

Figure 3.6: White light spots generated in the YAG crystal. We can observe a good $TEM_{00}$ mode, absence of complex filamentation and the external reddish halo. The spot on the right has different colours because its picture was taken after the transmission of the beam through the beam splitter which is not a 50:50 R:T ratio in the visible, although it is 50:50 in the near-infrared.

crystal, in a scheme identical to the one we built [21].

### 3.2.2 The two-stages OPAs

After the BS for WLG, a half-wave plate (HWP1) rotates by $\pi/2$ the polarization of the pump, making it vertical. The rotation is a compulsory step to fulfill the phase matching conditions in type-II OPAs. The pump is then split by a 50:50 BS2 (for OPA1 and OPA2) and each beam is subsequently split with a 8:92 ratio, to pump the first (8%) and the second (92%) stage (BS3, BS4).
An OPA with two stages rather than only one has two main advantages. It allows to create in the first stage a seed with a "clean" spectral content, and then to amplify it in the second stage. The two stages are optimized separately, and this makes the total gain larger than that of a single crystal with the same total length. Notably, the group velocity mismatch accumulated in the first crystal does not influence the temporal superposition of seed and pump in the second stage, because the second stage pump's optical path is adjusted by a separate delay line before the entrance

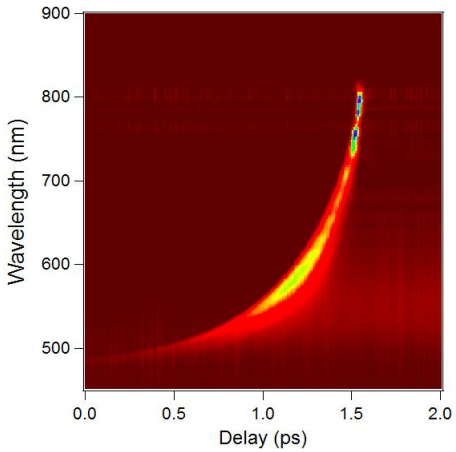


Figure 3.7: Two photons absorption in a ZnSe crystal (colour scale), which follows the chirp-wavelength profile of the white-light continuum. ZnSe has an energy gap of $E_g = 2.7\,\text{eV}$ at room temperature, corresponding to a wavelength of 460 nm. Ultrashort pulses at 800 nm act as optical gates for the two photon absorption process $\hbar\nu_{\text{gate}} + \hbar\nu_{\text{WLG}} > E_g$. The transmitted white light is wavelength dispersed and measured by means of an array of photodiodes, and the relative change in transmission —caused by two photon absorption— is plotted. Delaying the ultrashort gate pulses allows to appreciate the temporal dispersion of the spectral content in the white light cuntinuum pulses, i.e. their chirp. The chirp is almost linear. The infrared tail is absent because out of range of the detector, and the bending of the curve for shorter wavelengths (present similarly if the image is plotted versus frequencies instead that wavelengths) should not be ascribed to a chirp nonlinearity, but to the high $\mathrm{d}n/\mathrm{d}\lambda$ term of ZnSe in that region, approaching $E_g$. The gate pulse slips over the white light pulse and causes two photon absorption with larger wavelengths than expected. Adapted from [21]

of the second crystal.
Only type-II phase matching was used, because of the advantages already discussed in section 1.2.3.

### The first stages: NOPA

The first stage has a noncollinear interaction geometry (NOPA). The angle between seed and pump is approximately 3° in the vertical plane. Noncollinearity allows to easily separate idler and signal after the crystal, because they have different directions, due to the conservation of wavevectors (phase matching). A simple stopper placed a few centimeters after the BBO blocks idler and remaining pump beams, which are going down, while the signal passes, together with the white-light.
Two lenses (L$i$.1.1 and L$i$.1.2, $i = 1, 2$) with focal lengths of 20 cm focalize seed and pump about three millimeters before the BBO crystal. The spot sizes of the two beams are the same, and the spatial overlap is achieved at the entrance of the BBO. Since the angle of noncollinearity is smaller and the focuses are quite long, the beams can be considered spatially superposed throughout the length of the crystal. The lengths of the first-stage's BBOs create the only asymmetry present in the twin OPAs. In effect the two OPAs have to work at different central wavelength to be used efficiently for the DFG process. Typical values are 1.3 µm and 1.5 µm for

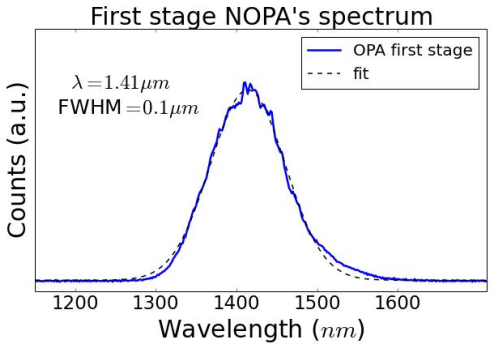


Figure 3.8: Typical spectrum of the signal generated in one of the two NOPAs. Central wavelength and bandwidth are written on the left of the peak.

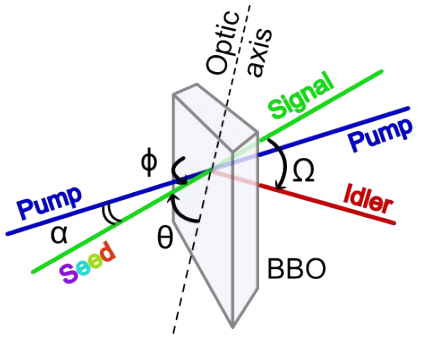


Figure 3.9: Geometry of the three waves interaction in the first stage OPAs.

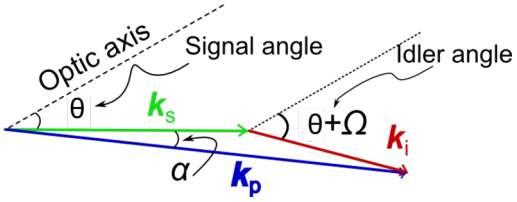


Figure 3.10: Geometry of the phase matching for the first stage OPAs.

OPA1 and OPA2 respectively[3]. But as can be seen in Fig. 3.5, the spectral density is exponentially decaying in the infrared, and the larger the wavelength, the less the seed intensity. To partially balance this asymmetry, the BBO of the more infrared OPA (BBO1.1) was chosen to be 3 mm long, to maximize the gain; the length of the BBO of the other OPA (BBO2.1) was instead 2 mm.

First stages' signal intensities range from approximately 3.5 µJ per pulse at 1.25 µm, down to 1.5 µJ at 1.55 µm, close to signal-idler degeneracy (at 1.6 µm). As in every noncollinear OPA, spectra are typically large, like in Fig. 3.8. Nevertheless, we adjusted parameters to make it as narrow as possible, and reached spectral widths below 100 nm.

The efficiency of the process can be expressed by the ratio (Intensity of signal plus idler)/(Intensity of pump plus seed), or by the photon conversion ratio (Number of signal photons)/(Number of pump photons). It is common to talk simply about *efficiency* ($\eta$) when referring to the first definition, while in the second case the name *quantum efficiency* ($\eta_Q$) has to be preferred. If the intensity of the seed can be neglected with respect to the intensity of the pump (like in our case), $\eta = (I_s + I_i)/I_p = (N_s\omega_s + N_i\omega_i)/(N_p\omega_p) = (N_s/N_p)\times(\omega_p + \omega_i)/\omega_p = N_s/N_p$, exactly the quantum efficiency $\eta_Q$[4]. In the most favorable configuration (OPA at ∼1.3 µm), the signal pulses have energies up to 3 µJ, corresponding to an efficiency of about

[3]From here on, we will always call OPA1 the OPA generating a signal with larger wavelength.
[4]This result is a mere consequence of the conservation laws of the parametric interaction.

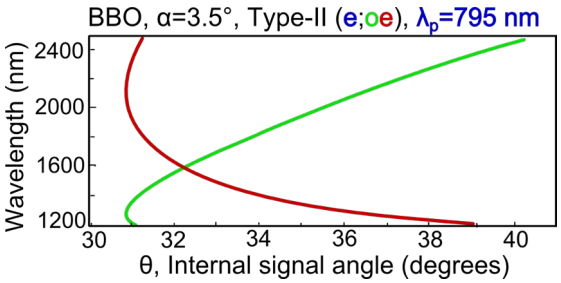


Figure 3.11: Calculated (with SNLO) room temperature phase matching conditions for a BBO-based NOPA pumped at $\lambda_p$, with pump-signal angle of noncollinearity $\alpha$, and for type-II phase matching. Green line: signal, ordinary polarized; red line: idler, extraordinary polarized.

10%.

We can schematize the geometry of our interaction as in Fig. 3.9 and 3.10[5]. In the setup, both the azimuthal angle $\theta$ and the polar angle $\phi$ can be varied. With the program SNLO [1], we calculate the angles between signal and optic axis in order to achieve phase matching. In Fig. 3.11 we see how to tune the angle $\phi$ of the crystal once we choose a desired signal wavelength, for our type-II NOPA in a BBO. Basing on these numerical calculations, our first stage's BBOs were cut at 31° for both OPAs.

Finally, we note that the described interaction is not the unique nonlinear process happening in the BBO crystals. It is doubtlessly the principal nonlinear process, but together with the invisible spot of the signal, several new visible and colourful spots come into view, spatially dispersed because of the noncollinear interaction geometry.

### The second stages: collinear OPAs

The choice of a collinear interaction geometry was necessary in order to achieve the maximum gain, using 6 mm-long crystals.

Similar to the case of WLG, also the BBO of the first stages is placed within two lenses (with focal lengths of 20 and 12.5 cm respectively), even if not exactly in the focus. The position of the second lens is chosen with the aim to match the spot sizes of pump and seed in the second stage BBO. In effect, the pump in the second stage is very intense (800 mJ per pulse), and does not need to be focalized in order to produce nonlinear effects. Moreover, a focalized pump would go beyond the damage threshold, causing permanent damage to the crystal. For this reason, the pump is collimated in a Galilean telescope (L1.2.1-L1.2.2, e.g. for OPA1) to a spot size of about 3 mm, and it enters in the BBO after being reflected by a suitable dichroic mirror. Such a dichroic mirror allows us to have a collinear interaction geometry, because the seed (the signal of the first stage) is transmitted, while the pump experiences reflection.

In Fig. 3.12 we report the analogous calculation of Fig. 3.11, but carried out for a collinear parametric amplification. Targetting for OPA1 at 1.5 µm and OPA2 at 1.3 µm, the crystals are cut at 27° and 26° respectively.

The efficiency for the second stages is higher, since the sum of signal and idler intensity is larger than 200 mJ, for a single OPA, corrisponding to an efficiency exceeding

[5]The angle $\psi$ introduced in paragraph 1.1.4, is here the sum $\theta + \alpha$.

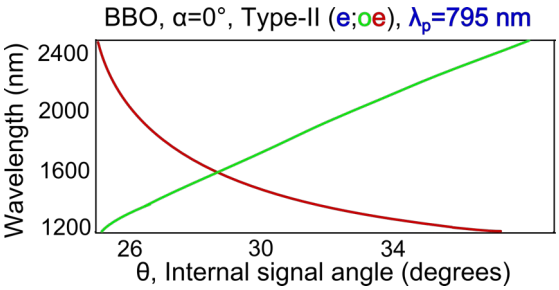


Figure 3.12: Calculated (with SNLO) room temperature phase matching conditions for a BBO-based NOPA pumped at $\lambda_p$, in a collinear geometry interaction, and for type-II phase matching. Green line: signal, ordinary polarized; red line: idler, extraordinary polarized.

25%. Like for the first stage, when working close to signal-idler degeneration the generated intensity decreases, but here smoothly. At 1.3 µm we reach values up to 250 mJ of signal plus idler, but at 1.5 µm we can still have around 200 mJ.
In absence of the seed, a small fraction of light is still downconverted to signal and idler (spontaneous OPA), which we found useful to employ in the procedure to align the pump and the seed of the second stage of the OPAs. Despite the presence of this light with a pulse-to-pulse randomly generated CEP, the CEP of the signal is the one of the seed, when the OPA is seeded. We can be confident about it because the intensity of the spontaneous OPA is around 1 µJ per pulse, a tiny fraction of the total signal, which will be even smaller, almost zero, in presence of the seed.

### 3.2.3 DFG

The collinearity of the second stages requires new methods to isolate the signal beam from pump and idler. For this reason, a low-pass filter (LP1, for OPA1) blocks the pump and leaves signal and idler going through it. As can be seen in the top of Fig. 3.4, the half-wavelength plate HWP2 rotates by $\pi/2$ the polarizations of signal and idler of OPA1. The signal-idler splitting and the recombination of the two signals are achieved in the same optical element: a cube polarizer (P). The signal from OPA1 is reflected because of its *s*-polarization, while the signal from OPA2, which is *p*-polarized, is trasmitted. Conversely for the idlers.
At the output we have thus the two signal beams spatially superposed at one side of the cube polarizer, and the same for the idlers at the adjacent side. For the purposes of this thesis, we are not interested in the idlers, and therefore we dump them in the absorber, and just focalize the signals directly on the DFG crystal (a 0.5 mm GaSe crystal), using a lens (L3.1) with a long focal (30 cm). In addition to the long focal length, the crystal was always kept slightly out of the focus, in order to avoid a possible damage of the crystal.
We should mention that the cube works very well as a polarizer for the reflected beam, but not so well for the transmitted beam. Thus a little part of the idler of OPA2 is still present together with the two signals impinging on the GaSe crystal.

We built a "sum frequency generation line" to look for the temporal overlap of the pulses of the two signals. A flip mirror (M3.6) separates it from the main line of the DFG. The signals impinge on a thin BBO crystal (BBO3), cut for second harmonic generation, and generate their second harmonics, usually orange for OPA2 and in the extreme red for OPA1. Moreover, also the third harmonic of OPA1 is visible,

with an azure spot. The chromatic dispersion of a prism made of glass separate the spots. Scanning the translator of the delay line of OPA2 (M3.4-M3.5, placed before the cube polarizer), we observe the temporal coincidence of the pulses when a new spot appears in the middle of the two second harmonics. This spot is the sum frequency of the two signals.
The described method allows us to achive the temporal coincidence (the so called "time zero") in an easy way. Working directly with the DFG would be more difficult and time-consuming, because the mid-infrared radiation cannot be seen neither with bare eyes, nor with infrared cards. Furthermore, the emitted DFG beam has a low intensity, especially when not carefully optimized over every parameter, and hence it is a useful aid to look for infrared light optimizing the angles of the crystal, but knowing to have already temporal coincidence.
To look for DFG radiadion, we used the power meter placed after a Germanium plate (LP3), acting as a low-pass filter. The band gap of Germanium is 0.67 eV, corresponding to 2.085 µm. Therefore the signals of the OPAs are completely absorbed, while the DFG, which is well below gap, passes, although not completely, because it is partially reflected at the interfaces. We estimated the transmission using a slightly noncollinear interaction geometry, thanks to which we could separate geometrically the DFG from the other beams. It turns out that the Germanium lowers the intensity to about 60% of the total DFG (i.e. it blocks $\sim 40\%$ of the DFG radiation).
Working with the OPA1 signal wavelength larger than 1300 nm avoids that the residual OPA1 idler passes through the Germanium window.

The characterization of the DFG pulses is the topic of chapter 4. Here we only anticipate that varying the wavelength of the OPAs, the relative path difference between the signals and the angles of the GaSe crystal, it is possible to generate light from 4 up to nearly 20 µm. The achievable energy per pulse strongly depends on the DFG wavelength, being of a few hundreds nJ for the largest wavelengths and many µJ for the smallest.

## 3.3 Generation of $< 20$ fs pulses

In the introduction to the present chapter, we pointed out that we need very short probe pulses in order to be sensitive to the phase of the electric field within the envelope of the pump pulse. A rough estimate for its FWHM, $\Delta t_{\text{probe}}$, is $\Delta t_{\text{probe}} \lesssim T_{\text{pump}}$, where $T_{\text{pump}}$ is the period of the pumping electric field, and both quantities are evaluated in the material, hence taking into account the contribution of the refractive indexes. Actually $n(\text{probe}) > n(\text{pump})$ in our case, because we use an *optical* probe, at $\lambda_{\text{probe}} = 800$ nm, and so we will use the vacuum wavelengths, knowing that the estimate will result to be a little conservative. For wavelengths between 8 and 18 µm, $T_{\text{pump}}$ ranges between 27 and 60 fs. The temporal width of our probe should therefore be approximately less than 25 fs, to cover our full range of interest.
After the laser amplification stage, the 800 nm-pulses are almost transform-limited and has a temporal width of approximately 60 fs, being not suitable to be used directly as probe pulses. We therefore broaden their spectrum by means of a nonlinear technique consisting in the focalization of the beam in a hollow fiber filled by a noble gas, in our case Argon. We then correct the accumulated chirp in a set of suitable designed chirped mirrors. We will examine it in depth in the next paragraph, dealing

here with the techinques used to measure the temporal width of laser pulses.

Femtosecond pulses are too short for their temporal shape to be measured directly by electronics. Once again, nonlinear optics comes to our aid, and allows to measure the field autocorrelation, from which the temporal width can be inferred.
The (normalized) correlation function between the fields $E_1$ and $E_2$ is

$$\gamma_{12}(\tau) = \gamma_{21}(\tau) = \frac{< E_1(t) E_2^*(t+\tau) >}{\sqrt{< E_1(t) E_1^*(t) >< E_2(t) E_2^*(t) >}}, \tag{3.1}$$

where the sign $< \cdot >$ stands for the integration in $t$ over a region large with respect to the two pulses temporal extent. The denominator of equation 3.1 is nothing but the square root of the product of the intensities, $(I_1 I_2)^{1/2}$. $\gamma_{12}(\tau)$ determines the interference term in the intensity of the field sum of $E_1$ and $E_2$.

$$I_{12}(\tau) = < E_1(t) + E_2(t+\tau) >^2 = I_1 + I_2 + 2\sqrt{I_1 I_2}\mathrm{Re}(\gamma_{12}(\tau)) \tag{3.2}$$

If $|\gamma_{12}| = 1$, the two fields are perfectly coherent, and there will be an interference pattern which depends on the ($\tau$-dependent) phase between the fields. If $0 < |\gamma_{12}| < 1$, we have partial coherence between $E_1$ and $E_2$, while for $|\gamma_{12}| = 0$, the fields are said to be completely incoherent, and the intensity of the sum is just the sum of the intensities.
When $E_1 = E_2 \equiv E/2$, we talk about **autocorrelation**, and

$$\gamma(\tau) = \frac{< E(t) E^*(t+\tau) >}{I} = \frac{1}{I} \int_{-\infty}^{\infty} E(t) E^*(t+\tau) \mathrm{d}t \tag{3.3}$$

is the autocorrelation function. It follows that $\gamma(\tau = 0) = 1$, for every kind of radiation. Moreover, continuous-wave laser fields have an almost infinite coherence length, and so $|\gamma(\tau)|$ will be unitary for almost every $\tau$. For pulsed laser, it can be used to measure the temporal width of the pulses, if they are transform-limited. Transform-limited pulses with a Gaussian envelope and intensity FWHM= $\Delta t$ gives rise to a Gaussian autocorrelation function, with FWHM= $2\Delta t$, as can be seen in Fig. 3.13.
The Fourier transform $\gamma(\omega)$ gives the power spectrum of the electric field $E(t)$, i.e. $\gamma(\omega) = \mathcal{F}_\omega[\gamma(t)] \propto |E(\omega)|^2$. We can perform this kind of measure splitting a beam in two, delaying one of the split beams by a time $\tau$, and then recombinig them on the surface of a photodiode. It is basically the scheme of a Michelson interferometer.

The precedent considerations about linear autocorrelation versus time duration of the pulses hold as long as the pulses are transform-limited.
If they are not, this kind of autocorrelation still gives the correct power spectrum, once Fourier transformed, but continue to give the temporal width in its tranform-limit case, which actually is no longer the case. However, the information given by the time axis in a linear autocorrelation is often useful, because it sets a lower limit to the temporal duration of the pulses. We can intuitively understand why for chirped pulses it underestimates the correct pulse duration with the following argument. Two identical chirped pulses separated in time by a delay $\tau$ (Fig. 3.14) are placed with the back of the delayed pulse (red electric field) temporally superposed to the front of the non-delayed pulse (blue electric field). Because of the chirp, the frequencies of the two pulses in that region of temporal superposition are not equal,

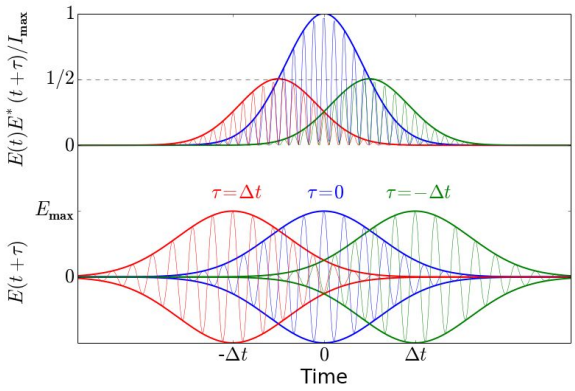


Figure 3.13: In the bottom part, the same transform-limited pulse $E(t+\tau)$ is represented in red, blue and green for three delays $\tau = -\Delta t$, 0 and $\Delta t$ respectively, with $\Delta t$ indicating the FWHM of the pulse intensity. In the top part, the products $|E(t)E^*(t+\tau)|$ are also shown, normalized to unity. Their temporal width is constant for any $\tau$. Therefore, the height of the peak is directly proportional to the integral over $t$ of $E(t)E^*(t+\tau)$, and hence to $\gamma(\tau)$. We can then conclude that $\gamma(\tau)$ is just 1/2, for $\tau = \pm\Delta t$, i.e. the full width at half maximum of the autocorrelation function is twice the one of the original pulses.

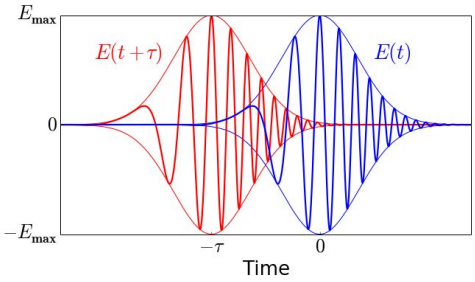


Figure 3.14: Partially superposed chirped pulses. The chirp is exaggerated unrealistically for sake of clarity.

and therefore the interference term will be little with respect to the interference term if the pulses were unchirped.
In chapter 4 we will describe and use it to analyse the spectral content of the mid-IR pulses.

The correlation $\gamma_{12}(\tau)$ is a *linear* correlation, because it involves fields. We can also define a nonlinear correlation $\Lambda_{12}(\tau)$, which is *quadratic* in the fields, and therefore involves their intensities. We will call it "intensity correlation". Again, we are interested in the autocorrelation case

$$\Lambda(\tau) = \frac{1}{<I(t)>^2} \int_{-\infty}^{\infty} I(t)I(t+\tau)\mathrm{d}t \tag{3.4}$$

The delay $\tau$ can be controlled by means of a mechanical translator, the integration over $t$ is performed by a photodiode, and to have the product $I(t)I(t+\tau)$ we can exploit the nonlinear effect of frequency doubling (second harmonic generation, SHG), already mentioned in section 1.1. We here only recall that in a SHG process the two fields at the same frequency couple in a second-order nonlinear crystal, and the field amplitude of the emitted second harmonic is directly proportional to the product of

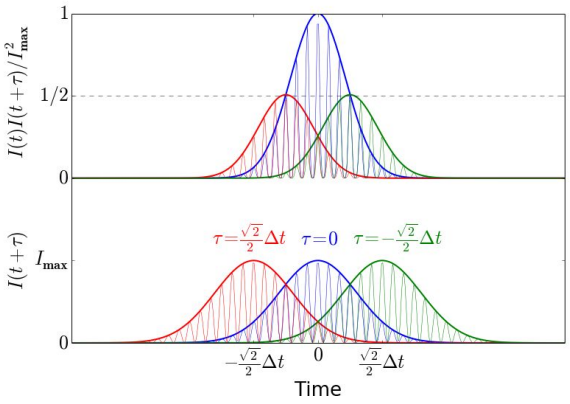


Figure 3.15: Analogous to Fig. 3.13, but for the intensity autocorrelation. In the bottom, the intensity of three pulses with different delays. In the top, their products with the non-delayed pulse intensity. Since for any $\tau$ the latter quantities mantain the same linewidth, their peak intensity is directly proportional to the integrated intensity. The FWHM of the intensity autocorrelation $\Lambda(\tau)$ turns out to be $\sqrt{2}\Delta t$.

the fields. Therefore, the intensity of the SHG pulses, which is the quantity measured by the photodiode, is proportional to the product of the intensities. This will enable us to perform intensity autocorrelation measurements, whose experimental implementation and results are left to paragraph 3.3.2.
The FWHM of the SHG intensity peak as a function of the delay $\tau$ is $\sqrt{2}\Delta t$, where again $\Delta t$ is the FWHM of the intensity of the pulses, as explained in Fig. 3.15.
What said about intensity autocorrelation and temporal width measurement is not limited to transform-limited pulses, unlike what said about linear autocorrelation. The process of frequency doubling is nothing but a sum frequency generation. With reference to Fig. 3.14, when the temporally superposed frequencies are slightly shifted about the central frequency (one to the left and the other to the right), the sum frequency generation process creates photons with twice the central frequency of the incoming pulses. The probability of the sum frequency to happen is the same of the second harmonic generation when the pulses are exactly in temporal coincidence, since the chirp cannot be large enough to change the constant factors that determine the "strength" of the process, namely the second-order nonlinear susceptibility.
Therefore, also for chirped pulses, a SHG measurement like the one showed in Fig. 3.22 is an intensity autocorrelation measurement, and gives the correct estimate of the duration of the involved pulses.

### 3.3.1 Spectral broadening and compression

The necessary stages to obtain temporally compressed pulses can be divided in spectral broadening and following chirp correction, which often takes the name of "compression", because it really compresses the pulse duration, almost down to its transform-limit.
We already talked about two phenomena which causes **spectral broadening** or generate pulses with a large bandwidth: the downconversion in a noncollinear interaction geometry and the self-phase generation, in section 1.2.3 and 1.3 respectively.

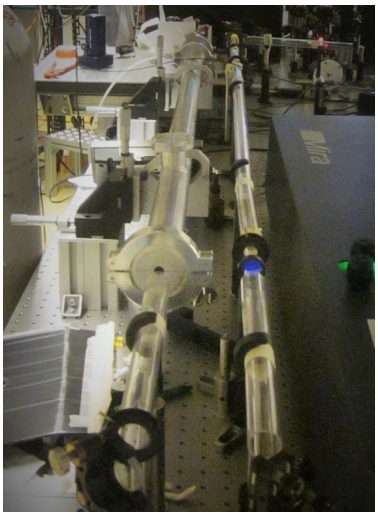

Figure 3.16: Picture of the system to compress the 800 nm pulses. The plexiglass tubes, visible in the right part of the figure, serve to protect the beam from air movements, which would introduce additional noise.

In the first case (the noncollinear optical parametric amplification, NOPA), the output is centered in the region between 1.3 and 1.5 µm, considering a pump pulse at 800 nm. After a suitable compression stage, pulses with a few optical cycles can be obtained, in the sub-10 fs regime [5]. The reason which allows the NOPA broadband generation is the presence of a variable idler output angle, i.e. the addition of a degree of freedom in the phase matching equation, which can thus be verified over a broad spectral band.
The second case in that of self-phase modulation, which broadens the spectrum around the central wavelength of the driving pulse. It is the main process occurring in white-light generation, and gives rise to pulses with a linear chirp, which is a valuable property for the engeneering of the wavelength-dependent delay lines used in the compression stage.
The most common implementation does not involve sapphire or yttrium aluminium garnet crystals —which do not work with high intensity pulses— but noble gases. A box filled by a noble gas is an optical Kerr medium, even thought with a quite small third-order nonlinear electric susceptibility, at least at atmospheric pressure. To overcome this issue, small diameter hollow fibers are employed. In effect, if we focalize the beam at the aperture of the hollow waveguide, it propagates with the same focus size until the waveguide ends, thus allowing the nonlinear process throughout the length of the fiber. Two-photon absorption sets the limit to the shortness of the wavelength that can be employed, but noble gases have very high ionization thresholds, and thus it does not constitute a problem for us. Moreover, in noble gases, to smaller ionization energies correspond higher third-order nonlinear coefficients. For this reason, in the heaviest gases it is easier to achieve the broadening.
Actually, we used KALEIDOSCOPE™[6] (Fig. 3.16), which consists of a quartz hollow fiber, 1 m-long, with an internal diameter of 250 µm, and placed on a V-groove mount in a cylindrical chamber filled by Neon or Argon. The chamber is closed by two 5 mm-thick Brewster-angle windows for input and exit. Inlet and outlet valves

[6] A FEMTOLASERS™, product [18]

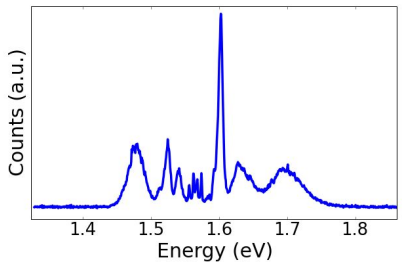


Figure 3.17: Typical spectrum of the probe pulses, as measured after the compressor.

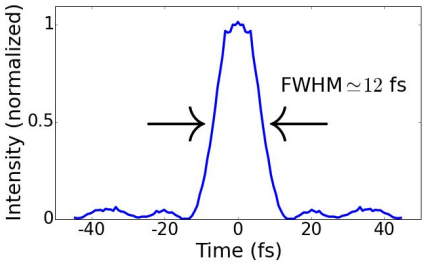


Figure 3.18: Fourier transform of the probe spectrum. We see that our pulses can suport $\sim$12 fs pulses.

regulate the pression of the gas inside the chamber, and the position of the hollow fiber is controlled in the $xy$ plane (being $z$ the propagation direction of the beam). In a pump-probe experiment the probe pulse intensity should be a tiny fraction of the pump intensity; for this reason it is wise to use as much intensity as we can to pump the twin OPAs, and address the minimum intensity to the probe generation. Unfortunatly, our hollow fiber system works well only for pulse energies larger than 400 µJ. We hence addressed 400 µJ per pulse to KALEIDOSCOPE™, and chose to use Argon because, having a higher third-order nonlinear coefficient, serves better in our low-pulse intensity regime. The beam is focalized in the hollow waveguide by means of a lens with a focal length of 1 m. The $xy$ position of the fiber and the pressure of the gas were adjusted to generate pulses with

- broadband spectrum;
- stability;
- $\mathrm{TEM}_{00}$ mode.

Even if the spot is more complex than that of a $\mathrm{TEM}_{00}$ mode, the important feature is the presence of a $\mathrm{TEM}_{00}$ region in the spot, which can then be selected using a pinhole. The final throughput of hollow fiber compressor is larger than 120 µJ per pulse, well exceeding what is needed for the probe, and therefore we select only a small fraction of it. Gas pressure ranging from 150 to 220 kPa, enables us to have large enough spectra. Another fundamental parameter is the compression of the pulses entering in the hollow fiber. The optimal pulse compression for spectral broadening in Argon resulted to be different from the optimal compression for the same process in YAG, used to generate the seed of the OPAs; not even a compensation of the amount of glass in the two paths seemed to be sufficient to completely equalize the optimal compression. A compromise was therefore necessary.

A typical probe spectrum, acquired with a spectrometer, is represented in Fig. 3.17. The process introduces a noise, which makes the broadband pulses significantly more noisy than those before the hollow fiber. The pulse-to-pulse mean intensity fluctuations can be estimated to be around 5-10%.

The apparatus does not change neither the electric polarization nor the carrier-envelope phase (CEP) of the pulses; the CEP of the probe pulses is irrelevant for our experiments (see Fig. 3.19). Indeed the envelope of the probe pulses is shorter than the wavelenght of the CEP-stable mid-infrared pulses, but significantly longer than

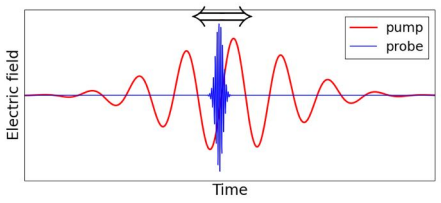


Figure 3.19: Representation of pump and probe pulses as they should be in our experiments.

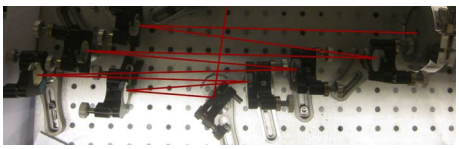

Figure 3.20: Picture of the set of chirped mirrors, used to correct the chirp of the probe pulses. The light (sketched in red) bounces between them in a back-reflection geometry.

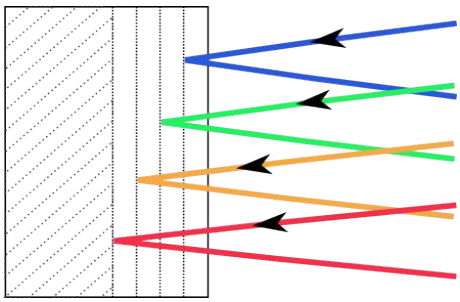

Figure 3.21: Conceptual representtion of the working mechanism of a chirped mirror.

the wavelenght of the probe itself and will not significantly influence our response.

The large linear chirp introduced by the self-phase modulation process is corrected in a specifically designed wavelength-dependent delay line. The elements making the optical length in the delay line dependent on the wavelength are the so-called "chirped mirrors". We used a set of six chirped mirrors (Fig. 3.20). The characteristic feature of this kind of dielectric mirrors is that different wavelengths have different penetration depths, as illustrated naïvely in Fig. 3.21. In addition, they have a very broadband reflectivity: only green and blue light are transmitted, but it does not constitute a problem, because blue and green light do not carry significant intensity in our pulses (Fig. 3.17).
In section 1.3 we showed that a self-phase modulated pulse is linearly chirped, with redder wavelengths shifted towards the front of the pulse and and bluer wavelengths towards the back. This is also the common chirp introduced by the pulse propagation in an ordinary dispersive medium. The layers of the employed dielectric mirrors were optimized to correct the chirp accumulated in our hollow fiber and in the Brewster-angled windows.

### 3.3.2 Pulse duration - autocorrelation

Fig. 3.18 represents the square modulus of the Fourier transform of the square root of the power spectrum, Fig. 3.17. This indicates that our pulses can in principle support a temporal width down to 12 fs. This width constitutes only a lower bound, not a measure of the pulse duration, which can be done with an intensity autocorrelator, as described in the introduction to this section. The optical scheme of the autocorrelator is sketched in Fig. 3.22. Thanks to the noncollinear geometry, the second harmonic originating from the temporal coincidence of the pulses in the two

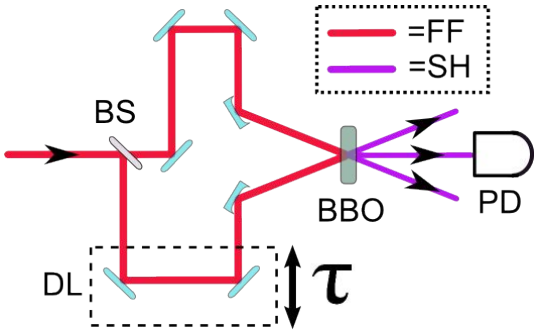


Figure 3.22: Optomechanical scheme of the intensity autocorrelator. BS: beam splitter; DL: delay line; PD: photodiode; FF: fundamental frequency; SH: second harmonic.

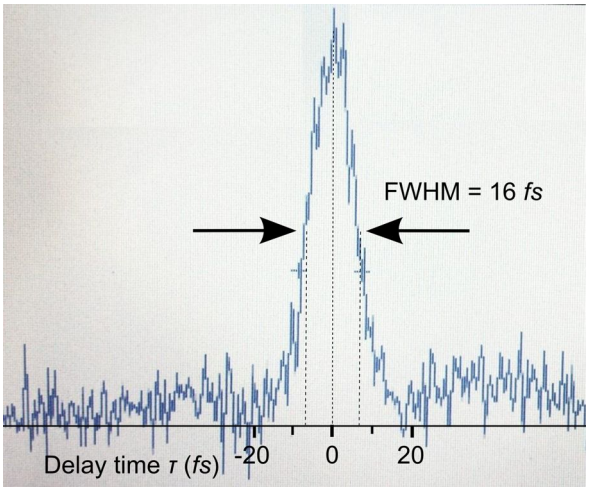


Figure 3.23: Example of an intensity autocorrelation trace (average of 16 scans), as measured with our autocorrelator. Here the FWHM of the trace is 15 fs, i.e. the temporal width should be 12 fs

arms does not mix with the second harmonics generated by the single pulses, and thus the measurement can be done on a free background. A similar autocorrelator could also allow a collinear geometry, placing a high-pass filter to block the fundamental frequency; nevertheless, in that case, the autocorrelation signal would stand over a high background of the delay-independent second harmonics. The mechanical translator of the delay line is controlled via an electronic circuit. For each position, a Silicon-based photodiode integrates, over a suitable temporal window around the trigger signal, the intensity of the second harmonic pulses produced in the thin BBO crystal. Fig. 3.23 shows a typical trace of second harmonic intensity $I_{\mathrm{SHG}}$ versus delay time $\tau$. Its temporal scale is not corrected by the factor $\sqrt{2}$ shown above, in the introduction to the present section.

The autocorrelation measurements are performed after the chirped mirrors. It is then important to preserve the ultrashortness of the probe pulses up to the sample. For this reason it is crucial to use optical elements which do not absorb or reflect part of the spectral bandwidth, and do not chirp the pulses. The latter issue limits ourselves to use only optical element in reflection, not in transmission, because the material disperion does introduce a chirp. To this end, no lenses could be employed, and therefore we chose to use a concave spherical mirror to focus the probe on the

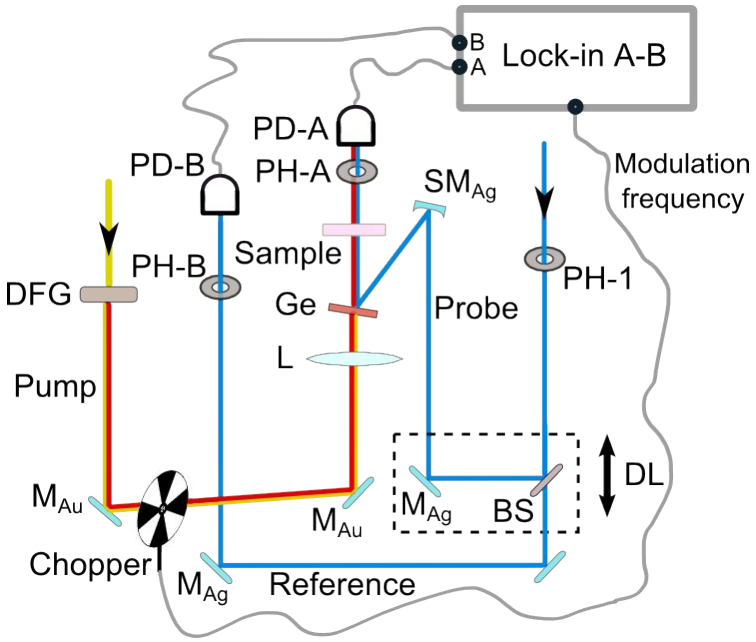


Figure 3.24: Setup for mid-infrared pump-optical probe spectroscopy experiments. The acquisition system is shown for measurements in transmission, but little changes allow to measure the reflectivity. Yellow lines indicates the signals of the twin OPAs, red lines the mid-IR pump, and blue lines the probe. Part of the probe is taken as a reference signal. Used acronyms: DFG difference frequency generation crystal (GaSe), $M_{Au}$ Gold plane mirror, L ZnSe lens, Ge Germanium window, PH pinhole, DL delay line, BS beam splitter, $M_{Ag}$ Silver plane mirror, $SM_{Ag}$ Silver spherical mirror, PD Silicon photodiode.

sample. The first mentioned issue, basically concerns the materials which the optical elements are made of. Better than Gold or Aluminum, Silver has a very high reflectivity over both visible and near-infrared range, and does not cut the tails of the broadband spectrum. We therefore adopt Silver mirrors to transport the probe pulses from the compressor to the sample.
Finally, the least optical element on the path of the probe is a coated Germanium window, which works both as a dichroic mirror, allowing the recombination of pump and probe in a collinear geometry, and as a low-pass filter, stopping the radiation coming from the OPAs. A reflectivity spectrum of the coated Germanium is not available. However, as we will demonstrate in the later chapters, it supports a sufficiently broad pulses to be used for our purposes.

## 3.4 The pump-probe setup

The optomechanical scheme of our pump-probe setup is drawn in Fig. 3.24, together with a schematization of a possible acquisition system, which is the topic of section 3.5. We already stressed the importance of the pinhole $PH_1$, of Silver mirrors $M_{Ag}$ and $SM_{Ag}$, and of the use of Germanium as a dichroic mirror. Probe pulses have an energy ($\sim$1.55 eV) well above gap, and are mainly absorbed. Apart from the absorption, a considerable quantity is reflected by the surface of the window, and this is the precisely the quantity that goes to *probe* the sample. Different pump-probe delays are obtained thanks to the movement of the mechanical translator DL on

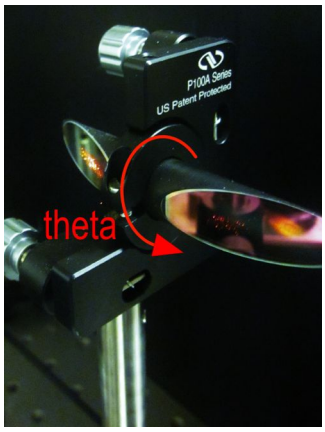


Figure 3.25: Polarizer with Brewster-angled windows. It is apt for broadband transmission.

the probe path. Its first mirror is actually a beam splitter (BS, in Fig. 3.24): it transmits part of the beam to be used as a reference probe signal. As described earlier, hollow fiber introduces intensity fluctuation of order of 10% making crucial the implementation of a refrerenced measurement in pump and probe configurations. This becomes crucial when pulse-by-pulse acquisitions are performed, typically with a balanced photodiode.
The polarization of the probe pulses is not totally lying in the horizontal plane but has also a vertical component, although smaller by about a factor 5. It is possible that part of the small polarization rotation occurs in the hollow fiber, despite it is delimited by two Brewster-angled windows, but, in addition to this, the reflection on the Silver mirrors do not perfectly conserve the polarization axis, and therefore introduces a vertical component.
If we want to perform experiments with a polarized probe, we should put a polarizer on the probe path. We opted for a Brewster polarizer, Fig. 3.25, not represented in Fig. 3.24. Rotating the angle $\Theta$ of the polarizer is possible to select any linear polarization. It also changes the probe intensity, but it could be easily compensated varying the aperture of PH-1. In addition to this, our polarizer working in transmission introduces a chirp that temporally broadens the pulse. On the other hand, the polarizer has been chosen to have extremely thin (100 µm) Brewster-angled windows, so that the overall chirp introduced in the probe pulse could be neglected.

On the pump path, we mounted Gold mirrors for their high reflectivity in the mid-infrared range. The optical path between GaSe crystal and sample has been designed for minimizing the path length, because the pump has a high divergence and, when approaching 20 µm wavelengths, the air infrared absorption comes into play, and should be minimized. The lens L that focalizes the pump beam onto the sample is a key element of the setup, since a good focalization of the pump is a necessary step to be successfull in a pump-probe experiment. We use a lens made by Zinc Selenide (ZnSe), with a nominal focal length of 10 cm. The effective focal length of the pump beam is larger, because of the pump divergence, around 13 cm. Changes in the pump wavelength can sligthly modify the effective focal lenght, considering that the refractive index is not constant, especially for wavelengths larger than about 14 µm. The transmissivity of the lens to mid-IR pulses is larger than 70% below 14 µm and decreases smoothly for larger wavelengths.

Pump and probe beams must have different focus sizes on the sample. The probe beam should be smaller than the pump one, because we want to probe a region of the sample with a homogeneous pump excitation. On the other hand, a uniform excitation cannot be achieved simply making the pump spot larger, since we have a pump intensity limited to the few µJ per pulse produced in the twin-OPAs (Chapter 4). We used a $SM_{Ag}$ with a focal length of 35 cm, so that the resulting focus (Fig. 3.26) is quite long, and if we displace the sample of a few mm away of its optimal position, no appreciable changes occur in the probe focalization. The same consideration does not hold for the pump beam, whose focus is rather short. We therefore first place a pinhole with a diameter of 250 µm in the location of the focus of the pump; then adjust the direction of the pump beam to be exacty in the center of the pinhole and place a second adjustable aperture about 1 m away on the pump path; finally, we allign the probe in the first pinhole and on the second, to ensure spatial superposition and collinearity, respectively.
Silicon-based photodiodes are not sensitive to long wavelength radiation ($\lambda > 1.1$ µm), and therefore, even if a fraction of the transmitted or reflected pump impinges on the sensitive area of the photodiode, no photoinduced current is generated.
The acquisition of a pump-probe trace is done scanning with the mechanical translator and acquiring the for each step, i.e. for each pump-probe delay, a large number of pulses.
Finally, we mention that we pump and probe optical paths are more than 6 m, after their splitting in the first beam splitter. The search for time-zero, the temporal coincidence, is not a straighforward task. Similar to the tricky expedient adopted to find the temporal coincidence in the DFG, we use a thin BBO cut for second harmonic generation/sum frequency generation. However, here we cannot use directly the mid-IR radiation, but use as signals the probe and the signall of OPA2. In a slight noncollinear geometry, a new green spot appears in the center, when temporal coincidence is reached. It correspods to the sum frequency of the signal of OPA2 and probe. As a consequence of the tiny misalignment between the signal of OPA2 and the DFG signal, this procedure gives only an approximate time-zero for mid-IR pulses. The correct pump and probe time zero will be found will lie in the proximity of the delay identified with thi procedure.

## 3.5 Acquisition system

We introduce here two acquisition systems used, the first based on the lock-in amplifier and the second on two *balanced* photodiodes. Every pump-probe trace presented in this thesis is acquired using to the lock-in amplifier, but we tested also the balanced photodiodes. The sampling rate of the acquisition board we had at our disposal (3 MHz) is very close to the undersampling limit of the signal produced in the photodiodes, and for this reason the lock-in acquisition system resulted better performing. Nevertheless, balanced photodiodes are the most "natural" way to measure the variations in probe reflectivity or transmittivity, as we will see in the following, and have many advantages.

#### Lock-in amplifier

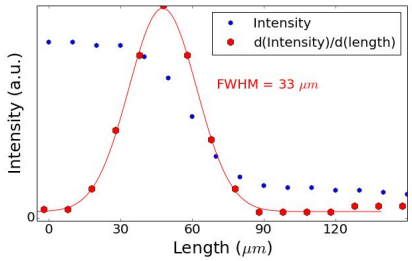


Figure 3.26: Knife edge measurement of the probe beam in its focus. Its width is smaller enough with respect to the pump focus, which is approximately 200 µm, as measured with a pinhole.

Lock-in amplifier is an well-estabilished and widely applied instrument for signal acquisition. It is especially useful when revealing signals which are little variations over a noisy background. In Fig. 3.24, we see that we modulate the pump signal with a square wave modulation signal $m(t;\nu_0)$, with frequency $\nu_0$. This is done thanks to a mechanical chopper, that stops the beam at regular intervals $1/\nu$. Calling $f_{\text{rep}}$ the laser repetition rate, the relation $\nu_0 \ll f_{\text{rep}} = 1\,\text{kHz}$ must hold. The changes in probe reflectivity or transmittivity induced by the pump pulses are then modultated by the modulation signal $m(t;\nu_0)$. The lock-in amplifier just performs an analogical time-integration of the differential current $i_\text{A} - i_\text{B}$ multiplied by $m(t;\nu_0)$ and then amplifies the signal so-obtained. Every contribution to the differential current which does not follow the profile of $m(t;\nu_0)$ is averaged to zero over a long enough integration time $T \gg 1/\nu_0$, and only the contribution to the differential current which contains the frequency $\nu_0$ remains. The integration time determines the allowed bandwidth of the extracted signal, and so its signal-to-noise ratio. We typically used integration times of 100 or 300 ms, chopping at 320 Hz. In the described configuration, the reference photodiode PD-B is not strictly essential, but it helps the lock-in in eliminating the probe intensity fluctuations from the extracted signal and to get the desirable experimental configuration of a "null measurement". To do this, we set the apertures of PH-A and PH-B in order to equalize the currents generated in the two photodiodes, which are monitored in an oscilloscope. Intensity fluctuations in the probe beam are then roughly canceled out in the difference $i_\text{A} - i_\text{B}$.
We chose to employ Silicon-based photodiodes with a large sensitive surface, because of their slow response. The output current of a photodiode is proportional to the intensity of the light impinging onto its sensitive surface, at a given wavelength. Indicating with $\mathcal{R}$ the quantity we are interested to study (typically $\mathcal{R} = R$ or $T$, i.e. —respectively— reflectivity or transmittivity of the probe), the output of the lock-in amplifier is a voltage proportional to $\Delta\mathcal{R}(\tau) = \mathcal{R}_\text{A}(\tau) - \mathcal{R}_\text{B}$. The quantity that properly indicates how the physical quantity $\mathcal{R}$ varies, when the sample is stimulated by the pump, is the fraction

$$\frac{\Delta\mathcal{R}(\tau)}{\mathcal{R}}\,. \tag{3.5}$$

The measure of $\mathcal{R}$ can be done once for a pump-probe experiment, since it remains constant. In order to do it, we chop the probe beam, for example, with reference to Fig. 3.24, between $\text{M}_\text{Ag}$ and $\text{SM}_\text{Ag}$ to obtain an output of the lock-in amplifier proportional to $\mathcal{R}$.

### Balanced photodiodes

With Balanced photodiodes we indicate two photodiodes (let us call them "channel A" the probe and "channel B" the reference) in reverse bias. This means that the

photoinduced currents of A and B have opposite sign. The subtraction (actually, the sum of the signals from A and B) occurs before of the pre-amplification stage, and this gives a low noise differential signal. We used Thorlabs PDB210/AM. The differential signal is then sent to an acquisition board, to be digitalized, and it is possible to acquire at the same time the difference $i_- = i_\mathrm{A} - i_\mathrm{B}$ and the reference $i_\mathrm{B}$. If $i_- = 0$ out of pump-probe temporal coincidence, the ratio $i_-/i_\mathrm{B}$ is the fractional change in $\mathcal{R}$.

$$\frac{\Delta\mathcal{R}(\tau)}{\mathcal{R}} = \frac{i_-(\tau)}{i_\mathrm{B}} \tag{3.6}$$

The noteworthy aspect of a balance photodiode is that $i_-$ and $i_\mathrm{B}$ are digitalized pulse by pulse. Intensity noise over the probe pulses is canceled out pulse by pulse, as shown in the following. If the intensity of the pulse $I$ increases by a factor $(1+\epsilon)$, the current generated in the phododiodes will increase by the same factor, since they work in the linear regime. Writing $i_\mathrm{A}(\tau) = i_\mathrm{B} + i_-(\tau)$, we get

$$\left(\frac{\Delta\mathcal{R}(\tau)}{\mathcal{R}}\right)_{I(1+\epsilon)} = \frac{(i_\mathrm{B} + i_-(\tau))(1+\epsilon) - i_\mathrm{B}(1+\epsilon)}{i_\mathrm{B}(1+\epsilon)} = \frac{i_-(\tau)}{i_\mathrm{B}} = \left(\frac{\Delta\mathcal{R}(\tau)}{\mathcal{R}}\right)_I . \tag{3.7}$$

Therefore, the $(1+\epsilon)$ cancels out pulse-by-pulse, not simply on average —having confidence in the randomness of $\epsilon$. This is true under the assumption that not only the photodiodes, but also the response of the sample is linear with the intensity, for small $\epsilon$. It is actually what we expect for a very weak probe. In the more general case, Eq. 3.7 has to be corrected with terms $\propto \epsilon^2$ and larger.

Furthermore, the adoption of an acquisition system based on a balance photodiode opens to a statistical analysis of the pump-probe spectroscopy data. In fact, for a given $\tau$ we acquire $N$ pulses and can calculate not only their mean value, but also their variance, skewness and other high-order statistical moments, that can give some physical information about the process under study [22]. Unfortunately the small sampling rate of the digitizer used in these sets of experiments introduced further noise, making the single pulse acquisition less performing than the lock-in acquisition. We therefore discuss in the following data acquired excusively through a chopper plus lock-in acquisition.

# Chapter 4

# Characterization of the Mid-IR pulses

This chapter is dedicated to the characterization of the mid-infrared (MIR) pulses generated with the setup described in section 3.2. It is composed by two parts. In the first, we present an analysis of the spectral content of our MIR pulses, together with general considerations about efficiency and tunability of the pulses generated in the difference frequency generation (DFG) process. In the second, we show the results of the electro-optic sampling (EOS) measurements performed in a thin sample of ZnTe. Thanks to EOS, we perform a full phase and amplitude characterization of the MIR electromagnetic field and verify the carrier-envelope phase stability of the pulses. EOS is a pump-probe measure, and thereby gives as well the proof that the setup works properly.

## 4.1 The Michelson interferometer

In order to introduce the Michelson interferometer built for the characterization of the spectral content of MIR pulses, we proceed as follow: we introduce the detector used to reveal MIR pulses and proceed by describing the optomechanical scheme of the interferometer. It is worth noticing that standard semiconductor-based photodiodes are insensitive to mid-infrared wavelengths. For this reason we turned to but Mercury Cadmium Telluride (MCT) detectors cooled with liquid Nitrogen, which are suitable for mid-infrared light detection. A MCT detector is a photodiode made of the alloy $Hg_{1-x}Cd_xTe$. HgTe is a semimental, CdTe a semiconductor, with a bandgap of about 1.5 eV. The bandgap of the alloy is determined by the Cadmium fractional concentration $x$, and can be varied from 1.5 eV (for $x = 1$) to 0 (for $x = 0$), almost linearly. Therefore, the value of $x$ determines the spectral location of the peak of sensitivity of the detector, and influences also the working bandwidth. Since we need to measure long wavelengths, we need a MCT detector with a poor fraction of Cadmium. The resulting bandgap is of the same order of magnitude of the thermal energy $k_BT$ at room temperature. Hence, at room temperature, electrons are thermally driven to conduction band, and thermal noise makes the detection of infrared light with a MCT at room temperature a very hard task. This is the reason why the photodiode should be cooled down to about 77 K, putting it in contact with a thermal reservoir at a temperature close to that of liquid Nitrogen.

We used the Hamamatsu P5274-01 MCT photoconductive detector, whose picture

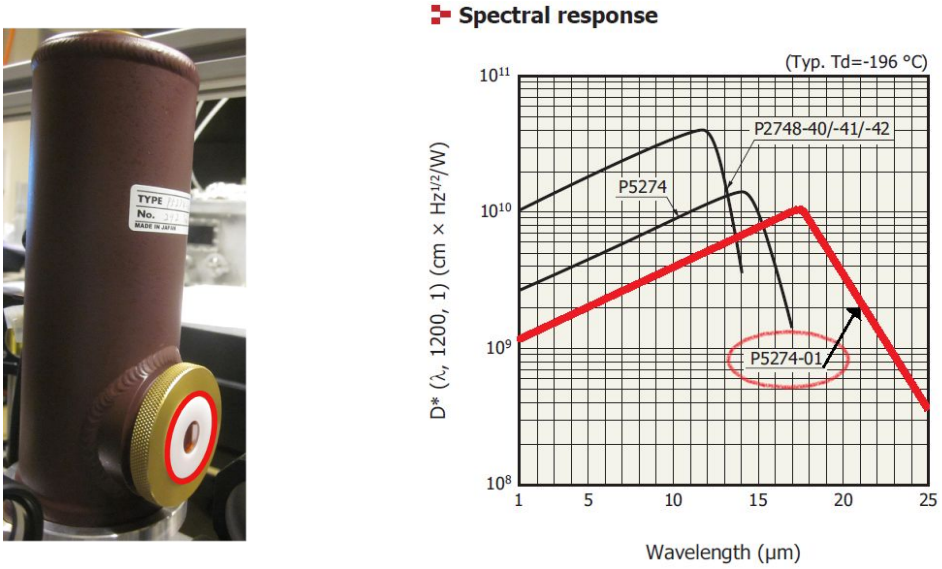


Figure 4.1: Left: picture of the Hamamatsu P5274-01 MCT photoconductive detector, with its dewar to be filled by liquid Nitrogen and the 1 mm sensitive area in the center of the red ring. The window, that separates the photodiode, which stays in vacuum, from the outside, is made of Thallium Bromo-Iodide KRS-5, which is transparent in the near- and mid-infrared range. Right: curve of spectral sensitivity, in red, from Hamamatsu P5274-01 datasheet. The spectral response function is plotted versus the wavelength of the incident light.

and spectral sensitivity are represented in Fig. (4.1). The peak sensitivity is at 17.5 µm, the cutoff around 22 µm.

In order to carry out a spectral characterization of the mid-infrared pulses, it is possible to both design a grating that spatially separates the wavelengths, sending them to an array of photodiodes, or to construct a Michelson interferometer. The choice of the grating spectrometer is the most common for near-infrared pulses, but for mid-infrared ones, its critical point is the array of MCT detectors which is very expensive to make. We opted to construct a Michelson interferometer, which requires a single MCT. Its scheme is represented in Fig. (4.2), together with the description of its components. To avoid saturation and effects of nonlinearity on the response of the infrared detector, we filter the mid-infrared beam before the detector, first selecting only the central part of the beam, thanks to PH, and then by means of a pellicle wire-grid polarizer, POL. The polarizer works following Malus' law, and, since our electromagnetic radiation is fully polarized, we can block as much radiation as we need, simply rotating the wire-grid polarizer. Moreover, we leave the beam unfocused on the detector.
A rough alignement of the Michelson can be done with a He:Ne laser pointer collinear to the mid-infrared beam. On the BS surface, the pulses of the two arms of the interferometer have to be superposed in space and time, in order to interfere. BS does not need to have exactly a 50:50 splitting R:T ratio, since, before impinging on the MCT, each beam should be both reflected and transmitted by BS. On the detector the electromagnetic fields from the two arms are thereby summed with the same coefficient. The mechanical translator that controls the position of $M_2$ has a sub-micrometric screw controlled via a Physik Instrumente (PI) controller. We can

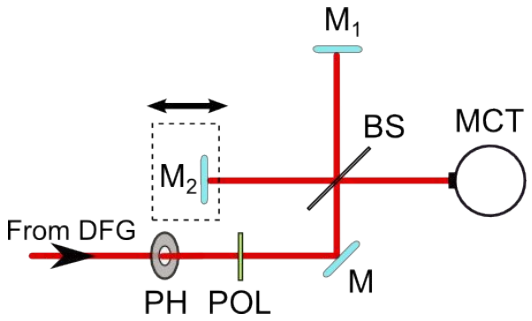


Figure 4.2: Scheme of our Michelson interferometer. PH: pinhole; POL: polarizer; M, $M_1$, $M_2$ Gold mirrors, $M_2$ mounted over a mechanical translator with remote control, BS: pellicle beamsplitter, with a R:T ratio approximately 50:50 for light polarized in the horizontal plane; MCT: detector.

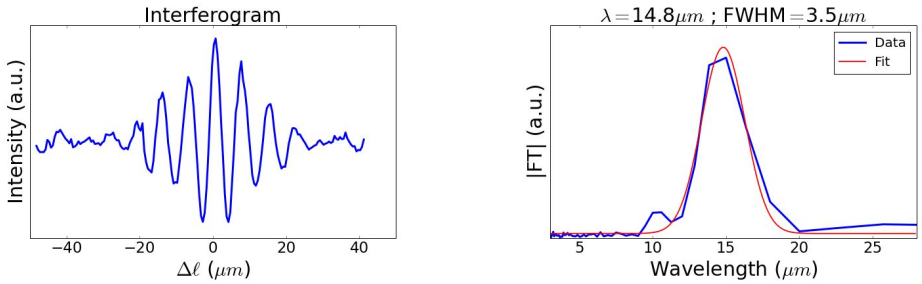


Figure 4.3: Left: Example of a Michelson interferogram. Right: Modulus of the Fourier transform of the interferogram on the right; the plotted abscissa is $2\pi/k$, where $k$, the wavevector, is the Fourier conjugate of $\Delta\ell$. The fit is Gaussian.

hence choose the absolute displacement of each step of $M_2$.
The inteference trace (the *interferogram*, for example Fig. 4.3 on the left) is acquired in the following way. We perform a scan over the position of $M_1$, in a region symmetric around the point for which the two arms have equal length. We call $\Delta\ell/2$ the length of each step of $M_1$, which determines a $\Delta\ell$ variation in the optical path. The condition $\Delta\ell \ll \lambda_{\mathrm{DFG}}$ ensures to sample correctly the interference pattern. $\Delta\ell$ determines the $x$-axis in the interferogram. For each step, we acquire the intensity of $N$ pulses, and plot their average. Tyipical values are $\Delta\ell = 1$ and $N = 64$ or 128. The acquisition of the pulse intensity is triggered by the laser repetition rate-trigger. The acquisition and on-line data analysis program was written in LabView.

As explained in the introduction to section 3.3, Michelson interferometry gives us the access to the energy content of the light pulses. In order to see it, we only need to Fourier transform the interferogram. An example is reported in Fig. (4.3), where a Gaussian fit is also plotted.

## 4.2 Spectral range, bandwidth and tunability

In order to generate the "best" DFG pulses, we can vary many parameters, such as the spectral position of the OPAs' signals, their spectral width, their temporal superposition in the GaSe crystal (of particular importance because they are chirped), in addition to the phase matching angles of the GaSe crystal. Our goal is to produce pulses with a high intensity, with a wavelength tunable in the mid-infrared and

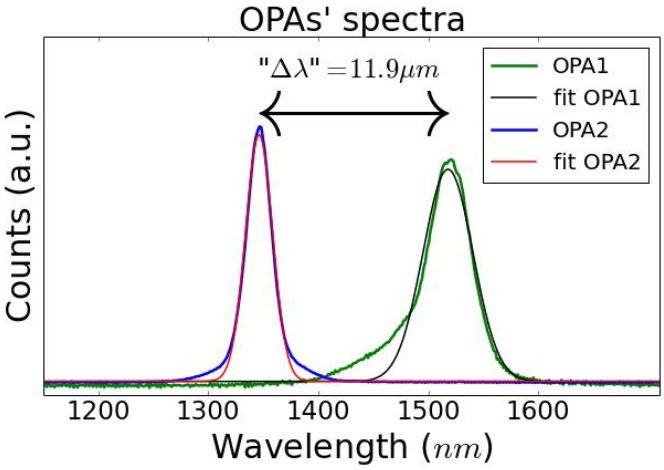


Figure 4.4: Example of the spectra of the two OPAs (signals only). Fits are Gaussian, although the spectra are not Gaussian in their tails. Nonetheless, we use Gaussians because we are not interested in investigating the exact spectral shapes, but only in estimating their peak positions and bandwidths.

having control on their spectral content. The last point is equivalent to be able to make *pulse shaping*. We usually aim to have a clean and narrow bandwidth, but —as we will see later— it could be interesting also to have pulses with large beats between two groups of frequencies.
We here explain some procedures allowing for the reproducible generation of MIR pulses.

In Fig. 4.4 we can see an example of OPAs' spectra, centered around 1345 nm and 1520 nm. Once chosen the OPAs, we can look for the temporal superposition and the GaSe angles that maximise the DFG intensity. In a naïve picture, we could span the whole mid-infrared range simply varying the spectral positions of the two OPAs within their near-infrared range. The closer in energy the OPAs, the larger the DFG wavelength. At "zero-order approximation" we can observe it in Fig. 4.5. We note, however, that in general, once these two parameters are optimized, the resulting DFG has not the OPA2-OPA1 peak-to-peak difference frequency. This is explained by the chirp and large spectral width of the two signals impinging the GaSe crystal, together with the non-constant gain of the DFG process at different wavelengths, decreasing for larger generated wavelengths. Indeed, if the spectra of the OPAs are pushed one close to the other (leading in theory to a larger DFG wavelength), the generated DFG pulses have a smaller wavelength than expected, if we simply maximise the intensity. It means that the tails of the OPAs' spectra are phase matched and in temporal coincidence, not the peaks.

We mounted the crystal like in Fig. 4.6, the crystal being free to move in $\theta$ and $\phi$ (and in $z$), but not in the third angles $\psi$, which is kept fixed to $\pi/2$. Both $\theta$ and $\phi$ are important, in contrast with the case of BBOs, where (for type-II phase matching) only the angle equivalent to $\psi$ plays a role in the search of the phase matching. The DFG intensity is a periodic function of $\phi$, with periodiod $2\pi/3$.

A first possibilty is hence to keep fixed the two OPAs and changing the delay $\tau$, each time slightly adjusting the angles $\phi$ and $\theta$ of the crystal, in order to reach the best phase matching conditions for the frequencies in temporal coincidence. What

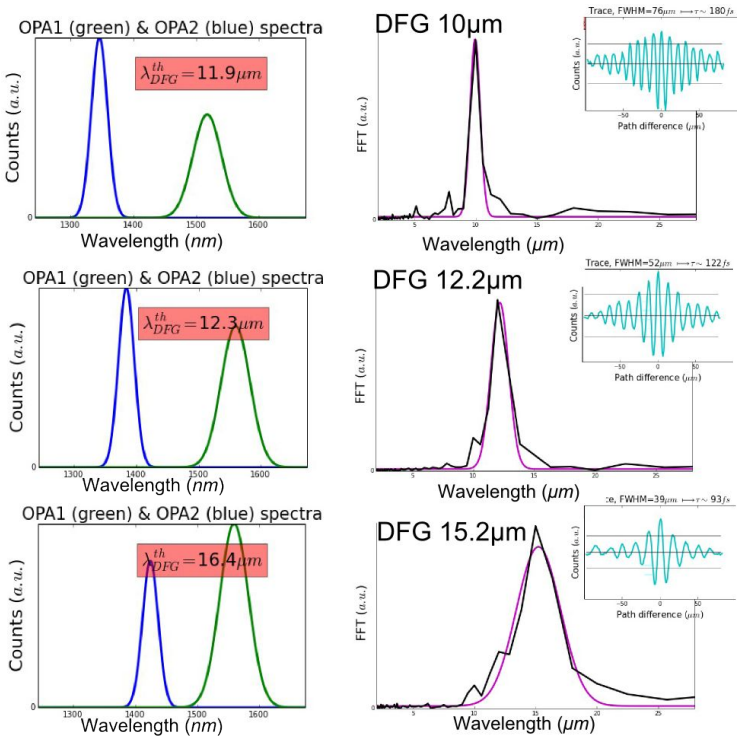


Figure 4.5: Left: OPAs' spectra for three different configurations. Only the Gaussian fits are reported, to improve graph clarity, and $\lambda^{th}_{DFG}$ is the wavelength that would be generated in a peak-to-peak difference frequency generation process. Right: relative DFG spectra, from Michelson interferometry measurements, obtained maximizing the intensity for the fixed OPAs on the left.

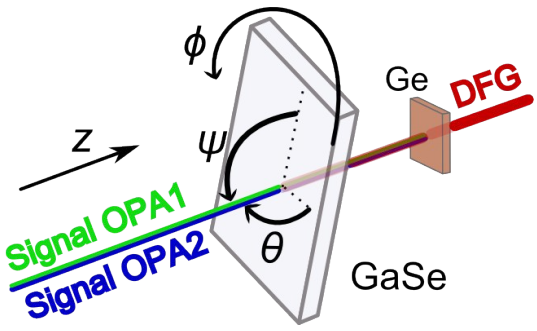


Figure 4.6: GaSe crystal with relevant angles. The thin crystal is kept with its face orthogonal to the impinging beams (hence $\psi = \pi/2$).

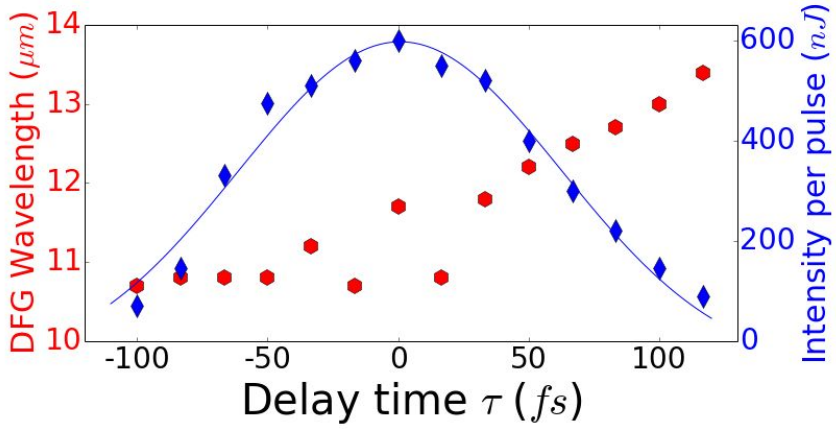


Figure 4.7: Left axis (red hexagons): DFG wavelengths, obtained with the procedure described in the text; Right axis (blue lozenges): corresponding DFG energies per pulse. The solid line is a Gaussian fit. The resulting FWHM is approximately 140 fs, and gives a hint about the OPAs' temporal width.

we note, is that the phase matching conditions vary rather smoothly, and for this reason we initially fixed the angles. A prototypical example is depicted in Fig. 4.7, where we plotted (red hexagons) the central wavelength of the DFG, as resulted from the Gaussian fit, versus the delay $\tau$ between the two pulses, whose spectral content are those plotted in Fig. 4.4, with a "nominal" peak-to-peak difference frequency corresponding to a fwavelength of 11.9 µm. The behaviour seems to be linear until $\lambda_{\mathrm{DFG}} = 10.7\,\mu\mathrm{m}$, where a sort of saturation is reached. It could be understood better considering also the intensity of the pulses (blue lozenges). For $\tau = 0$ the intensity has its maximum and the generated DFG wavelength is very close to the wavelength estimated from OPAs' peak-to-peak difference frequency (11.7 µm versus 11.9 µm). The intensity then decreases with a Gaussian shape (blu line) once we add a temporal delay between the two OPAs. The saturation for negative delay times is probably caused by the absence of phase matching conditions: it is possible to generate DFG pulses with lower wavelengths, but only changing $\theta$ or $\lambda_{\mathrm{OPAs}}$ significantly. The highest wavelength generated in Fig. 4.7 seems to be limited essentially by the absence of chirped spectral density in regions allowing for higher DFG wavelengths. The width of the spectra has a trend that follows the growth of $\lambda_{\mathrm{DFG}}$, although with more irregularities, being larger for larger wavelengths. This suggests that pulses with large DFG wavelengths are shorter than those with small wavelengths, and therefore would have a higher peak amplitude of the electric field, with respect to other pulses with the same pulse energy but smaller wavelength. Since the energy per pulse decreases for larger wavelengths, this fact goes in the direction to balance, on the electric field strength, the loss of energy per pulse.
At first glance, the linear behaviour of $\lambda_{\mathrm{DFG}}(\tau)$ appears broken by the two points at $\tau = \pm 17$ fs, but we should consider that those two pulses contain a beat between wavelengths at 10.9 µm and 13.1 µm, and that the Gaussian fits only the first, which has a larger spectral weight.
Finally, the energy per pulse measurement of Fig. 4.7 is a measurement of the correlation function $\gamma_{12}(\tau)$ between the two OPAs' signals, Eq. 3.1, mediated via the the interaction with the GaSe crystal. For the same reasons pointed out when we

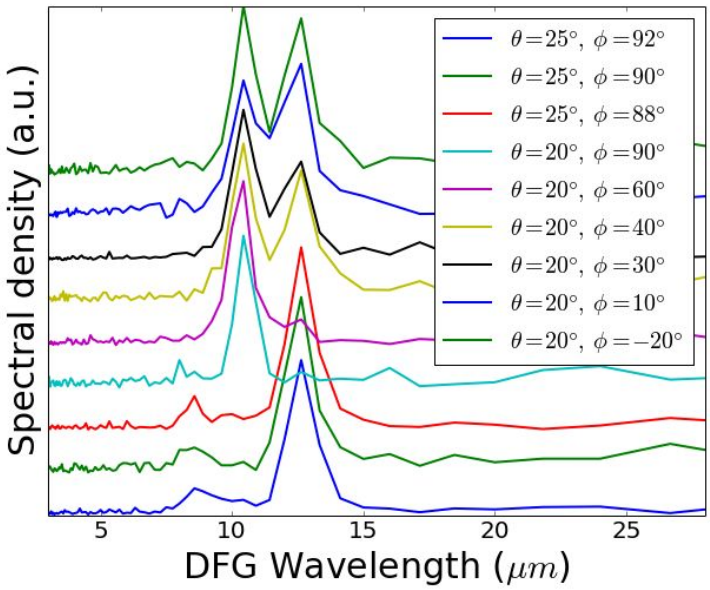


Figure 4.8: Sequence of spectra obtained varying only the GaSe angles. We can keep only the peak at 10.5 µm, only the peak at 13 µm, or a mixture of both, simply choosing the suitable angles.

dealt with Michelson interferometry, also this kind of correlation process does not give the exact time duration of the pulses, but, nevertheless, gives a hint on it[1]. All the FWHMs of the OPA1-OPA2 correlation's traces lie in the interval between 110 fs and 230 fs.The DFG pulses would have a similar temporal width.

Another possibility is to change the GaSe angles keeping fixed the two OPAs. In particular we observe that if we change $\phi$, we can span over a rather large set of DFG wavelengths. $\theta$ is used mainly to eliminate pulse beats. When in the DFG spectrum there are two peaks, usually we can select the more infrared peak increasing $\theta$, and viceversa if we want the less-infrared peak.
Fig. 4.8 shows some DFG spectra generated with different angles, indicated in the inset.

DFG pulses have an energy per pulse strongly dependent on their wavelength. In Fig. 4.9 we report a plot of energy per pulse versus DFG wavelength. Since data were acquired in non homogeneous conditions, and hence result hardly comparable, Fig. 4.9 should be interpreted as a proof of a trend, not as an exact reference curve for mid-infrared photon downconversion in GaSe. The maximum energies are of approximately 3.5 µJ per pulse[2], corresponding to $\lambda_{\mathrm{DFG}} = 8\,\mu\mathrm{m}$; energies per pulse between 1.5 and 2.5 µJ are commonly generated with $\lambda_{\mathrm{DFG}}$ ranging from 4

[1] As discussed in section 3.3, the spectral content of the MIR pulses will set only the lower limit for the pulse duration; i.e. the pulse duration under the assumption of transformed-limited pulsed. We argue that being such a lower limit of the same order of the pulse duration of the pulses used to generate the MIR pulses, the information given by the Michelson, will give a realistic estimate of the pulse duration. A more direct measurements is given in the following section.

[2] Measured after the Germanium window, which cuts approximately 40% of the mid-infrared pulse intensity.

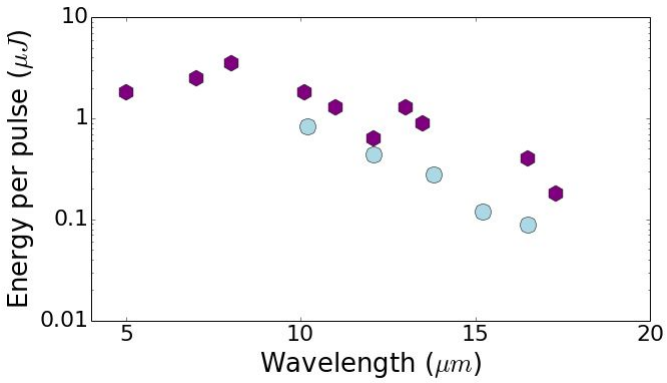


Figure 4.9: DFG energy per pulse, in log-scale, measured after the Ge window. Purple hexagons pertain to an inhomogeneous set of data, while light blue circles refer to pulses obtained with the same conditions and procedures.

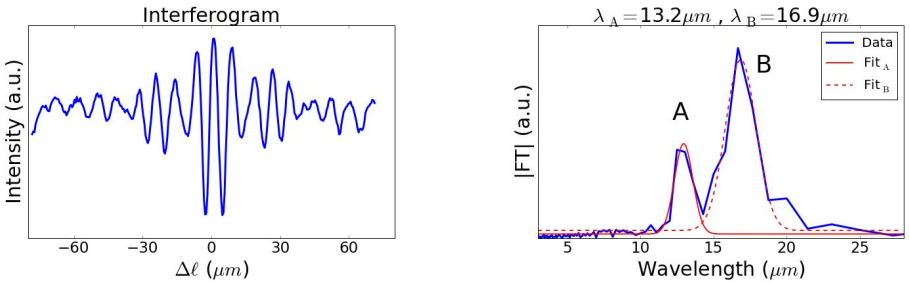


Figure 4.10: Left: interferogram with symmetric beats. Right: modulus of the Fourier transform of the interferogram on the right, together with the fitted curves for the isolated frequency peaks that produce the beats.

and 13 µm. At larger wavelengths, the energy per pulse decreases quite fast, and, for $\lambda_{\mathrm{DFG}} = 17$ µm, only 200 nJ could be generated. Large wavelengths have also large bandwidths, and thus the spectral tails can exceed the 20 µm, but no pulse peaked over 20 µm was produced.
The relative efficiencies, calculated as the ratio between the energy per pulse of the DFG and that of the two signals impinging on the GaSe, are below 3%, consistent with what reported by many authors (see, for instance, [14]).
The fast decrease in pulse intensity for long mid-infrared wavelengths is a joint consequence of worse phase matching conditions and lower transparency of the crystal. In particular, the transparency plays the decisive role, because GaSe has an infrared absorption coefficient which grows througouth the infrared, and changes slope around 17.5 µm. The infrared transparency cutoff for Gallium Selenide is usually set to 18 µm

### Beats

Fig. 4.10 contains the example of a beats between two well-separated groups of frequencies, and it is visible both in the interferogram and in its Fourier transform. We are able to tune the spectral weight of the two wavelength coomponents, and hence to make an elementary pulse shaping, from narrow peaks (only for $\lambda_{\mathrm{DFG}} <$

12 µm), to very broad peak (especially in the region above 14 µm), and also to have tunable beats between two or even three different wavelengths, in the whole range of tunability of the DFG.
An advantage of using a pulse with a beat as a pump in a pump-probe experiments resides in its shorter time duration, which makes the amplitude of the electric field larger. More ambitously, it could induce peculiar phenomena in a material when stimulating in proximity of the nodal points of its envelope. Indeed, in a naïve picture, a sinusoidal electric field induces the electric dipoles in the pumped material to oscillate with its frequency; if the dipoles are, for example, accelerating towards their stretching position when a node of the pulse arrives, they suddenly experience a force in the opposite direction. It could therefore be interesting to study the dynamics induced by such pulses. In order to do it, a complete control over the pulse shape is required (Michelson interferometry is in general not enough, because it does not account for the chirp), together with a material whose response follows in some way the pump pulse.

## 4.3 Electro-optic sampling in a ZnTe crystal

### 4.3.1 Electro-optic sampling (EOS)

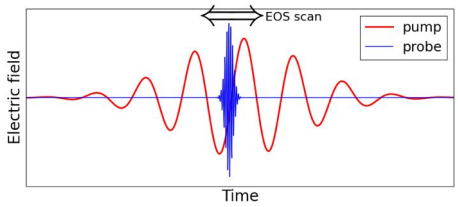


Figure 4.11: Pumpe and probe pulses in an EOS experiment.

Electro-optic sampling (EOS) is an optical time-domain spectroscopy technique, which exploits the Pockels effect, the effect due to a second-order nonlinear polarization to measure the amplitude and phase of mid- and far-infrared light pulses. In short, as shown in Fig. 4.11, by means of a second order nonlinear interaction it is possible to map the instantaneous infrared electic field on the polarization state of a visible (near-infrared) ultrashort pulse, whose envelope is shorter than the infrared wavelength. By scanning the delay between the infrared and visible pulse it is possible to measure the infrared field shape in the time domain. The technique makes use of two pulses Fig. 4.11 and consists of a sequential sampling, like a pump-probe experiment. For this reason we use the same setup of pump-probe experiments, Fig. 3.24, with only a change in the acquisition of the probe beams, as depicted in Fig. 4.12.
If the polarization of a material has a quadratic term in the applied electric field, its refractive index $n$ becomes linear in the field, as explained in chapter 1. For light pulses, this is precisely the optical Pockels effect, analogous of the optical Kerr effect (where $n$ is quadratic in the field), but for non-centrosymmetric material.
In order to perform EOS, the employed material has not only to exhibit Pockels effect, but also to be uniaxial birefringent. We have already dealt with uniaxial birefringence in previous chapters. Here we only remind that light travelling in a birefringent crystal experiences a different refractive index whether its polarization is parallel or orthogonal to the optic axis. At the end of the crystal, the parallel and orthogonal polarization components are delayed, and hence the total polarization

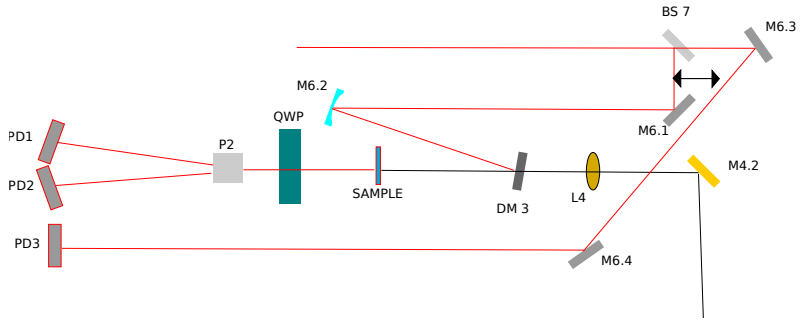


Figure 4.12: Pump-probe and electro-optic sampling experimental setup, almost identical to Fig. 3.24. Mid-infrared pump is drawn by grey lines, the optical probe by red lines. In the case of EOS, the experiment is "in transmission", and the sample is a crystal of ZnTe, 50 µm thick. After the sample, there is a quarter-wave plate (QWP), which makes the light circularly polarized, and a Wollaston prism (P2), which separates light with orizontal and vertical polarization. The photodiodes PD1 and PD2 acquire the pulses coming out of the Wollaston prism. PD3, the photodiode for the reference beam, is not used in EOS.

is rotated. We just described the working principle of wave plates. In a half-wave plate, for example, the length of the crystal is set to produce a half-wave delay between the two polarization components. When light is polarized at $\pi/4$ with respect to the optic axis, at the end of the half-wave plate it will be rotated of $\pi/2$ about the optic axis. No rotations occur if the light is fully polarized parallel or perpendicular to the optic axis. The phase delay $\Gamma$ depends linearly from the length of the crystal and the birefringence $\Delta n = n_\mathrm{o} - n_\mathrm{e}$, after an integration along the probe beam propagation axis $x$,

$$\Gamma = \int_0^L \frac{2\pi\Delta n(x)\mathrm{d}x}{\lambda}\,, \tag{4.1}$$

where $\lambda$ is the wavelength and $L$ the length of the crystal.
When an electric field is applied on such materials, it changes the refractive index in the direction of the electric field, and therefore changes the polarization rotation inside the material. If the electric field is produced by a DC or a slowly-varying voltage, the material acts as a Pockels cell, a very common electro-optic modulator. More generally, this also happens when the electric field is oscillating with a multi-THz frequency (as in the case of our pump pulses), we talk about *electro-optic effect*, provided that the envelope of the *probe* is shorter than the period of the pump, and its frequency much higher than that of the pump.
A suitable material for electro-optic sampling with our configuration is Gallium Selenide, that, in addition to the generation of the mid-infrared pulses, can be also used to "detect" them by means of electro-optic sampling measurements [13]. Another suitable crystal for electro-optic sampling is Zinc Telluride (ZnTe), which is usually employed in THz detection. However, it is reported its use in detection also of shorter wavelengths, down to about 10 µm [17].
We used a ZnTe crystal, approximately 50 µm thick. The thickness is an important parameter. Larger crystals allow for a larger polarization rotation only as long as the pump-probe "walk-off" is negligible, corresponding to the case in which $\Delta n(x)$ is constant in 4.1. If it is not, the mismatch between the group velocity of the probe

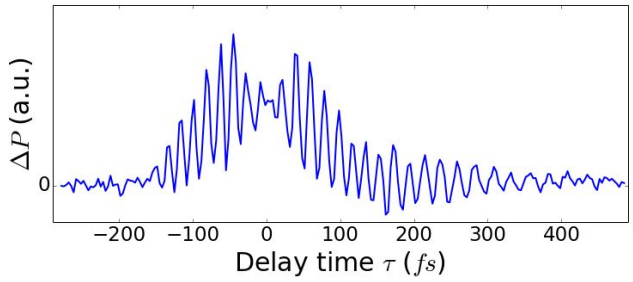


Figure 4.13: Example of electro-optic sampling trace. The polarization rotation oscillates with the pumping electric field. The oscillations are not about zero because of the "incoherent" peak. For negative $\tau$ the sampling is performed over the front part of the pump pulse. The trace is not symmetric about $\tau = 0$, having a longer tail in the back of the pulse.

and the phase velocity of the mid-infrared field make such that optical sampling averages over different phases of the pump's electric field, and the EOS effect is partially or totally lost.
The description of the setup is contained in Fig. 4.12. Even in absence of the pump, the polarization of the probe rotates, because the ZnTe thin slab is a wave plate. We rotate the ZnTe crystal and the quarter-wave plate in order to have an equal amount of light on the two photodiodes. The pump beam is chopped, and the signal PD1-PD2 sent to a lock-in amplifier, as described in section 3.5. The output of the lock-in is thus a measurement of the polarization rotation induced by the pump's electric field. The rotation is linear in the refractive indexes, and so it is linear in the pump's electric field. In other words, it is a measure of the electric field of the pump pulses. A complete sampling of the electric field is performed scanning sequentially over the pump-probe delay time $\tau$, and gives a complete phase and amplitude characterization of the mid-infrared pulses.

It is worthwhile to point out again the main peculiar features that make possible the electro-optic sampling in our experiments.
First of all, the presence of of light with a large wavelength, say $\lambda > 8\,\mu m$, in the mid-infrared range, sometimes called "multi-THz range", so as to highlight the proximity to THz physics. Secondly, the carrier-envelope phase stability of the mid-infrared pump pulses. Random-CEP pulses cannot be used for EOS, because, pulse-to-pulse phase fluctuations lead to a polarization rotation averaging to zero. As third point, the use of an ultrashort optical probe, with temporal width of approximately 20 fs. The electro-optic sampling is effective only when the probe light oscillates over many cycles in a region where the the pump's electric field does not change significantly. EOS with THz radiation is in this sense simpler, because it is possible probe optically with 60 or 100 fs pulses.

### 4.3.2 Results

The EOS traces, like the one in Fig. 4.13 have in general two contributions, which we name "coherent" and "incoherent", the first being oscillatory with the pump's electric field and the second not. The modulus of the Fourier transform of the EOS trace gives the spectral content of the pump pulses, and thus can be compared with the result of Michelson interferometry. We stress again that the comparison is pos-

sible in the Fourier domain, not between the traces in the direct space.
There is a fairly good agreement between the spectra obtained with the two methods, although the various spectral components do not have always the same weight. Furthermore, we can select single portions of the abscissa of the electro-optic trace, and perform a Fourier-analysis. For the prototype trace plotted in Fig. 4.13, we observe a clear spectral drift, as can be seen in Fig. 4.14. In general, a behaviour of this kind could be due to the pump chirp or to a response of the material. In our case, Michelson interferometry gives for the pump pulse a quite narrow peak at 10.8 µm (FWHM= 0.8 µm) and a second peak, with approximately the same width, centered at 12.5 µm, but with about a quarter of the intensity of the first peak. We find the first peak in the spectrum of the whole electro-optic trace (black line in Fig. 4.14), with basically the same position (10.7 µm), while the second is slightly shifted. In addition, the peaks have different spectral weights with respect to the result of Michelson interferometry, and there is also a larger long-wavelength tail. Because of the reasons expressed above, we cannot conclude that the inhomogeneous wavelength distribution within the electro-optic sampling trace is due for sure to a chirp in the pump pulse[3], as long as we suppose that the amplitude of the polarization rotation scales linearly with the amplitude of the pumping electric field throughout the EOS trace and that the Michelson interferometry gives the correct spectrum.
In spite of the overall good agremeent between the central wavelength obtained, we observe that the EOS sampling gives systematically a slightly larger wavelength with respect to the Michelson. This is tentatively ascribed to the possible presence of a spatial chirp on the mid-infrared pulses generated in the DFG stage. The Michelson interferometer works on a non-focused beam and, therefore, gives an integrated measurements of the spectral content over the detector area (1 $mm^2$), which is much smaller than the overall beam diameter (30-80 $mm^2$). On the contrary, EOS works on a focal point for the mid-infrared beam. It is reasonable to assume that, should a spatial chirp be present, the shorter wavelengths would be on the center of the beam profile, while larger ones will be on outer rings. Should this be the case, the Michelson will samples only the central part of the beam, therefore giving shorter wavelengths, while the EOS would be more rapresentative of the overall spectra. Further investigation are needed to clarify this discrepancy.

Electro-optic sampling depends on the polarizations of both pump and probe with respect to the ZnTe crystal axis, and also on the intensity of the pump pulses.
The incoherent part of the EOS trace can be reduced and even set to zero reducing the intensity of the pump beam, either using a wire-grid polarizer or placing the ZnTe out of the pump's focus. The second configuration is to be preferred, because if we place a polarizer for the pump, we should rotate also the probe polarization and the ZnTe, in order to remain in the same configuration of EOS. Nonetheless, neither the presence of the incoherent term nor a change in the EOS configuration modify the spectrum —which is the main feature we are interested in— as can be appreciated in the right of Fig. 4.15, which shows three EOS traces (left) and their relative spectra (right). The cyan curve is obtained with pump pulses with 350 nJ per pulse focalized on the ZnSe slab, while in the case of the red curves, ZnTe were placed 1 cm after the pump focus, and for the blue curves a polarizer was used to

[3]If the pump is chirped following Fig. 4.14, it would have bluer light in the front of the pulse, opposite to the chirps treated so far. Indeed, such chirp woud be the result of the difference frequency generation process, not en effect of chromatic disperion.

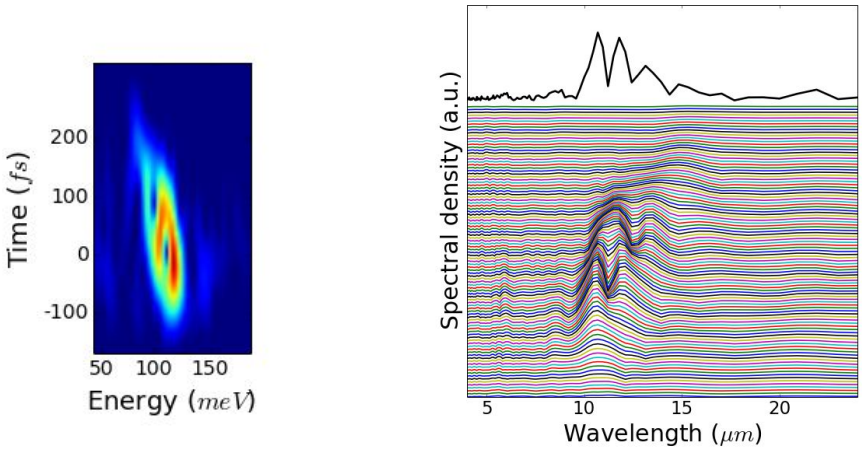


Figure 4.14: Referring to the trace of Fig. 4.13, we sequentially Fourier-analyze the electro-optic trace filtered by a scanning Gaussian window with standard deviation $\sigma = 90\,\mathrm{fs}$. Left: Spectral density color map. Time indicates the center of the Gaussian window, and is negative in the front of the pump pulse. Right: same data, but in a sequential plot, with spectral density versus wavelength. On the top (black line), the spectral density of the whole trace. In both plot, it is clearly visible a non trivial time-domain structure of the spectral density, with a spectral drift, that we think is a sign of the chirp of the pump pulse. Redder frequencies stay mostly on the back of the pulse, differently from the common chirps due to chromatic dispersion.

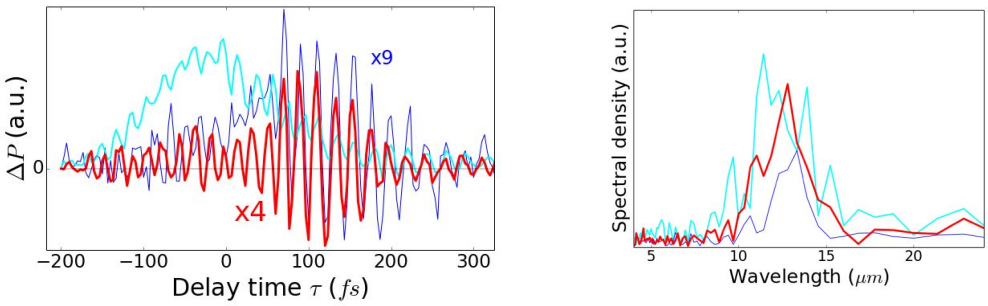


Figure 4.15: Left: EOS traces acquired under different pump intensities, but same wavelengths. The blue trace is multiplied by a factor 9, the red one by a factor 4. Right: relative spectral densities. See text for details.

attenuate the pump, with the ZnTe in the focus.
The red trace contains only oscillations in the polarization rotation; the blue has still a small incoherent term. It is possible to eliminate it rotating more the wire-grid polarizer, but we plotted it with the aim to show that when we modify the polarization of the pump, we change the projection of the electric field over the optic axis, i.e. the effective field amplitude that modulates the birefringence $\Delta n$. At the same time, it does not change with the same rate the total amount of energy released in the crystal. If the incoherent peak is a cause of heating, this consideration explains why in the blue trace there is still an incoherent peak, although the oscillations in $\Delta P$ have half of the amplitude of those relative to the red curve, where no incoherent peak is present.
From Fig. 4.15 we note also that the center of the trace without incoherent peak does not correspond to the center of the incoherent peak. Their are approximately 100 fs apart. This excludes that the incoherent polarization rotation is the effect of a "saturation" of $\Delta n$, which, for very high electric field, could not follow completely the oscillations of the electric field.
From measurements in the changes of transmittivity $\Delta T/T$, we observed a very high peak only in the configurations producing also a non-oscillating polarization rotation. Transmittivity traces contain an oscillating term smaller than EOS. The main and unsolved peculiarity of the incoherent polarization rotation is that it precedes the pump pulse, i.e. we can see it when the ultrashort probe pulse is in coincidence with the front tail of the pump pulse, and it ends when the probe pulse is within the FWHM. Indeed, we expect exactly the opposite behaviour, in which the local thermal heating induced by the pump pulse gives rise to a non-oscillating polarization rotation of the probe that reaches its maximum at the top of the pump envelope and that then decays with the characteristic time for heat dispersion in the sample. All the factors but the last one are coherent with a thermal description of the incoherent peak, which nonetheless cannot be proposed.

Indipendently form the presence of the incoherent peak in EOS traces, the reduction of the intensity of the pump pulses allows us to acquire very controlled and high-quality electro-optic samplings of the mid-infrared field. Typical results are those depicted in Fig. 4.16. As described earlier, the agreement is qualitatively satisfactory, given the small wavelength mismatch discussed for the prototype case of Fig. 4.14.

The angle of the EOS crystal is a fundamental parameter to optimize, in order to do EOS. The thin crystal is held with its plane face orthogonal to $z$, the propagation direction of the beam, and free to rotate about $z$, by any angle $\phi$. Rotating the ZnTe (at fixed pump and probe polarizations), we obtain traces ranging from high incoherent peaks with only very small oscillations, to high oscillating traces, null traces or incoherent peak with a polarization rotation in the opposite side.
We can analyze these series of traces in angle-dependence studying separately the oscillatory and non coherent part. We identify the integral of the Fourier peak as an indicator of the amount of coherent oscillation present in the trace, and the spectral weigth in a region of large wavelengths[4] as indicator of the incoherent part. In Fig. 4.17 the results are shown in polar plots.

Since the pump pulses of the series have two spectral components (right part of

[4] From 25 µm to $\infty$.

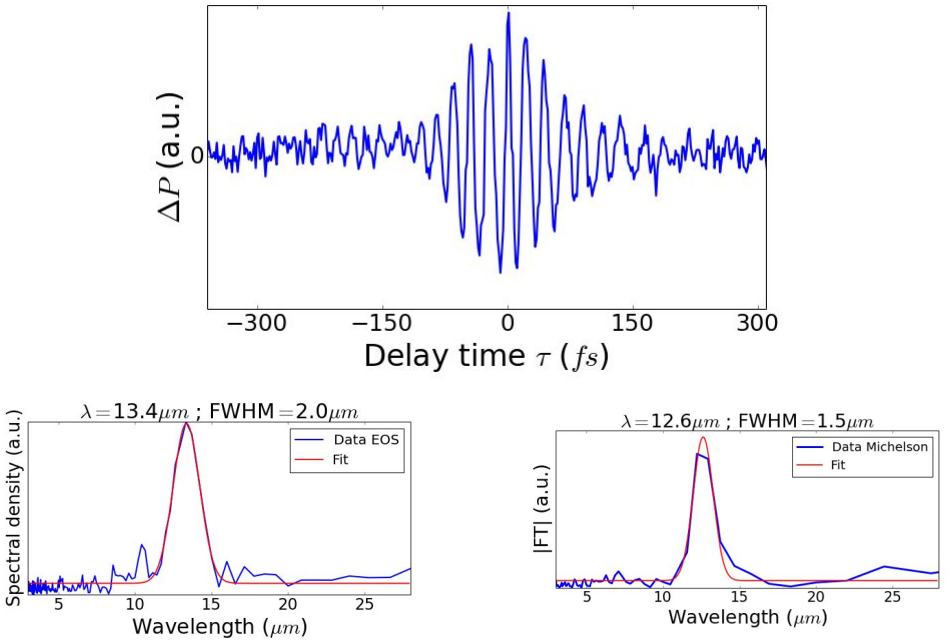


Figure 4.16: Top: EOS trace. Bottom left: spectral density from EOS. Bottom right: spectral density from Michelson interferometry.

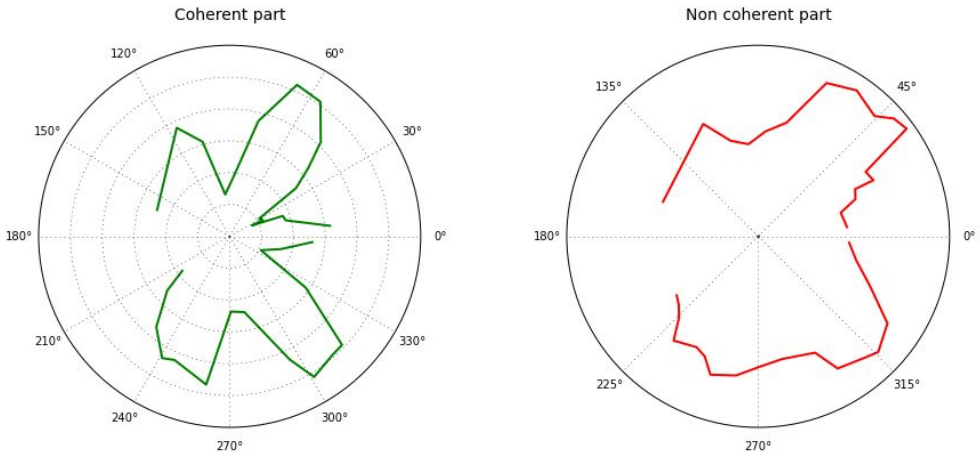


Figure 4.17: Coherent and non coherent parts of the EOS spectrum. The coherent part (left) reproduces clearly the $\pi/3$ rotational symmetry of ZnTe. The series is not complete over $2\pi$, and therefore it was not possible to analyze data around $\phi = \pi$. It is however rather easy to imagine the polar behaviour also at those angles. The incoherent part (right) has a different $\phi$-dependent structure, suggesting a $\pi/2$ periodicity.

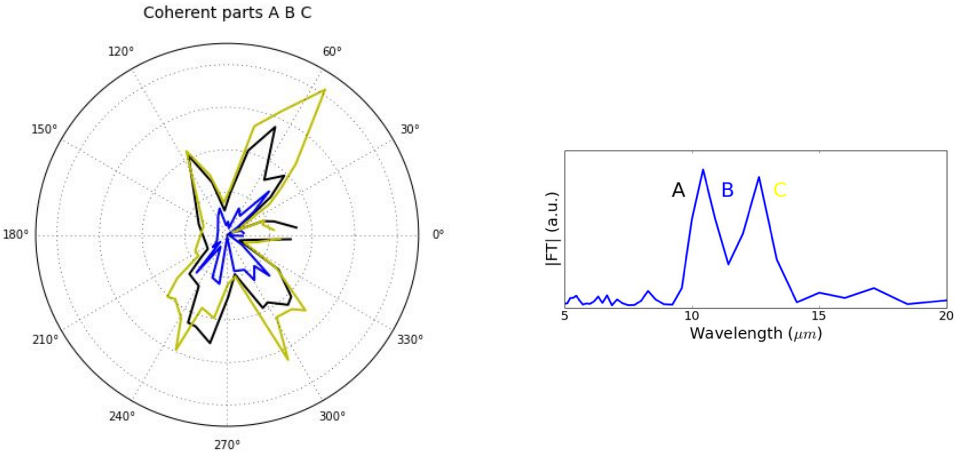


Figure 4.18: Left: polar plot of the coherent parts A (black), B (blue) and C (yellow). Right: spectral density of the pump pulse, from Michelson interferometry, and the three domains of integration: A, B and C.

Fig. 4.18), we can analyze each peak separately, and divide the region in the three sub-domains, A, B and C, being B the transition region between the two peaks within their FWHMs. The analysis of them reproduces the result shown before (left part of Fig. 4.18).

### 4.3.3 Proof of the CEP stability

The carrier-envelope phase stability of the mid-infrared pulses is fully proven by the electro-optic sampling measurements, which guarantee both pulse-to-pulse stability and allows us to estimate the eventual long-term phase drift velocity, or set its upper bounds. The verification of CEP-stability by means of a time-domain measurement technique, like EOS, has the advantages to be the most intuitive way to understand CEP, and that the measurement carries also other useful information, such as the spectrum, the temporal width and of the number of cycles of the pulses, and eventually the chirp. We performed experiments with DFG wavelengths down to 7.8 µm, where the electro-optic sampling is still effective, with a large oscillation amplitude.

With the goal to investigate the long-term stability of the setup, we acquired sequential identical EOS traces over times (many hours) well-exceeding the common acquisition time of a pump-probe experiment. As we will see in chapter 5, the pump-probe signal of mid-infrared pumped-optical probed Copper Germanate is very low, and therefore acquisition times that sometimes reach the whole hour or even more are required, in order to have a high signal-to-noise ratio. For example the data of Fig. 4.19 are constituted by 48 sequential traces over a restricted $\tau$ interval. Each trace is acquired in 50 s. For sake of clarity, we plotted only the four averages over 12 successive traces, and —in violet on the top of the graph— the total average. It is immediately verified that all minima and maxima of the oscillatory signal are reproduced at the same $\tau$ for all traces, and hence that the phase drift over 40 min is less than the detectable phase. To be conservative, we can estimate from this measure a drift velocity lower than $\pi/6$ per hour.

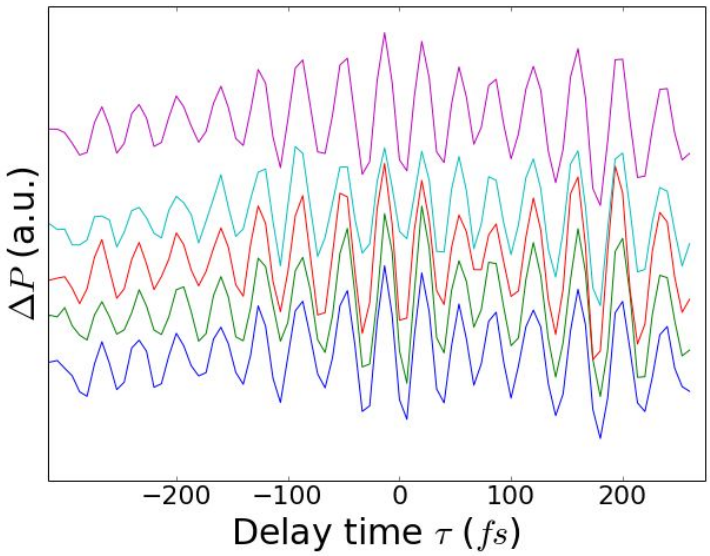


Figure 4.19: Sequential EOS traces, used to verify the long-term CEP-stability. For clarity, the traces are shifted on the ordinate axis. The violet trace, on top, is the average.

# Chapter 5

# Preliminary results on $CuGeO_3$

The pump-probe setup we constructed and succesfully characterized was used to carry out experiments on Gallium Arsenide (GaAs) and Copper Germanate ($CuGeO_3$), whose optical properties were studied in out-of-equilibrium conditions, pumping with the mid-infrared pulses generated in the twin-OPAs+DFG setup, and probing with the ultrashort optical pulses generated in the hollow fiber. We include in this thesis only preliminary results on Copper Germanate, which represent —as we are going to show— a rather interesting scientific case. The goal of the mid-infrared coherent excitation on Copper Germanate is to excite selectively a mid-infrared Copper-Oxygen (Cu-O) phonon mode, investigating the material's optical response at 1.5 eV.
The structure of the chapter is the following: in the first section we introduce Copper Germanate and introduce the leading idea of the experimental activities; in the second section we present the preliminary results, which are then discussed briefly in the third section.

## 5.1 $CuGeO_3$

### 5.1.1 Introduction to $CuGeO_3$

Copper Germanate is an insulating crystal belonging to the family of *cuprates*, and can be classified as a *strong electron correlated system*. Its room temperature structure is schematized in Fig. 5.1, and takes the name of "normal" or "undistorted" phase, in order to distinguish it from the *distorted* phase, present below 14 K. The phase transition between the undistorted and distorted crystal structure is a spin-Peierls transition, in which the lattice distortion is accompanied by the formation of a spin-singlet ground state and the creation of a energy gap in the spectrum of magnetic excitations. In fact, $CuGeO_3$ was the first discovered inorganic spin-Peierls material, and this made it a widely studied material.
The Cu-O vibrational modes have a rather high cross section (Fig. 5.3). It means that the electromagnetic field (with a suitable wavelength) will couple strongly to the phonon modes.
The visible absorption coefficient is depicted in the left part of Fig. 5.3. There is a peak around 1.7 eV due to the phonon assisted *d-d* transitions, sketched on the right part of Fig. 5.1. That peak is separated by the charge transfer edge, which starts around 3 eV.

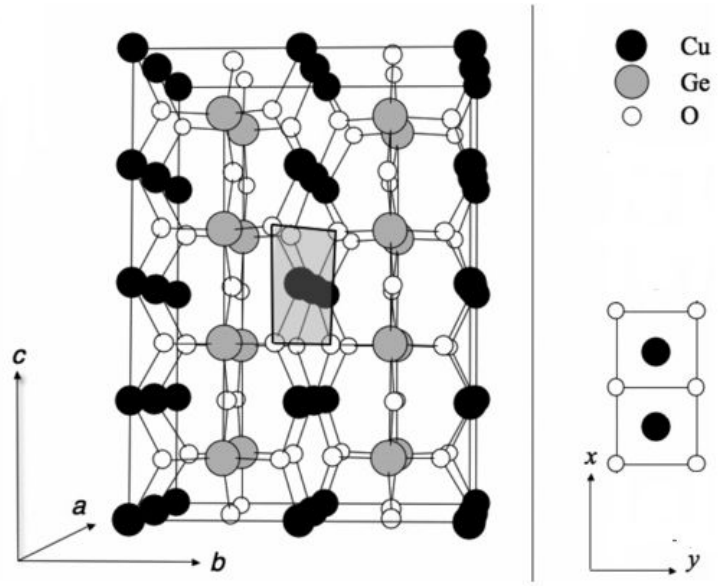


Figure 5.1: $CuGeO_3$ room temperature crystal structure. The shadowed area higlights a corner sharing $CuO_4$ unit. Two of these units are represented in top view, on the right. Adapted from [3]

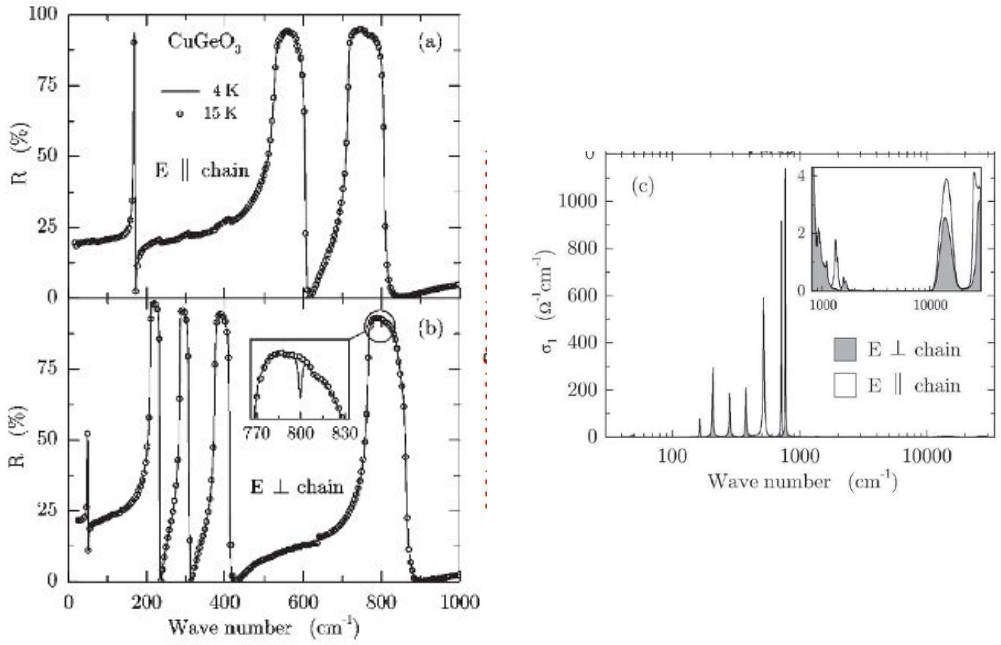


Figure 5.2: Left: infrared reflectivity of $CuGeO_3$ for the polarization along the axis parallel and perpendicular to the Copper chains. Right: infrared conductiviy, again separated for the two possible polarization components. Adapted from [7].

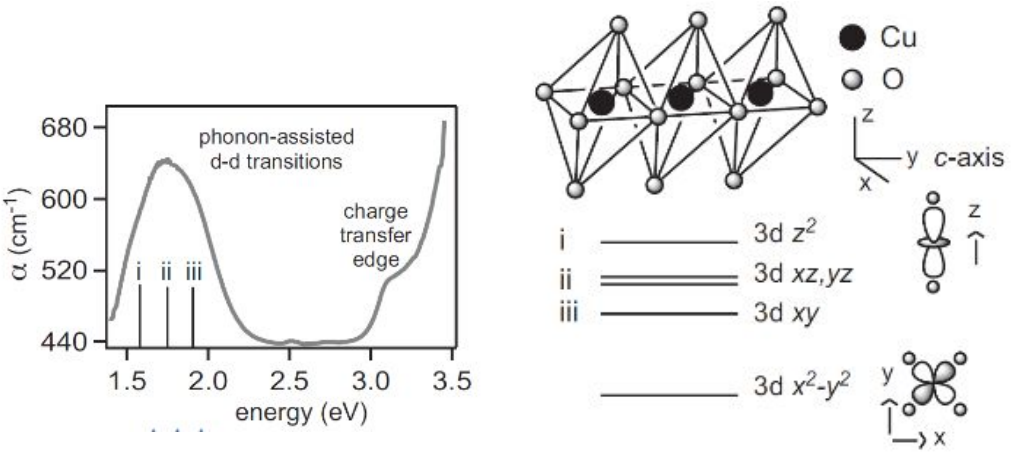


Figure 5.3: Left: Absorption coefficient $\alpha$ in the visible spectral range. Right: Copper-Oxygen octahedra and sketch of the energy level of the *d-d* transitions, which are split by the effect of the crystal field (and the octahedra have non-equivalent axis). Adapted from [8].

Being Copper Germanate an insulator, there are no free charges that can screen the coupling between vibrational modes and crystal field. It was observed, in optical pump-optical probe experiments, that an excitation at 1.5 eV induce a coherent oscillatory response of the material, at the frequency of a Copper-Oxygen phonon mode. The explanation of this effect is the following: the photoexcitation at 1.5 eV triggers a local redistribution of charges, with *d-d* transitions. The charge redistribution is the source of a lattice distortion that makes it possible to observe the coherent phonon in the pump-probe experiments.
The oscillation was observed in pump-probe experients with light pulses shorter than the inverse of the characterisctic phonon frequency. This aspect revealed that the electronic response times for the orbital excitation is expected to be shorter than such time.

### 5.1.2 The experimental idea

The experimental idea that led our activity on $CuGeO_3$ is to study the interplay between orbital excitation and phonon modes in Cu-O octahedra. Such an interplay is believed to play a central role in the physics of the cuprates, where various evidencies point towards a preferential channel for mapping the low energy physics of Cu-O vibrational modes to high energy responses of electronic origin (charge transfer transitions and *d-d*-orbital excitation). It is commonly difficult to study these physics in conducting systems as the presence of conducting electrons introduces collective excitations of electronic origin that mask the peculiar response of the localized electronic excitations. In details, in cuprates *d-d*-transitions lie commonly at energies close to the electronic plasma frequency, so that experiments on conducting systems will measure only the response related to conducting electrons.
Copper Germanate is the ideal playground to address this kind of physics. The

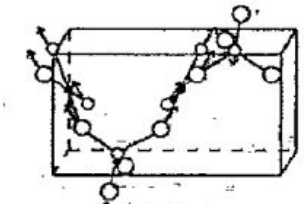

Figure 5.4: Copper-Oxygen stretching mode. Empty circles: Oxygen anions; dark circles: Copper cations.

local electronic structure as well as the vibrational mode of $CuGeO_3$ are similar to the cuprate family where a Cu ion is surrounded by six oxigens in an octahedral configuration (Fig. 5.3, on the right). On the other hand, while in cuprates the *d-d-* and charge transfer-transitions are at similar energies, in Copper Germanate the charge transfer is at 3.2 eV (Fig. 5.3 on the left), while *d-d* transition are in the vicinity of 2 eV. This, together with the insulating character of $CuGeO_3$, makes our sample ideal to single out the coupling between low energy vibrational modes and high energy excitation.

The angle we have taken is the following. A coherent excitation resonant to the phonon can induce a coherent lattice oscillation that —for the same coupling just described— can be mapped in the variation of the optical properties at 1.5 eV.

The phonon we aim to stimulate is the infrared stretching mode represented in Fig. 5.4, which has a wavelength of 13.2 µm, completely in the working range of the twin-OPAs+DFG setup.

## 5.2 Preliminary results

The pump-probe setup is that described for electro-optic sampling, except that with $CuGeO_3$ we performed experiments both measuring the variation in transmittivity and in polarization. With reference to Fig. 4.12, we do not use the Wollaston prism and the quarter-wave plate, when carrying out measurements of $\Delta T$. We just use the photodiodes PD1 and PD3, accounting for the probe after the material and the reference probe respectively.

The thickness of $CuGeO_3$ should be very small, of the order of magnitude of the wavelength corresponding to the energy of the phonon we aim to excite. On the other hand, using a thicker sample increase the signal measured. As a parameter to evaluate the best compromise, we proceed as follow. Using the refractive index at 13 and 0.8 µm, we calculated the maximum thickness we can use in experiment, as the thickness for which the pump (13 µm) and the probe (0.8 µm) would acquire a time difference of 10 fs propagating through the sample (approximately a quarter wavelength of the pump). A thickness of 100 µm was obtained. We employed $CuGeO_3$ crystals with thicknesses significantly below that limit, of approximately 40 µm and 20 µm, obtained via exfoliation.

The strategy is to pump both under, at, and above the 13.2 µm-wavelength phonon threshold. The first results can be seen in the following figures obtained with pump wavelengths of approximately at 10, 13.7 and 16 µm.

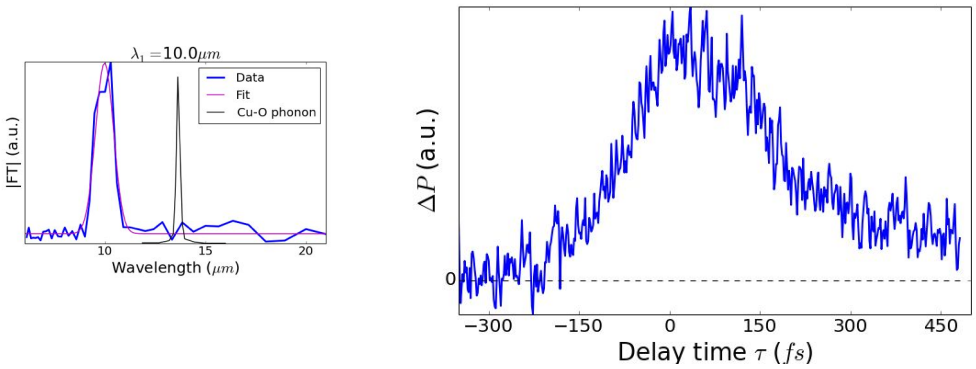


Figure 5.5: Left: pump spectrum, centered around 10 µm, from Michelson interferometry. We are pumping with photon energies larger than the phonon energy. Right: polarization rotation of the probe.

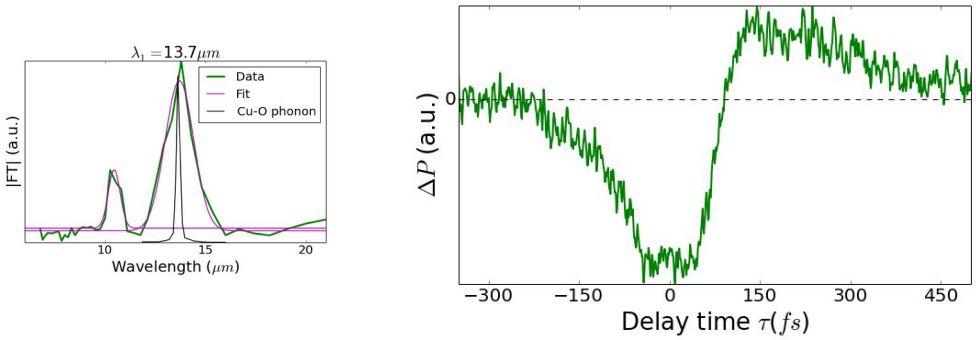


Figure 5.6: Left: pump spectrum, with double peak, at 10.5 µm (the smaller) and at 13.7 µm (the higher), from Michelson interferometry. We are pumping with photon energies resonant with the Cu-O stretching mode. Right: polarization rotation of the probe. There is a quite strong rotation on the opposite side with respect to the rotation direction when pumping above threshold.

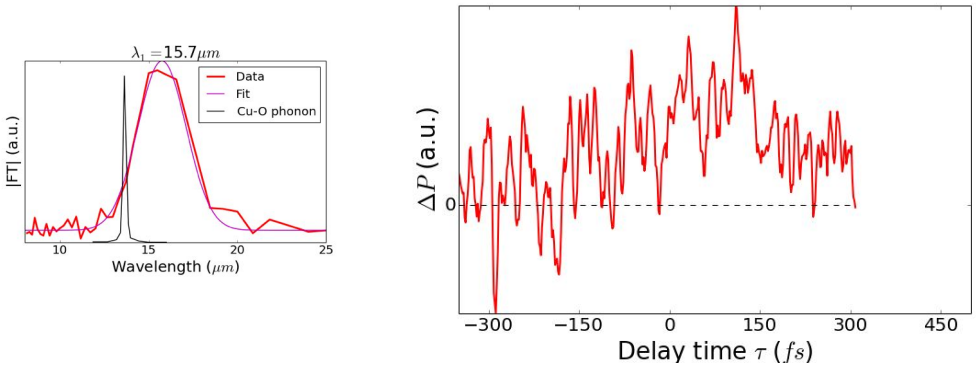


Figure 5.7: Left: pump spectrum, centered around 16 µm and quite broadband,from Michelson interferometry. We are pumping with photon energies below the phonon energy. Right: polarization rotation of the probe.

The pump-probe traces have different signal-to-noise ratios because they are the average of many scans (4, 50 and 10 from the bluest to the reddest pump respectively). Single scans do not contain oscillating terms. The intensity of the pump pulses was decreasing for larger pump wavelengths, as pointed out many times. It is not possible to easily re-normalize the response $\Delta P$ of the sample with respect to the measured energy per pulse of the pump at different wavelength, because at different wavelengths the pump beam does not have always the same divergence, nor the ZnSe lens has the same focal length (its refractive index decreases for wavelengths above $\sim 14\,\mu m$).
In these three pump-probe traces the geometry was constant, with both pump and probe polarized on the $c$-axis of $CuGeO_3$. No relevant signal was found pumping with polarization along the $a$-axis, whatever the (linear) probe polarization.

## 5.3 Discussion

As depicted in Fig. 5.5, 5.6 and 5.7, we observe a non-trivial response to photo-excitation at different wavelength. In spite of the preliminary nature of the measurements we can draw a few relevant conclusions which open for a very interesting scenario. The two most relevant observation on those figures are: first, the transient changes of polarization are different in the case of resonant and off-resonant excitation of the phonon mode and, second, in spite of the carrierenvelope phase-stable pump pulses, no coherent modulation of the 800 nm response is revealed.
The non-resonant excitation at energies higher than the phonon modes gives a strong rotation of the polarization. The rotation of the polarization of the transmitted light has to be expected in case of a light driven sample heating. Various X-ray studies demonstrated that $CuGeO_3$, undergoes a highly anisotropic thermal expansion, in particular while the $a$ and $b$ axis have a positive thermal expansion coefficient, the $c$-axis displays a negative one. This effect it is likely to result in a temperature dependent birefringence of $CuGeO_3$, also suggested by [19][1].

In this perspective, the time domain polarization transmitted by the sample is a good probe of how the effective anisotropy evolves in time subsequently to photo-excitation. For pump energies higher than the phonon mode (Fig. 5.5), the electromagnetic field will excite preferentially the Cu-O mode depicted in Fig. 5.3.The fast decay observed can be interpreted as the thermalization process among the different low energy degrees of freedom of the sample. More in details, the fast decay time observed in Fig. 5.5 is consistent with phonon-phonon thermalization times, mainly determined by phonon anharmoniciy.
The plateau reached several hundreds femtosecond after photo-excitation is consistent with a state where the different phonons are thermalized and the residual polarization rotation is due to the different temperatures between the initial and the final state in the sample. The longer decay time of this signal will be limited by heat diffusion into the sample.

[1] To the best of my knowledge, a temperature dependent birefringence in $CuGeO_3$ has never been reported at equilibrium, but the anisotropic expansion is a strong indication that such an effect will be present. The two indexes of refraction parallel and orthogonal to the principal optical axis of $CuGeO_3$ will be changed in a different way by thermal expansion. I can speculate that the lack of evidences in this sense could be either due to the small size of the effect making its measurements difficult with equilibrium techniques or, more simply, to the lack of interest of the condensed matter comunity to this aspect.

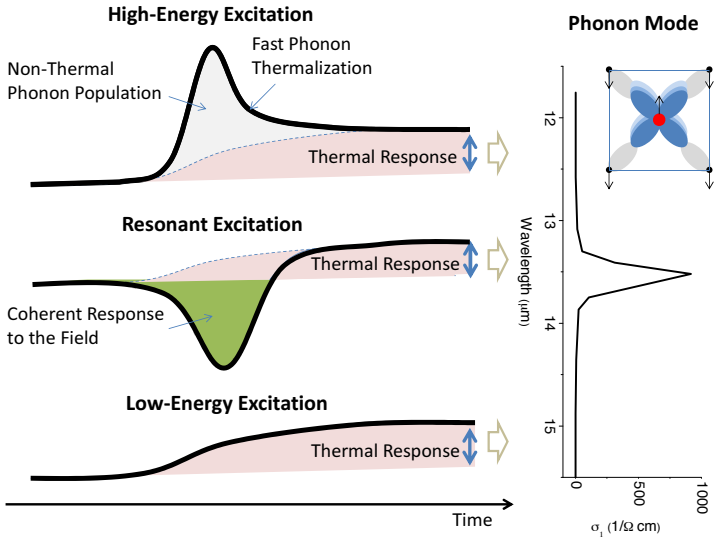


Figure 5.8: Schematical representation of the possible physical process. From bottom to top: photo-excitation below the phonon, at the phonon energy and above it. The long-term thermal response is basically the same, but a pump resonant to the phonon will induce a coherent (hence strongly non-thermal) response, and a pump above the phonon threshold will aslo populate the phonon states, although differently. In the right a small portion of the phonon spectrum is plotted. In the top-right corner the ∼13 µm-wavelength Cu-O stretching mode is represented. Cu in red, O in black, $d_{x^2-y^2}$ orbital in blu, and $p$ orbitals in grey.

In order to further test this scenario, we turn to excitation processes with pump pulses at energies lower than the phonon mode, i.e. at longer wavelength. The measurements (Fig. 5.7) show that no transient non-thermal population of the phonon modes is revealed. The measurements are poor in quality due to both the low cross section of the photo-excitation and the low energy per pulse reached in our setup (Fig.4.9). Nevertheless, a small signal revealing just a long lived tiny component is consistent with our interpretation where most of the signal observed is due to the population number of the ∼13 µm phonon mode. In this scenario, photo-excitation with energy lower than the phonon frequency will not directly excite the vibrational mode and the small residual signal is due to the thermalization effects which will lead to a non-negligible change of the phonon mode excitation.

The most interesting scenario is revealed by the photo-excitation process with a pump resonant to the phonon frequency. As revealed in Fig. 5.6, the resonant excitation leads to a transient signal which change sign with time. The long time response is consistent with the signal revealed by photo-excitation at high energy and can be described as a thermalization process transferring energy from the phonon mode resonantly excited to other modes. Surprisingly, the signal reveals also a signal of opposite sign when the pump electric field is present. Such a transient is likely due to the coherent response of the vibrational modes which seems to drive an overall increase of the anisotropy, analogous to the effects of a transient reduction of the temperature.

The physics scenario revealed is depicted with a cartoon in Fig. 5.8. The photo-excitation at energies higher than the resonant frequency drives a non-thermal population of the phonon mode which results in a time dependent anisotropic response, relaxing on phonon thermalization timescales. On the other hand the resonant excitation of the mode produces a sort of rectified response which goes in the opposite direction with respect to the thermal response.

Unfortunately the poor quality of the data does not allow to perform a quantitative analysis of the anharmonic coupling and of the coherent displacement of the ions following the resonant excitation of the phonon mode. Further measurements will be needed to substantiate and validate the physics scenario emerging.

# Conclusions

In this thesis we have shown the design, the construction and the characterization of a new "Twin-OPAs+DFG" optical setup for pump-probe experiments. It allows us to generate ultrashort carrier-envelope phase-stable pulses in a tunable mid-infrared range. A complete study of the mid-infrared electromagnetic field was carried out thanks to ectro-optic sampling in a thin ZnTe crystal; short- and long-term phase stability was proven by such measurements.
We used those mid-infrared pulses in benchmark mid-infrared pump-ultrashort optical probe experiments on $CuGeO_3$, whose preliminary results are presented in chapter 5.

With this thesis we gave a little contribution to enlarge the present technological frontiers in order to obtain an ultrafast coherent control of the optical properties of materials.

# Ringraziamenti

Il mio ringraziamento più sentito va a Daniele e Francesco, che mi hanno introdotto, insegnato e guidato nell'attività di questo progetto di tesi. Sono stati sette/otto mesi moto belli, in primis per l'amicizia e il lavoro in lab. È stato un onore collaborare con voi, e —*ça va sans dire*— l'amore sbocciatomi per il laboratorio è da ascrivere in toto tra le vostre colpe.
In particolare a Daniele va la riconoscenza per avermi proposto un progetto non banale e in buona parte da scoprire assieme, per la fiducia, l'aiuto costante, la visione scientifica, e —paradigmaticamente— per quell'alba carsolina sopraggiunta senza accorgercene, intenti a pumprobare. A Francesco per tutto il tempo trascorso nell'oscurità del lab a spremere dal setup qualche milliwatt in più (da cui l'epiteto affettuoso di "mago degli OPA"), per le fine settimane ad Elettra, per iPython, LabView, i disegni, lo sguardo intuitivo sui processi fisici, l'aiuto su tutti i fronti e molto altro.

Desidero ringraziare il prof. Parmigiani per avermi accolto nel gruppo di ricerca, per il costante interesse sul progredire del progetto, e non da ultimo per aver dato vita alla bella realtà che è il T-ReX, della quale ho potuto far parte in questi mesi. Rimanendo in ambito T-ReX, un grazie va a Goran per l'aiuto con la fibra e i laser, a Federico per i consigli tecnici, a Fabio e Andrea M. per aver lavorato al progetto nella sua prima fase, a Martina E. per gli aiuti e la simpatia, e poi a Francesca, Giulia, Martina D., Barbara, Alberto, Andrea S., Toni e Marco, che *tutti* mi hanno insegnato qualcosa.

Sono grato ad Elettra-Sincrotrone Trieste S.C.p.A., al programma europeo LLP-Erasmus, alla dott.ssa Lia Brautti e al Collegio Universitario per le Scienze "Luciano Fonda", che (attraverso rimborsi, borse e premi di studio) hanno finanziato in gran parte il mio quinquennio di studi triestini. In particolare il "Fonda", che ha giocato un ruolo determinante nella mia scelta dell'Università, sia per la Triennale che per la Magistrale.

Mi ritengo estremamente fortunato per gli anni vissuti in questa magnifica città, la *mia* città, casa *mia*. Vissuti assieme agli amici, assieme ad Agnese, Letizia, Oscar, Mara, Matteo, Enrico, Nicola, Elisa, Gianluca, Cristina, Luca, Adriano, Nadira, Alessandro, Alex, Anna, e poi Gabriele, Fabio, Daniele, Nicola F., Đơn, Enrico R., Enea, Thomas, Michele, Tommaso, Manuel e tanti altri (no, non è un modo di dire), che sono in dovere di ringraziare perché cadauno mi ha dato qualcosa di importante. Mi piacerebbe potermi soffermare singolarmente su ognuno di voi, ma è chiaro che in questa sede finirei tosto fuori tema.

Impossibile non citare tutti gli amici dei (o meglio: dai) tempi scolari, primariamente Francesco, che ringrazio per l'amicizia e la stima, ed Emanuele, per la complicità liceale.

Infine con grande affetto ringrazio mia madre, mio padre, mia sorella, mio fratello e le mie nonne per il supporto, la comprensione e la stima mai venute meno.
Ed Alessandra, per l'essere stata con me in questi anni, ad amarmi ed essere amata.

*Ghil*

Trieste, ottobre 2014.

# Bibliography


[1] As-Photonics. http://www.as-photonics.com/snlo.

[2] Robert W. Boyd. *Nonlinear Optics*. Academic press, 2003.

[3] Bondino et al. Crystal-field and zhang-rice-singlet excitations in $cuge_{1-x}si_xo_3$ (x=0, 0.05, and 0.1) from temperature-, angle-, and polarization-dependent resonant soft x-ray emission. *Physical Review B*, 75, 2007.

[4] Bradler et al. Femtosecond continuum generation in bulk laser host materials with sub-$\mu$j pump pulses. *Applied Physics B*, 97, 2009.

[5] Cerullo et al. Ultrafast optical parametric amplifiers. *Review of Scientific Instruments*, 7(1), 2003.

[6] Cerullo et al. Few-optical-cycle light pulses with passive carrier-envelope phase stabilization. *Laser Photonics Reviews*, 5(3), 2011.

[7] Damascelli et al. Optical spectroscopy of pure and doped $cugeo_3$. *Physical Review B*, 61, 2000.

[8] Giannetti et al. Disentangling thermal and nonthermal excited states in a charge-transfer insulator by time- and frequency-resolved pump-probe spectroscopy. *Physical Review B*, 80, 2000.

[9] Jones et al. Carrier-envelope phase control of femtosecond mode-locked lasers and direct optical frequency synthesis. *Science*, 288, 2000.

[10] Junginger et al. Single-cycle multiterahertz transients with peak fields above 10 mv/cm. *Optics Letters*, 35(15), 2000.

[11] Koke et al. Direct frequency comb synthesis with arbitrary offset and shot-noise-limited phase noise. *Nature Photonics*, 4, 2010.

[12] Koke et al. Noise performance of a feed-forward scheme for carrier-envelope phase stabilization. *Applied Physics B*, 104(4), 2011.

[13] Liu et al. Gase crystals for broadband terahertz wave detection. *Applied Physics Letters*, 85(863), 2004.

[14] Manzoni et al. Single-shot detection and direct control of carrier phase drift of midinfrared pulses. *Optics Letters*, 35(5), 2010.

[15] Paulus et al. Absolute-phase phenomena in photoionization with few-cycle laser pulses. *Nature*, 414, 2001.

[16] Wittmann et al. Single-shot carrier–envelope phase measurement of few-cycle laser pulses. *Nature Physics*, 5, 2009.

[17] Wu et al. Free-space electro-optics sampling of mid-infrared pulses. *Applied Physics Letters*, 71(1285), 1997.

[18] FEMTOLASER. http://www.femtolasers.com/kaleidoscope-tm.122.0.html.

[19] Yulia Matiks. Spectroscopic ellipsometry of spin-chain cuprates and lanio3-based heterostructures. *Ph.D. thesis at Universit}, 2011.*

*[20] Andrea Mattioni. Progettazione e realizzazione sperimentale di un opa.* B.Sc. thesis, Università degli Studi di Trieste*, 2013.*

*[21] Francesco Randi. Generazione e caratterizzazione di un impulso supercontinuo di luce bianca.* B.Sc. thesis, Università degli Studi di Trieste*, 2011.*

*[22] Francesco Randi. Pulsed homodyne detection for quantum state reconstruction applied to ultrafast non-equilibrium spectroscopy.* M.Sc. thesis, Università degli Studi di Trieste*, 2013.*

*[23] Leitenstorfer Sell and Huber. Phase-locked generation and field-resolved detection of widely tunable terahertz pulses with amplitudes exceeding 100 mv/cm.* Optics Letters*, 33(23), 2008.*

*[24] Ye and Cundiff.* Femtosecond Optical Frequency Comb: Principle, Operation, and Applications*. 2004.*